Alma Mater Studiorum – Università di Bologna

DOTTORATO DI RICERCA IN

Scienze Biotecnologiche, Biocomputazionali, Farmaceutiche E Farmacologiche

Ciclo XXXIV

Settore Concorsuale: 05/E3

Settore Scientifico Disciplinare: BIO12

STUDY OF BONE BIOMINERALIZATION IN 2D AND 3D CULTURES OF A HUMAN OSTEOSARCOMA CELL LINE AS OSTEOBLAST-LIKE MODEL

Presentata da: Giovanna Picone

Coordinatrice Dottorato	**Supervisore**
Prof.ssa Maria Laura Bolognesi	Prof. Stefano Iotti

Esame finale anno 2022

Abstract

This PhD project focuses on the study of the early stages of bone biomineralization in 2D and 3D cultures of osteoblast-like SaOS-2 osteosarcoma cells, exposed to an osteogenic cocktail.

First, the efficacy of osteogenic treatment was assessed on 2D cell cultures after 7 days. A large calcium minerals production, an overexpression of osteogenic markers and of alkaline phosphatase activity occurred in treated samples.

TEM microscopy and cryo-XANES micro-spectroscopy were performed for localizing and characterizing Ca-depositions. These techniques revealed a different localization and chemical composition of Ca-minerals over time and after treatment. Nevertheless, the Mito stress test showed in treated samples a significant increase in maximal respiration levels associated to an upregulation of mitochondrial biogenesis indicative of an ongoing differentiation process.

The 3D cell cultures were realized using two different hydrogels: a commercial collagen type I and a mixture of agarose and lactose-modified chitosan (CTL).

Both biomaterials showed good biocompatibility with SaOS-2 cells. The gene expression analysis of SaOS-2 cells on collagen scaffolds indicated an osteogenic commitment after treatment and Alizarin red staining highlighted the presence of Ca-spots in the differentiated samples. In addition, the intracellular magnesium quantification, and the X-ray microscopy on mineral depositions, suggested the incorporation of Mg during the early stages of bone formation process.

SaOS-2 cells treated with osteogenic cocktail produced Ca mineral deposits also on CTL/agarose scaffolds, as confirmed by alizarin red staining. Further studies are underway to evaluate the differentiation also at the genetic level.

Thanks to the combination of conventional laboratory methods and synchrotron-based techniques, it has been demonstrated that SaOS-2 is a suitable model for the study of biomineralization *in vitro*. These results have contributed to a deeper knowledge of biomineralization process in osteosarcoma cells and could provide new evidences

about a therapeutic strategy acting on the reversibility of tumorigenicity by osteogenic induction.

Contents

List of abbreviations

A-CHA A-Carbonatate Hydroxyapatite

ACP Amorphous Calcium Phosphate

ALPL Alkaline Phosphatase

ARS Alizarin Red Staining

ATF4 Activation of transcription factor 4

BGLAP Bone Gamma-Carboxyglutamate Protein

BLCs Bone lining cells

BM Biomineralization

BMMSCs Bone Marrow Mesenchymal Stem Cells

BMPs Bone Morphogenetic Proteins

BSP Bone Sialo Protein

CBF-α-1 Core-Binding Factor Subunit A-1

CM Control Medium

COL1A1 Collagen 1 A1

COL1A2 Collagen 1 A2

CPC Cetyl pyridinium Chloride

CREB cAMP-Responsive Element-Binding

CTL Lactose-Modified Chitosan

DCHQ5 Diaza-18-Crown-6-Hydroxyquinoline

DDW Double Distillate Water

DLX5 Distal-Less Homeobox 5

ECM Extracellular Matrix

ER Endoplasmic Reticulum

ESB European Society for Biomaterials

EXAFS Extended X-Ray Absorption Fine Structure

FCCP Carbonyl Cyanide-p-Trifluoromethoxy Phenylhydrazone

FGF-23 Fibroblast Growth Factor 23

HA Hydroxyapatite

HbMSCs Human Bone Marrow Mesenchymal Stem Cells

hFOB Human Fetus Osteoblast

Hh Hedgehog

HPP Hypophosphatasia

IL-1b Interleukin 1b

M-CSF (or **CSF-1**) Macrophage Colony Stimulating Factor

MSC Mesenchymal Stem Cell

MSX2 Msh Homeobox 2

MVs Matrix Vesicles

NCPs Non-Collagen Proteins

OCR Oxygen Consumption Rate

OM Osteogenic Medium

OPG Osteoprotegerin

OPN Osteopontin Protein

OS Osteosarcoma

OSX (or **SP7**) Osterix

PBS Phosphate Saline Buffer

PGA Polyglycolic Acid

PHOSPHO1 Phosphatase Orphan 1

Pi Inorganic Phosphate

PLGA Polylactic-Co-Glycolic Acid

PLLA Polylactic Acid

PPi Inorganic Pyrophosphate

Ptc Patched

PTH Parathyroid Hormone

RANKL Receptor Activator of Nuclear Factor Kappa-B Ligand

RB1 RB Transcriptional Corepressor 1

RT Room Temperature

RUNX2 Runt-Related Transcription Factor 2

SAXS Small-Angle X-Ray Scattering

SM Sphingomyelin

Smo Smoothened

SMPD3 Sphingomyelin Phosphodiesterase 3

SPARC Secreted Protein Acidic and Cysteine Rich

SPP1 Secreted Phosphoprotein 1

SR Synchrotron Radiation

STXM Scanning Transmission X-Ray Microscopy

SZ Seal Zone

TCP Tricalcium Phosphate

TE Tissue Engineering

TEM Transmission Electron Microscope

TGF-β Transforming Growth Factor B

TNF Tumor Necrosis Factor

TNF-α Tumor Necrosis Factor Alpha

TXM Transmission X-Ray Microscopy

XANES X-Ray Absorption Near Edge Structure

XAS X-Ray Absorption Spectrometry

X-CT X-Ray Computed Tomography

XPS X-Ray Photoelectron Spectroscopy

XRD X-Ray Diffraction

XRF X-Ray Fluorescence

XRFM X-ray Fluorescence Microscopy

µCT Micro-Computed Tomography

1. Introduction

Bone is a biomineralized tissues, with a well-structured organization. Bone formation and repair are a widely studied topics due to their effects in the medical, bio-technological, and bioengineering fields.

Bone regeneration involves a complex process known as biomineralization. This is a ubiquitous phenomenon in the animal kingdom, consisting of the formation of organized mineral crystals [1]. In humans, the early steps of this process begin at the nanometric scale, through chemical-physical transformations, performed by the cellular activity, by which ions are converted into complex calcium composite materials and culminate forming hexagonal hydroxyapatite (HA) crystals [2].

In general, the investigation of the mineralization process in bone has been difficult due to the restricted localization of the formation sites, the way the process proceeds and therefore the nature of the bone itself. This has made it imperative to use cell models (especially 3D cell cultures) to generate hypotheses which are then tested in explanted or animal models [3]. To date, most studies have investigated the advanced stages of biomineralization, but the mechanism that explains the genesis within the cell and the propagation of the mineral in the extracellular matrix still remain largely unexplained.

A deeper understanding of the morphology and formation of bone tissue, combined with tissue engineering approaches, could offer the possibility to mimic nature for the development of bio-inspired materials and find new therapeutic strategies to treat different bone diseases.

1.1 Biology of bone tissue

Bone is a complex and dynamic vascular mineralized tissue with multiple functions. It serves as an attachment point for muscles and tendons, protects and supports internal organs, and serves as a storehouse for minerals [4].

Its complex and hierarchically organized structure can be described from the macro- to nanoscale levels (**Fig. 1**). It is composed of bone cells and an extracellular nanocomposite matrix of minerals (65%), water (10%), lipids (1%), and proteinaceous material (25%), the latter consisting of type I collagen (90%) and non-collagenous proteins (10%) [5]. All these components give bone its remarkable mechanical properties and ability to remodel. The composition and architectural features vary with age, sex and species and can be affected by disease and treatment [6–8].

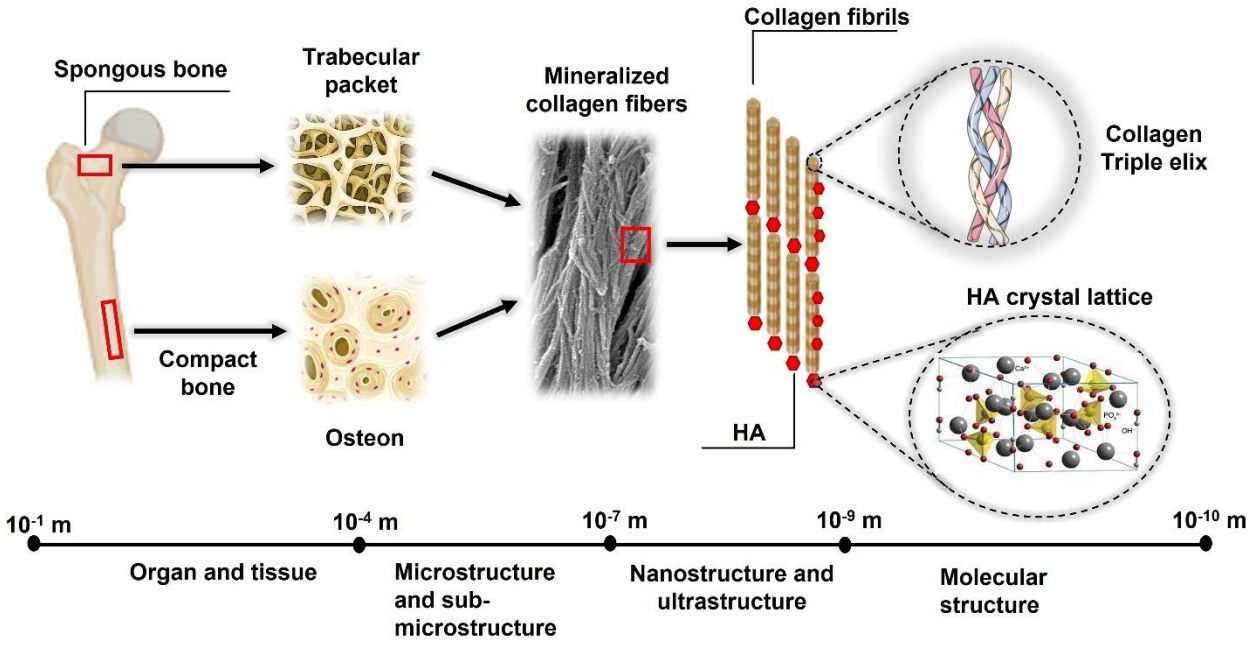

Figure 1 Hierarchical organization of bone from the macro- to the nanoscale levels.

1.2 Bone cells

Bone tissue is composed of a heterogeneous population of cells responsible for the growth, formation, and repairs of bone. Each type of cell has specific functions and its own characteristics. Here is a brief overview of the different cell types.

Osteoprogenitor cells

Osteoprogenitor cells, also known as osteogenic cells or pre-osteoblasts, are human mesenchymal stem cells that reside in the bone marrow and play a prominent role in bone repair and growth. Osteoprogenitors can self-replicate, renew themselves and participate in osteogenic differentiation. They are localized in the endosteum (a membrane lining the wall of the bone marrow cavity) and in the lining of osteogenic cells and are the precursors of specialized cells as osteocytes and osteoblasts [9]. In mature bone osteoprogenitor cells exist as flattened spindle-shaped structures. They attach to the bone surface and are referred to as "inactive osteoblasts" at this time. During fetal development or during periods of high turnover in adult osteogenesis, osteoprogenitor cells exhibit plump oval nuclei and abundant spindle-shaped cytoplasm and they later transform into characteristic cuboidal active osteoblasts. [10].

Osteoblasts

Osteoblasts are large cells responsible for synthesizing and mineralizing bone during both initial bone formation and later bone remodeling. They arise from the differentiation of osteogenic cells in the periosteum and from mesenchymal stem cells (MSCs) in the endosteum of the bone marrow cavity. The activity of osteoblasts is greatest during embryonic skeletal formation and growth, but they are present through all life [11,12]. When osteoblasts are mature, they surround themselves with bone matrix becoming osteocytes. Osteoblasts that remain on the surface of the bone in front of the periosteum have the potential to become inert cells of the bone lining or undergo

apoptosis. As the population of mature osteoblasts declines, new osteoblasts differentiate from mesenchymal progenitor cells, but their resources are limited [13].Osteoblastic differentiation requires a regular blood supply and the involvement of many genes, proteins, and cytokines, which are described in more detail in the following sections [12].

Osteocytes

Osteocytes arise from the MSC (mesenchymal stem cell) lineage through the differentiation of osteoblasts and account for 90-95% of total bone cells [14].

At the end of a cycle of bone formation, a subpopulation of osteoblasts becomes osteocytes embedded in the bone matrix. They are connected to each other and to the cells of the bone surface and even to the cells of the bone marrow by dendrite-like projections contained in fluid-filled microchannels (canaliculi) that radiate to the surface and to the blood supply. The shape and spatial arrangement of osteocytes are consistent with their function of signal detection and transport. [4].

In this way, osteocytes can respond to changes in mechanical forces and in the levels of circulating factors such as hormones and ions. They amplify these signals, resulting in a coordinated adaptive skeletal response to environmental stimuli [15]. Osteocytes are long-lived cells, but like osteoblasts and osteoclasts, they die by apoptosis. Decreased osteocyte viability is related to bone fragility caused by estrogens and androgens deficiency or deprivation and excess glucocorticoids [16].

Osteoclasts

Osteoclasts are differentiated and multinucleated cells that arise from mononuclear cells of the hematopoietic stem cell lineage. Osteoclast formation depends critically on two cytokines, namely macrophage colony-stimulating factor (M-CSF or CSF-1), nuclear factor K ligand receptor activator (RANKL) [17,18] and another factor called osteoprotegerin (OPG). The RANKL / RANK / OPG system is an important mediator of osteoclastogenesis [19,20]. An abnormal increase in osteoclast formation and

activity leads to some bone diseases such as osteoporosis, in which resorption exceeds formation, resulting in a decrease in bone density and an increase in fractures [21]. In addition, osteoclasts produce factors called clastokines that control osteoblasts during the bone remodelling process. Recent evidences have demonstrated that osteoclasts can also directly regulate the hematopoietic stem cell niche. These results show that osteoclasts are not only bone resorbing cells, but also a source of cytokines that affect the activity of other cells [4].

Bone lining cells

Bone lining cells (BLCs) cover inactive bone surfaces. BLCs have flat or slightly ovoid nuclei and are connected to each other by gap junctions. They can be stimulated to proliferate and differentiate into osteogenic cells and may provide a source of osteogenic progenitor cells [22]. The functions of bone lining cells are not fully elucidated, but these cells can prevent direct interaction between osteoclasts and the bone matrix when bone resorption should not occur. They are able to produce OPG and RANKL and could be involved in osteoclast differentiation [23].

1.3 Bone Extracellular matrix

1.3.1 Organic components: Collagen I and Non-collagen proteins

The organic bone matrix is composed of type I collagen (~ 90%) and non-collagenous proteins (NCPs) (10%) [24]. Type I collagen is a triple helix molecule containing three polypeptide chains: two α1 (I) chains and one α2 (I) chain. It is synthesized as a precursor procollagen and translocated into the lumen of the rough endoplasmic reticulum (ER). The procollagen molecules are transported through the Golgi and secreted by the cell. Hydrogen bonds between hydroxyproline and other charged amino acid residues hold together polypeptide chains that form a linear triple helix of collagen approximately 300 nm in length. The triple helices are assembled into fibrils, which in turn cluster into collagen fibers [25,26].

The collagen fibrils provide places for precipitation of nano-hydroxyapatite crystals on their surface to form mineralized structural units of bone [27].

Collagen I is a key component of the extracellular matrix (ECM) of bone and forms associations with integrins on the cell surface and other ECM proteins.

NCPs have been shown to play important roles in regulating osteoclast and osteoblast function, organizing the extracellular matrix, coordinating mineral-matrix and cell-matrix interactions, and regulating the bone mineralization process [28].

Among the most important ones are osteocalcin, osteonectin, osteopontin, sialoprotein II, bone morphogenetic proteins (BMPs), growth factors, and other small leucine-rich proteoglycans [29].

1.3.2 Mineral constituent: Hydroxyapatite

The bone mineral component consists of a highly substituted, poorly crystalline nanocrystal of hydroxyapatite [$Ca_{10}(PO_4)_6(OH)_2$] with a Ca/P ratio of less than 1.67, as demonstrated by X-ray diffraction over 60 years ago [2].

Although there is still disagreement about the initial phase of the deposited mineral, it is now accepted that the mature bone mineral is a substituted crystalline phase of calcium phosphate termed carbonated hydroxyapatite [30].

Recently, Sorrentino et al. have hypothesized that $CaCO_3$ in the initial phase of biomineralization of human bone marrow mesenchymal stem cells (hbMSCs) starts as an amorphous phase that develops into crystalline calcite after 4 days of osteogenic engagement. In their study, both crystalline compounds, calcite, and hydroxyapatite were detected [31], (**Fig. 2A)**. Biological HA crystals are plate-like nanocrystals with a thickness of 2-3 nm and a length and width of tens of nanometers. Human HA is not stoichiometric, but contains many substituted elements, some in the ppm range, that play important roles in bone metabolism. Substitution by ions can affect crystal structure, surface charge, solubility, and other physicochemical properties.

The most important substituent in biological apatite is carbonate (CO_2^{3-}), which is typically present in the bone mineral in amounts of 5-8 wt %. The carbonate ion can be substituted at two positions in the apatite structure, namely at the hydroxyl position and at the phosphate ion position, giving the A- and B-type of carbonate apatite, respectively. The B-type is the preferred carbonate substitution found in the bones of a variety of species, with the A/B ratio ranging from 0.7-0.9. A higher value of A/B ratio was observed in old tissue compared to young tissue. The apatite lattice structure and the A- and B-type carbonate substitutions are shown in **Fig. 2B**.

The presence of B-type carbonate substitution in the apatite lattice can cause a decrease in crystallinity and an increase in solubility. In addition, osteoblasts show a lower affinity for the surface of A- CHA, compared to that of HA [32].

Natural HA contains other impurities such as sodium (0.9%) and magnesium (0.5%), fluorine, zinc, barium, and strontium ions as substitute groups in phosphate and hydroxyl sites, resulting in poorly crystalline, low calcium and carbonated HA [33,34]. In a study performed on hbMSCs exposed to an osteogenic cocktail for 4 and 10 days, Procopio et al. showed that biomineralization begins with the nucleation of Zn-hydroxyapatite within the cell and rapidly develops into hexagonal hydroxyapatite crystals that are very similar in composition and structure to those found in human bone [35]. These types of substitutions can lead to changes in the mechanical properties of bone. They can decrease crystallinity by altering solubility, which is important for mineral homeostasis and bone adaptation [24].

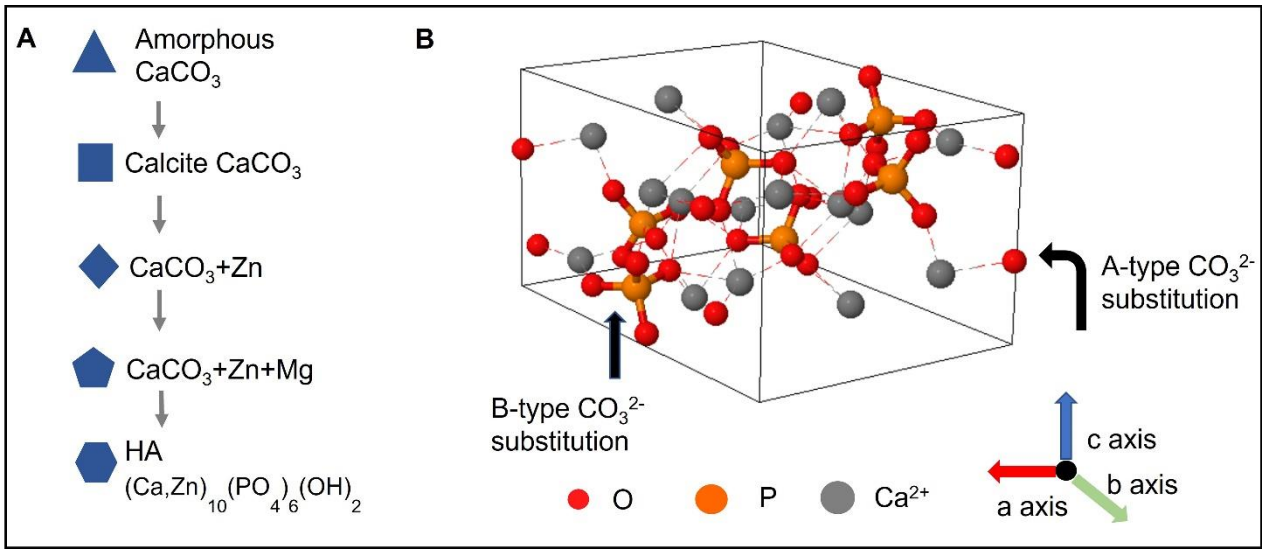

Figure 2 A) Evolution of Ca compounds during the early phases of osteogenic differentiation, based on the model proposed by Sorrentino et al., 2021 [31]. **B)** Hexagonal unit cell of a hydroxyapatite crystal $Ca_{10}(PO_4)_6(OH)_2$, taken from ChemTube3D. Direction of a-, b-, c axis determines spatial configuration of apatite structure. Black arrows indicate the positions of A-type and B-type carbonate substitution.

1.3.2 Magnesium in Bone

Magnesium is quantitatively one of the most important substituent ions for Ca^{2+} in the formation of biological apatite. In calcified tissues, the amount of magnesium associated with the apatite phase is greatest at the beginning of the calcification process and decreases as calcification progresses. The partial replacement of Ca^{2+} by Mg^{2+} leads to a reduction in the c-axis size, because the radius of Mg^{2+} (0.69 Å) is much smaller than that of Ca^{2+} (0.99 Å), resulting in a change in the lattice constants of apatite. In addition, magnesium inhibits apatite crystallization, destabilizes the HA structure, and promotes its thermal transformation to tricalcium phosphate (TCP) [32]. Magnesium deficiency negatively affects all stages of skeletal metabolism, resulting in cessation of bone growth, decreased osteoblastic and osteoclastic activity, osteopenia, and bone fragility. Magnesium deficiency can lead to bone loss due to altered

mechanisms related to hormone regulation (PTH), stimulation of proinflammatory cytokines (IL -1b and TNF-a), and alteration of hydroxyapatite crystal formation [36]. Magnesium-substituted HA has been extensively studied for its potential in the development of artificial bone and other medical applications, as Mg^{2+} promotes the formation of new bone mineral nuclei. [37,38].

1.4 Osteogenic commitment

1.4.1 Osteogenic Gene markers and regulator proteins

The osteoblast phenotype is promoted by several regulatory proteins and specific transcription factors that promote the expression of osteogenic phenotypic genes. The key molecular switch for the incorporation of mesenchymal progenitors into the osteoblast lineage is the transcription factor Runt-related transcription factor 2 (*RUNX2*), also known as core-binding factor subunit alpha-1 (*CBF-α-1*), a protein that in humans is encoded by the RUNX2 gene. The RUNX2 transcription factor has several upstream regulators and a variety of targets. Upstream factors are the Wnt/Notch system, Sox9, Msx2, and Hedgehog signaling [39].

Cofactors of Runx2 include Osx, Atf4, and others. Some paracrine and endocrine factors act as coactivators, especially bone morphogenetic proteins and parathyroid hormone [12] . The process is further refined by vitamin D and histone deacetylase [40]. Osteoblast differentiation is subject to regulation by physical stimuli to ensure the formation of bone suitable for structural and dynamic support for the body [41]. A brief description of the role of key genetic regulators, transcription factors and matrix proteins in osteoblast phenotype follows.

MSX2

MSX2 (Msh homeobox 2) is protein coding *MSX2* gene and is a decisive factor that promotes osteoblastic differentiation in conjunction with inhibition of adipogenesis in mesenchymal stem cells [42]. A marked slowing of ossification in cranial bones and a

general decrease in bone volume has been observed in mice following inactivation of Msx2. This phenotype is accompanied by a decrease in Runx2, suggesting that Runx2 expression may be regulated directly or indirectly by Msx2 [39].

Hedgehog

The Hedgehog (Hh) signaling pathway plays many important roles during development and postnatal tissue homeostasis, including bone formation [43]. negative and positive cellular regulation of Hh is controlled by two transmembrane proteins, Patched (Ptc), a negative regulator, and Smoothened (Smo), that stimulates downstream signaling in response to Hh [44]. Hh protein promotes differentiation of hMSCs into the osteoblastic lineage, increasing the alkaline phosphatase (ALPL) expression and *in vitro* mineralized matrix formation, which are markers of mature osteoblast function. Several developmental bone diseases are associated to a disruption of the Hh pathway [45].

WNT/NOTCH system

WNT is a paracrine glycoprotein that acts through multiple signaling pathways and it is important for osteoblast differentiation. WNT proteins interact with its cell surface receptor and transmit the signal into the cytoplasm. Once inside the cell, the signal is converted to β-catenin [46]. NOTCH is an intracellular signaling protein that promotes the degradation of β-catenin by counteracting WNT. Recent studies have shown that during intramembranous bone formation, NOTCH signaling controls osteoprogenitor cell proliferation, whereas activation of the WNT pathway regulates differentiation [47]. The imbalance between the WNT and NOTCH pathways results in ectopic mineralization [48].

DLX5

Distal-less homeobox 5 (DLX5) protein is considered an important regulator of bone formation but is not a specific marker for osteoblasts. It is an upstream regulator of RUNX2 and induces RUNX2-mediated expression of ALPL and osteopontin. Dlx5 is expressed from the earliest stages of embryonic bone formation [49]. Forced expression of DLX5 leads to an increased rate of mineralized matrix production in culture, but the effect of the protein on other osteoblast genes (osteocalcin) is highly inconsistent [50].

RUNX2

Runt-related transcription factor 2 (*RUNX2*) is the key control gene for osteoblast phenotype. It mediates the activation and/or temporal repression of cell growth and phenotypic genes during osteoblastic differentiation. Expression of *RUNX2* is observed in osteochondroprogenitor cells, early in skeletal development and then during later stages of osteoblast differentiation, with maximal expression in the mature osteoblast [51]. The target genes of RUNX2 include TGF-β receptor, ALPL, type I collagen α1 (COL1A1) and α2 chain (COL1A2), osteopontin, osteonectin, vitamin D receptor, bone sialoprotein, osteocalcin, and collagenase [39].

OSTERIX

Osterix (Osx or *SP7*) is one of the few osteoblast-specific genes. The gene was first identified in mouse models and later in its human homolog *SP7* in a variety of bone cell types and cell lines, such as MG63 and HOS [52,53]. Osterix acts downstream of RUNX2, which positively activates it, through interaction with a promoter of the gene itself. It is involved in the regulation of other osteoblastic genes such as osteocalcin, osteonectin, osteopontin, bone sialoprotein, and COL1A1 [54,55].

It is a downstream zinc finger transcription factor of WNT and can also inhibit it by acting as a negative feedback loop [56].

ATF4

Activation of transcription factor 4 (ATF4) belongs to the cAMP-responsive element-binding (CREB) transcription factor family. It interacts with RUNX2, promoting osteoblastogenesis and enhancing osteocalcin expression [57]. ATF4 is also required for the proper synthesis of COL1A1. It also regulates osteoclast differentiation and bone resorption through its expression in osteoblasts, where it binds to RANKL. RANKL binds to its RANK receptor on osteoclasts and triggers complex and diverse signaling cascades that control lineage engagement and osteoclast activation. [58].

ALPL

ALPL is a ubiquitous tetrameric glycoprotein located on the outer surface of cells. Specifically, in human bone, it resides on the outer membrane of osteoblasts. It serves to hydrolyze inorganic pyrophosphate to provide inorganic phosphate, which is required for hydroxyapatite synthesis [59]. Levels of this enzyme have also been shown to increase in response to mechanical forces. The total serum level of ALPL is an index of new bone formation and osteoblast activity. In fact, it is used as a diagnostic index to assess bone-forming capacity in osteoporosis. Clinically, loss of function in the liver/bone/kidney *ALPL* gene is associated with hypophosphatasia (HPP), a severe skeletal deformity characterized by loss of bone mass and subsequent fractures [60].

OPG

Osteoprotegerin (OPG) is a member of the tumor necrosis factor (TNF) superfamily, and it is an excretory cytokine produced by the osteoblasts. The protein acts as a soluble decoy receptor that reduces osteoclastogenesis by blocking the interactions of RANKL with its receptor (RANK) [61]. In normal individuals, the RANKL/OPG ratio is very low. Benign and malignant bone diseases could be associated to an abnormal RANKL/OPG ratio [62].

COL1A1

Collagen type I is formed by heterotrimers of two α1 (I) chains and one α2 (I) chain, encoded by *COL1A1* and *COL1A2* genes respectively. Collagen type I is a key component of the extracellular matrix of bone and forms associations with cell surface integrins and other ECM proteins. The imbalance of the normal ratio of α1- and α2-chains of type I collagen could lead to the formation of a more fragile collagen with more organic than inorganic components [63].

A common nucleotide substitution in the *COL1A1* gene results in less resistant bone mass synthesis, associated with osteoporosis. Expression of *COL1A1* is activated by RUNX2 binding to sites close to those for Osterix binds. Thus, overexpression of RUNX2 and Osterix has a cooperative effect on the expression of endogenous COL1A1 [64].

BGLAP

Osteocalcin is a 49 aminoacidic protein encoded by *BGLAP* gene (bone gamma-carboxy glutamic acid-containing protein). Osteocalcin is considered a specific marker of osteoblasts. It is highly expressed during the process of bone mineralization. After its release from osteoblasts, it is incorporated into the extracellular bone matrix. It constitutes approximately 15% of the non-collagenous protein fraction and is responsible for calcium and hydroxyapatite binding [65]. Osteocalcin incorporated into the bone matrix can be released during bone resorption as intact molecules and fragments. Thus, serum osteocalcin levels should be considered as a marker of bone turnover rather than bone formation. In fact, serum osteocalcin levels may be negatively correlated with metabolic syndrome [66].

OPN

Osteopontin (OPN) is a phosphoglycoprotein coded by phosphoprotein 1 (*SPP1*). RUNX2 and Osx are required for the activation of this gene and malfunctions within the gene encoding osteopontin can lead to tumorigenesis. As protein, osteopontin is

isolated from extracellular bone matrix, but it is also expressed by several cell types including osteoblasts, osteoclasts, macrophages, activated T lymphocytes, smooth muscle, epithelial and ganglion cells. Moreover, it is a structural component of some tissues such as bone marrow, placenta, kidney, and secretory epithelia [67].
In soluble form it is present in various biological fluids and actively participates in pathophysiological events such as bone remodelling, angiogenesis, scarring and some inflammatory processes of the osteo-skeletal system [68].

SPARC

SPARC (Secreted Protein Acidic and Cysteine Rich) is a gene that encodes for osteonectin, a phosphoprotein associated with the acid matrix rich in cysteine, the most abundant non-collagenous polypeptide expressed in bone [69]. Three transcription variants have been found for this gene that encode for different isoforms. It acts as a nucleation element for mineral crystals, as it is believed to be able to concentrate calcium in its vicinity, thus creating the conditions to initiate the precipitation of calcium phosphate [70]. The mature protein binds selectively to hydroxyapatite, collagen fibrils and vitronectin at distinct sites. It can allow proper organization of the bone matrix through contact with the cell surface. It appears to regulate cell growth through interactions with the extracellular matrix and cytokines. It is also involved in promoting changes in cell shape. Indeed, in some kinds of tumors, its upregulation has also been related to metastasis based on changes in cell shape that can promote tumor cell invasion [71].

TGF-β

Transforming growth factor-beta (TGF-β) stimulates matrix protein synthesis. The largest source of TGF-β in the body is found in bone (200 μg/kg of tissue), although the most concentrated source is in platelets [72]. TGF-β has multiple effects on bone cells depending on their phenotype and/or stage of differentiation. It can induce

osteoblastic differentiation or proliferation [73], it can inhibit osteoclastic precursor formation and, at high concentrations, isolated osteoclasts [74].

1.4.2 Paracrine and endocrine factors influencing osteoblastic differentiation

Bone Sialoprotein

BSP (bone sialoprotein) is a phosphorylated glycoprotein produced by activated osteoblasts and odontoblasts but it has also been found in osteoclastic and malignant cell lines [75]. It plays a significant role in extracellular matrix organization and cell-matrix adhesion processes. Indeed, this protein contains an Arg-Gly-Asp (RGD) integrin recognition sequence, which enhances the attachment of osteoblasts and osteoclasts to plastic surfaces. It also binds to the α2 chain of collagen, promotes nucleation of hydroxyapatite crystals *in vitro*, and it appears to increase bone resorption [76].

PTH

Parathyroid hormone (PTH) is fundamental for the calcium homeostasis and, it is one of the upstream regulators of *RUNX2* [57]. It thus contributes to the regulation of bone absorption. High levels of this hormone cause an increase in bone resorption. PTH receptor signaling in osteoblasts and osteocytes can increase the RANKL/OPG ratio, promoting osteoclast recruitment and activity. If the elevation is not continuous, the resorbed bone releases TGF-β and recruitment of new osteogenic progenitors occurs [4] .

Vitamin D

Vitamin D acts directly and indirectly on the bone. It acts directly on osteoblasts, osteocytes, and osteoclasts affecting the production of type I collagen and numerous non-collagen proteins (osteocalcin, osteopontin, BSP). Under the influence of vitamin D, osteocytes produce phosphatonin (FGF-23, Fibroblast growth factor 23), which

regulates the renal hydroxylation of 1,25-$(OH)_2$ vitamin D3, inhibits phosphate reabsorption and reduces PTH synthesis. It stimulates the preosteoblasts to secrete the M-CSF, which in turn activates the proliferation of preosteoclasts and prevents their apoptosis. It causes increased RANKL expression in osteoblasts and inhibits OPG expression, thus stimulating osteoclastogenesis [77].

As mentioned above, vitamin D has an indirect action on the bones by regulating the body's calcium and phosphate metabolism. Indeed, it acts on the intestinal epithelium to regulate calcium absorption and interacting with PTH to stimulate the reabsorption of calcium and phosphate in the kidneys from tubular fluid into the blood [78].

1.5 Stage of osteoblastic differentiation

The osteoblastic differentiation starts from mesenchymal stromal cells (MSCs), that can give rise to myoblasts, osteoblasts, chondrocytes, or adipocyte lineages. The commitment of MSCs to the osteoprogenitor lineage requires the expression of specific genes, as previously described. The osteogenic differentiation proceeds through a series of steps (**Fig. 3**).

In stage 1, cells proliferate and express collagen, TGF-β receptor 1, osteopontin, and fibronectin, another ECM protein able to bind growth factors relevant for bone regeneration. In stage 2, they exit the cell cycle and begin to differentiate, and there is the expression of RUNX2, DLX5 and SP7, crucial for the differentiation of osteoblasts [73]. Furthermore, *COL1A1*, *ALPL*, *BSP*, *BGLAP* genes are upregulated by RUNX2. At this stage, osteoblast progenitors exhibit ALPL activity and are considered pre-osteoblasts. In stage 3, the pre-osteoblasts become mature osteoblasts, and there is an increase in SP7 expression and secretion of bone matrix proteins such as BSP, COL1A1 and BGLAP that stimulate mineral matrix deposition. At this stage, the osteoblast assumes its characteristic cuboidal shape [79]. During the bone formation process, between 5% and 20% of osteoblasts become osteocytes, reducing up to 70%

of their cellular body, when osteocyte maturation is complete. Part of the osteoblasts can undergo apoptosis or become quiescent, that is, lining cells along the bone surfaces [80].

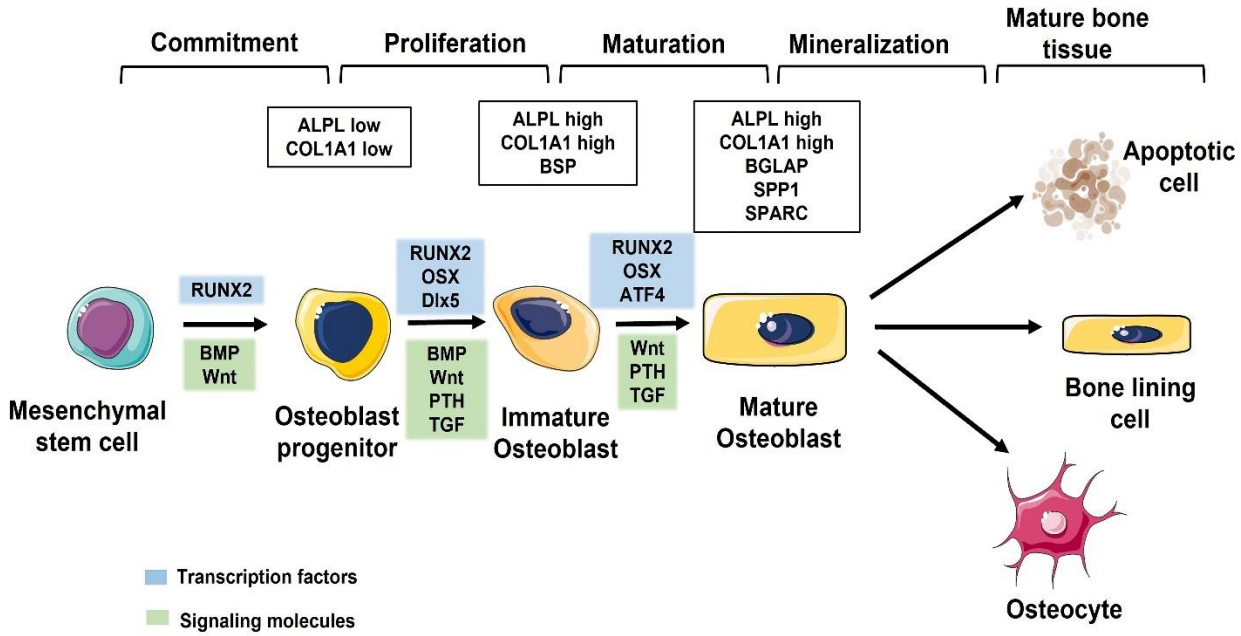

Figure 3 Osteoblastogenesis and fate: diagram illustrating the origin of osteoblasts, the main transcription factors and signaling molecules involved in their proliferation and differentiation. Upon completion of bone formation, mature osteoblasts may flatten to cover the quiescent bone surface as lining cells, die for apoptosis, or become osteocytes.

The figure was modified from Servier Medical Art by Servier is licensed under a Creative Commons Attribution 3.0 Unported License (https://smart.servier.com/).

1.6 Bone Remodeling Process

Bone remodeling is a lifelong physiological process based on a complex cell-bone crosstalk. It consists of several phases in which the osteoclasts reabsorb the bone which is replaced by new tissue formed by osteoblasts (**Fig. 4**) [13].

Osteoblasts secret the constituents of extracellular organic matrix, as mentioned above. Once the extracellular matrix is secreted, it undergoes mineralization. Primary mineralization by deposition of hydroxyapatite crystals begins about two weeks after

unmineralized matrix (osteoid) is laid down by the osteoblasts and continues for about six months. The spawning of young mineral crystals continues slowly for months with incorporation of more mineral and development of crystal structure (secondary mineralization). The osteoblasts, recalled in the bone formation sites by cytokines and growth factors, after the secretion of the matrix, remain incorporated in it, taking the name of osteocytes. The body of osteocytes remains enclosed in a niche carved into the intercellular substance, the bone gap, while the extensions are housed inside the thin bone canaliculi [79]. The signal to initiate remodelling may be endocrine, such as increased PTH in response to hypocalcaemia, which leads to a generalized increase in osteoclast activation [57]. Localized remodelling is initiated in response to microdamage, by signals from osteocytes. The molecules responsible for the interaction between these different cell types, and therefore for the balance between the two processes (resorption and renewal) are numerous proinflammatory cytokines (IL-6, TNF-α and IL-1). They stimulate osteoclastogenesis and proteins such as OPG, the NFk-β activating receptor RANK and the RANKL, which represent a key triad of bone biology [81].

Osteoblasts produce osteoclast activators, RANKL, and M-CSF, both by directly secreting proteolytic enzymes and cleaving the organic component. Among these, collagenase is secreted in an inactive form (procollagenase) and made operative in the extracellular environment after proteolytic cleavage by plasmin. Collagenase works by removing the layer of non-mineralized osteoid tissue that covers the surface of the bone, allowing the osteoclasts to adhere to the mineral matrix and dissolve it. Active bone resorbing osteoclasts show cellular polarization with the apical membrane consisting of the clear zone (or sealing zone, SZ) and ruffled edge and a basolateral plasma membrane [82]. The SZ is the bone attachment site that delineates the bone resorption space where the ruffled edge is formed. The SZ appears as a filamentous actin ring (F-actin also called an actin ring or podosomal belt), with the podosomes acting as focal adhesion points. It serves to isolate the compartment that reabsorbs the

bone from the extracellular fluid [83]. The actual bone resorption process is a two-step process, which begins with the dissolution of the mineralized part, followed by the enzymatic degradation of the organic matrix. At the level of the sealed area, the osteoclast carbonic anhydrase II (CA II) converts CO_2 and H_2O into H^+ and HCO_3^-. H^+ is transported across the ruffled border into resorption lacuna by a vacuolar type H^+-ATPase [84]. The resulting lowering of the pH leads to the dissolution of the apatite crystals. At the same time, the osteoclasts evocate the content of lysosomal enzymes such as hydrolases which are activated at low pH and digest the organic components of the bone matrix. The lytic action of osteoclasts is manifested by the formation of Howship lacunae. Once the gap is formed, the osteoclasts detach from the matrix, move to the portion of bone adjacent to the reabsorbed one, starting the formation of a new gap. Osteoclastic function is finely regulated by local and hormonal factors. These are the only bone cells that possess the receptor for calcitonin, a hormone produced by the parafollicular cells (C cells) of the thyroid and PHT antagonist. Calcitonin is an inhibitor of bone resorption as it is able to induce the detachment of osteoclasts from the bone, the disappearance of the brush border and the reduction of cellular metabolism. The receptor for the molecule is already expressed in the circulating precursors of osteoclasts, so much so that it is used as a discriminant for the identification of this cell type [85,86].

Bone remodelling has a circadian rhythm. Bone resorption increases at night and decreases during the day. The pace is driven by a combination of endocrine factors (which may include cortisol, oxytocin, and melatonin), local factors (such as the peroxisome proliferator-activated g receptor, PPARG), and clock genes [87].

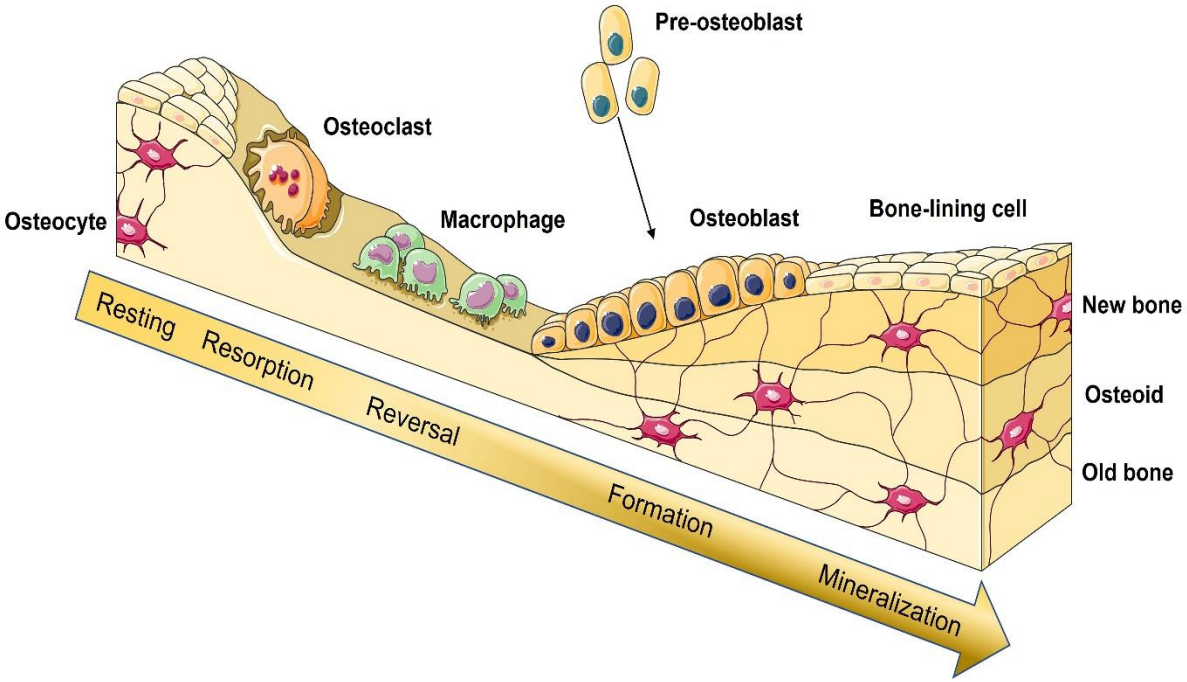

Figure 4 Bone remodeling process involves the following steps: resorption, reversal, formation, mineralization and resting. Osteoclasts and osteoblasts work together to maintain the balance between bone loss and bone formation. *The figure was modified from Servier Medical Art by Servier is licensed under a Creative Commons Attribution 3.0 Unported License (https://smart.servier.com/).*

1.7 Bone mineralization

Biomineralization (BM) is a lifelong process that is essential in bone formation and repair. Mineralization is a highly controlled process, absent in tissues other than bone, during which ions (calcium, magnesium, zinc, phosphate...) are converted into biominerals that nucleate and grow within an organic matrix structure [3].

Osteoblasts are the cells responsible for the synthesis of the extracellular matrix, a complex structure consisting of collagen microfibrils that direct the formation of nanometer-sized HA platelets oriented parallel to the axis of the collagen fibrils, for interfibrillar mineralization [88]. To induce cell-mediated mineralization, the organism must create an environment in which the balance between Ca^{2+} and PO_4^{3-} is disturbed, leading to the precipitation of a $Ca_x(PO_4)_y$ complex. In physiological mineralization this nucleation process occurs through several cooperative mechanisms, in which there

is careful interaction between structures that initiate mineralization and molecules that suppress it [89,90].

In the last decades, several researchers have proposed various mechanisms to explain early bone mineral formation, but many aspects remain unclear.

One of the hypothesized mechanisms to trigger BM provides for the involvement of ALPL. It facilitates bone ECM mineralization in two ways: first, it reduces the level of inorganic pyrophosphate (PPi), an inhibitor of mineralization, and second, it generates inorganic phosphate (Pi), an activator of ECM mineralization. This coupled activity of ALPL alters the Pi/PPi ratio in the bone microenvironment to promote bone mineralization [91].

An alternative pathway involves amorphous mineral precursors being transiently produced and deposited within collagen fibrils. The compact hierarchical assembly of collagen molecules in fibrils and fibers results in nanoscale gaps both intra- and interfibrillar. These gaps are accessed by Ca^{2+} and Pi ions, which cluster as amorphous calcium phosphate (ACP) and where they transform into more crystalline apatite platelets [30,92].

An auxiliary mechanism for bone mineralization involves vesicular bodies. Portions with a diameter ranging from 30 to 300 nm, called matrix vesicles (MVs), are released from the apical membrane domain of osteoblasts. Within these vesicles, enzymes such as sphingomyelin phosphodiesterase 3 (SMPD3) and phospholipases cleave phospholipids (sphingomyelin [SM]) to generate phosphocholine, which in turn can be cleaved by another cytosolic enzyme orphan phosphatase 1 (PHOSPHO1) releasing free Pi. An increase in intravesicular Pi leads to its precipitation with Ca^{2+} to form first ACP and then nascent HA crystals [93].

Boonrungsiman et al. suggested another model, according to which amorphous calcium phosphate is stored in mitochondria and are transported via vesicles to the ECM before converting to a more crystalline form of apatite. The authors observed calcium-containing vesicles joining the mitochondria, which also contained calcium,

suggesting a mechanism of storage and transport. Probably, ionic calcium (and phosphate) is transferred from mitochondria to intracellular vesicles, through a direct process such as diffusion [94].

More recently, Tang et al. have proposed the ER as initiating site for mitochondrial mineral precursors. According to this process, calcium and phosphorus clusters are generated on ER membranes and then transported into mitochondria [95].

The different hypothesises about the biomineralization mechanisms have been graphically summarized in **Fig. 5**.

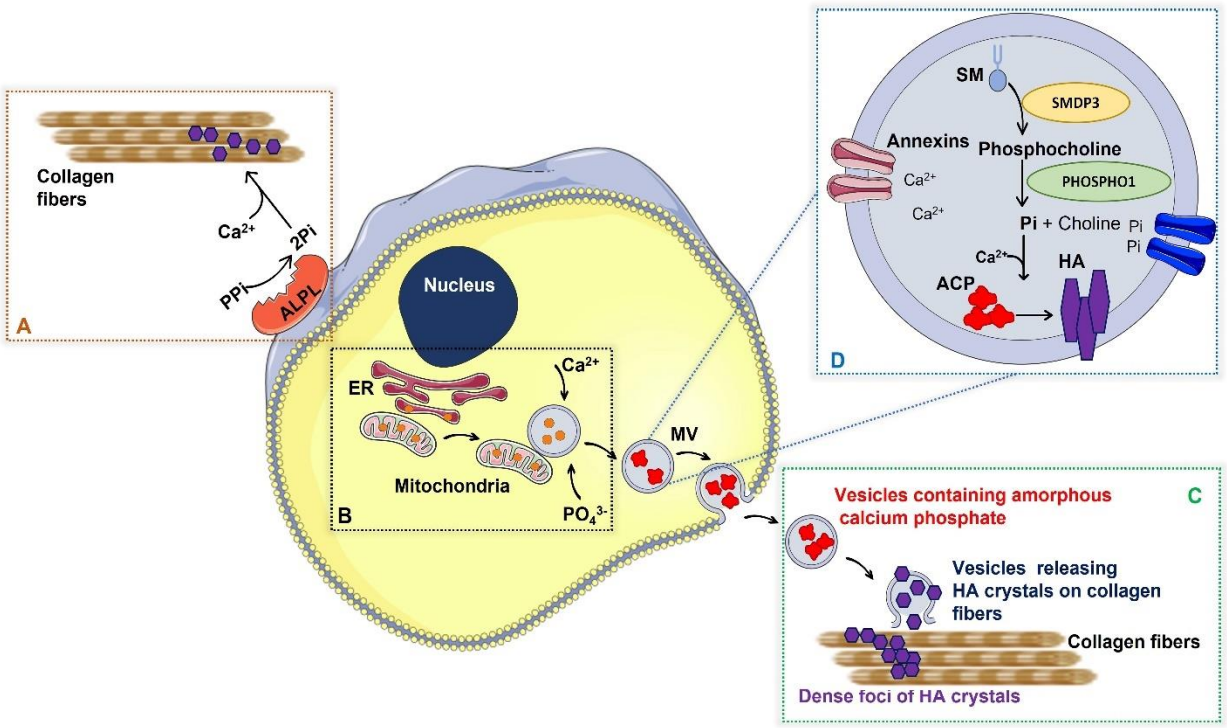

Figure 5 Graphic summary of current proposed mechanisms for bone biomineralization. (A) Alkaline phosphatase (ALPL), tethered to the osteoblast cell membrane, cleaves PPi into Pi. Simultaneously, compact hierarchical assembly of collagen fibers results in both intra and interfibrillar nanoscale gaps, accessible by Ca^{2+} and Pi ions that crystalize into HA (hexagonal violet shapes) [91]. (B) Calcium and phosphorus clusters (orange spots) are generated on the ER membranes and are transported into the mitochondria [95]. Additionally, calcium and phosphorus clusters stored in mitochondria are transported via vesicles to the ECM [94]. (C) Matrix vesicles bud from the plasma membrane and accumulate ACP extracellularly. Before associating with the collagenous ECM, ACP is converted to crystalline apatite and propagates from dense foci. (D) Matrix vesicles (MVs) contain enzymes such

as SMPD3 able to cleave SM to generate phosphocholine, which in turn can be cleaved by PHOSPHO1 releasing free Pi. Such an increase in intravesicular Pi leads to its precipitation with Ca^{2+} ions (transported by annexins) to form ACP and then nascent HA crystals [93].

The figure was modified from Servier Medical Art by Servier is licensed under a Creative Commons Attribution 3.0 Unported License (https://smart.servier.com/).

1.8 Osteosarcoma

Osteosarcoma (OS) is an osteoid-producing malignant tumor of mesenchymal origin, usually accompanied by lung metastasis. While primary bone cancers represent less than 0.2% of all cancers, their frequency has been increasing by 0.3% per year over the last decade [96]. It is the most common malignant primary bone tumor and occurs most frequently in patients between 5 years of age and early adulthood. The incidence peak in the older (>65 years) populations has been associated with pre-existing Paget's disease and prior radiation therapy [97].

Studies have shown that OS possesses various cytogenetic and genetic abnormalities [98]. OS etiology, as well as the molecular pathogeneses and genetics of OS are wide and extremely heterogeneous [96]. The most commonly dysregulated genes in osteosarcoma are p53 such as in Li-Fraumeni syndrome and *RB1* gene as in retinoblastoma caused by inherited alteration of this tumor suppressor [99]. Other alterations have been identified in MDM2 (negative regulator of the p53 tumor suppressor), β-catenin, and pathways related to cell proliferation and genome stability [100]. Most of osteosarcomas are not caused by inherited gene mutations, but by gene changes caused by radiation therapy used to treat previous form of cancer [101]. Several studies pointed out that OS development may be associated with defects in osteogenic differentiation, being associated with high cell proliferation [102].

Osteosarcoma originates systematically from MSCs of the osteoblastic differentiation pathway [103]. OS cells express typical markers of osteoblast cells (alkaline phosphatase, osteocalcin and/or bone sialoprotein) and the resultant tumor is

characterized by the presence of a mineralized osteoid-type matrix, according to its degree of differentiation [104].

Several OS types exist and they can be divided into osteoblastic, chondroblastic and fibroblastic subtypes [105].

An *osteoblastic subtype* is seen with the most differentiated cells; in this case, OS cells produce copious quantities of osteoid matrix that is organized in a complex trabecular structure, often external to the normal bone and described as a "sunburst" pattern (due to expansion of the tumor, mineralization and formation of periosteal spicules or "streamers") when seen on radiography.

A *chondroblastic OS subtype* results from mutation in less differentiated cells, where OS cells produce a more cartilaginous matrix in addition to the osteoid matrix as is reminiscent of endochondral ossification. The last subtype is a *fibroblastic OS*, which arises from the least differentiated OS cells and gives a morphology reminiscent of fibroblastic matrix tissue [106,107].

OS is also subclassified based on grade of malignancy as low-grade and high-grade [108,109]. While the prognosis for low-grade OS is usually favourable and most patients are treated only with surgery, long-term clinical outcomes of high-grade OS are much less satisfactory [110]. High-grade OS is a malignant aggressive primary bone tumor that commonly arises in the long bones of children and adolescents.

The high heterogeneity in OS due to its histological heterogeneity and the instability of its genetic makeup [107], as well as the rarity of the disease, have limited therapeutic developments and new discoveries.

Current treatment involves combined approach with neoadjuvant chemotherapy followed by surgery. The chemotherapy-based treatments remain the same since around the 1970s, with doxorubicin and methotrexate being the main drugs of choice, with cisplatin and ifosfamide later added [111,112].

This toxic cocktail of DNA intercalators, DNA/RNA synthesis inhibitors and alkylating agent improve the 5-year disease-free survival of OS patients [113].

However, clinical treatment faces numerous difficulties, including the adverse effects of chemotherapies, chemoresistance, and recurrence [114]. Most of research activity is focused on the investigation of alternative treatments capable of overcoming these defects. In this light, differentiation therapy is viewed as a challenge in osteosarcoma treatment research. It represents the use of agents that can induce differentiation in neoplastic cells, with the irreversible loss of tumor phenotype. The understanding of the relationship between defects in osteogenic differentiation and tumor development holds tremendous potential for treating OS. Nowadays, several differentiative treatments have been clinically tested for several types of sarcomas, and they are currently in preclinical screening for OS [115]. Among the most promising drugs in the differentiative arsenal for OS are metformin and pioglitazone because there is extensive data on their safety, and preliminary data on the additive effect with chemotherapy are available [116,117]. Thiazolidine, pioglitazone and troglitazone are a family of drugs that are PPARγ agonists and are currently used as anti-diabetic drugs treating millions of patients worldwide. Most of these agents are able to sensitize OS cells to chemotherapy. Moreover, the cells that survive chemotherapy can be induced to differentiate, acquiring a non tumor phenotype.

1.9 Osteoblast cell models in vitro research

The *in vitro* study of osteosarcoma is carried out by different types of cells. In the era of intensive bone tissue engineering research, a plethora of osteosarcoma-derived cells are commonly used as osteoblastic models due to limited availability of primary human osteoblast cells [118]. Human bone marrow mesenchymal stem cells (hbMSCs) are excellent model systems, but scarcity, heterogeneity and limited lifespan restricted their use [119]. Undifferentiated human fetus osteoblast (hFOB) cells possess similar markers as hbMSCs and are widely used as a model of normal osteoblastic differentiation [120].

Various methods have been developed for the isolation of primary human osteoblasts from bone explants, including enzymatic digestion and spontaneous culture of bone fragments, but are more difficult to obtain. Moreover, it has been demonstrated that behaviour and characteristics of human osteoblastic cells are affected by factors such as site of isolation, age of the individual and gender differences. For all these reasons in general osteosarcoma cell lines are preferred and chosen as osteoblastic models. The use of immortalized cell lines possesses several advantages: ease of maintenance, unlimited number of divisions (avoid new isolations) and relative phenotypic stability. On the other hand, the disadvantages may arise from: i) heterogeneous populations in the same line (different cell cycle phase), ii) full range of phenotypic characteristics of the original cells not expressed; iii) not physiological proliferation (loss of contact inhibition) [121–123].

The available *in vitro* culture models include immortalized cell lines derived from varied species (human, rat, mouse, bovine, ovine and rabbit), malignant cell lines, and more recently pluripotent stem cells induced to differentiate [121,124].

The most used animal cell lines are mouse pre-osteoblast MC3T3E1 [125], and rat osteosarcoma cells ROS 17 / 2.8 or UMR106.01 [126].

The first human cell line used was U2OS in 1964, isolated from the tibia of a 15-year-old female [127] and was followed by the HOS-TE85 cell line derived from a 13-year-old female in 1971 [128,129] -HOS, KHOS and 143B cell lines derived from the parental cell line HOS-Te85 [130–135], the SaOS-2 cell line derived from an 11-year-old female [136] and the MG-63 cell line derived from a 14-year-old male [137,138]. Several differentiation markers of osteoblasts have been demonstrated in these osteosarcoma cell lines. MG-63, Saos-2 and U-2 OS, cells revealed an osteoblastic labelling profile [139]. They are able to secrete MVs [140] and are good *in vitro* models of human osteoblast-like cell implant materials [119].

The origin and major features of commonly used human osteosarcoma cell lines were briefly described in **table 1**. A deeper description of SaOS-2 cell line is reported in the following paragraph.

Table 1 - Commonly used human osteosarcoma cell lines.

cell line	*year*	*gender*	*age*	*phenotype*	*Features*	*References*
HOS-TE85	1971	female	13	Immature osteoblast	Mixed fibroblast and epithelial like cells with flat morphology, sensitive to chemical and viral transformation; higher levels of ALP activity than MG63 cells, low osteocalcin expression.	[128,129]
MNNG-HOS	1975	female	13	Osteolytic/osteogenic	Derived from HOS-TE85 by transformation with 0.01 mcg/ml h N-methyl-N'-nitro-N-nitrosoguanidine (a carcinogenic nitrosamine). This cell line is not as aggressive as 143B but is more aggressive than the HOS-TE85 parental cell type.	[130,131]
KHOS	1975	female	13	Osteolytic/osteogenic	Cell line produced by the transformation of HOS cells by the Kirsten murine sarcoma virus (K-MSV) which carries the K-ras oncogene	[132,133]
143B	1979	female	13	Osteolytic	K-Ras oncogene transformed HOS-Te85 derivative; highly tumorigenic and metastatic	[134,135]
U2OS	1964	female	15	Very early osteoblast/fibroblastic	Negative for almost all osteoblastic markers, positive for cartilage markers like collagen II, IX, X. and for type IV collagen, Not consistently classified as osteoblastic, but also as fibroblastic.	[127,139]
MG-63	1977	male	14	Immature osteoblast	Sensitive to hormonal administration, low ALP enzyme activity, low mineralisation capabilities of monolayer.	[129,139]
SaOS-2	1973	Female	11	Mature osteoblast	Cytokine and growth factor expression profile similar to human osteoblast cells, sensitive to hormonal administration, high ALP, and mineralizing activity.	[136,140]

1.9.1 Characteristics of SaOS-2 cell line

SaOS-2 cell line has been widely used as an *in vitro* model with "normal" osteoblast behaviour. Rodan and colleagues characterized the osteoblastic properties of the human osteosarcoma cell line SaOS-2, which were isolated from an 11-year-old Caucasian female in 1975 [136]. These cells have a mature osteoblastic phenotype with a much higher level of ALP activity (4-6 μmol / mg / min) than other OS cell lines, such as MG-63 and SaOS-1 (2.5 nmol / mg / min). The ALPL level is comparable, at least in the early moments of culture, to human osteoblastic cells [121,141] but increased 120-fold after 14 days of cell culture under the same conditions [142]. ALP in SaOS-2 cells can be further stimulated by dexamethasone and by phosphate substrates, producing more different phenotype [141,143].

Interestingly, SaOS-2 cells form a calcified matrix typical of intertwined bone [136]. A detailed analysis of the collagen structure synthesized by SaOS-2 revealed that it is similar to collagen formed by human primary osteoblastic cells but with a higher level of lysyl hydroxylation [144]. Regarding the expression of osteoblastic markers, SaOS-2 cells expressed the osteoblastic markers osteocalcin, bone sialoprotein, and procollagen-I. Type III collagen and osteoprotegerin can only be detected in about 15% of cells, the expression of cytokines and growth factors is similar to that of osteoblasts. Furthermore, the expression of cytokines and growth factors of SaOS-2 cells has been shown to be like normal primary human osteoblastic cells [145], as well as the expression of receptors for PTH and calcitriol and the expression of COL1A1, which is upregulated during the preliminary stages of differentiation, and decreases upon mineralization [141].

However, unlike osteoblasts, most have tested positive for type IV collagen and some genes usually present in osteocytes which increased as a function of culture time. The most important alterations of the line, however, resulted from the expression of MMP-9 and type X collagen. Therefore, its differentiation capacity and its similarity to the

ROS 17 / 2.8 rat OS cell line show that the line is a good model for studying the differentiation of human osteoblasts *in vitro* [136,139,146].

1.10 3D cell cultures

Cell cultures represent a valuable *in vitro* tool to deepen our understanding of cell biology, tissue morphology and disease mechanisms, drug action, and protein production.

Two-dimensional (2D) cell cultures since the early 1900s have been the most widely used method to culture cells. They have several advantages associated with the simple and low-cost maintenance of the cells and the possibility to perform simple functional tests. However, they also have many limitations: the impossibility of faithfully representing cell-cell and cell-extracellular interactions; any changes in cell morphology, in cell division mode and the loss of polarity following isolation [147].

Currently, much more advanced experiments can be performed using new culture methods known as three-dimensional (3D) cell culture. In these systems, the cellular environment can be manipulated to mimic that of an *in vivo* cell. Moreover, 3D cell cultures provide more accurate data on cell-cell interactions, metabolic profiling, cell behaviour in the tumor microenvironment, but also on stem cells and several types of diseases [148]. 3D cell cultures represents an alternative system to study organs with the goal of reducing the gap between 2D cell culture and animal models [149].

Depending on the method of preparation, 3D models can be divided into i) suspension cultures on non-adherent plates; ii) cultures in concentrated medium or in gel-like substances¸ and iii) cultures on a scaffold. The different technical approaches to obtaining 3D models possess their advantages and their limitations. The proper choice of 3D system mostly depends on the research area.

In the wider and multidisciplinary field of investigation of tissue engineering (TE), the use of 3D scaffolds constitutes an alternative and promising approach for grafts, i.e.,

autografts, allografts, and xenografts, especially for studying of bone and for repairing its damages.

1.10.1 Biomaterials for bone tissue engineering

Tissue engineering focuses on providing appropriate solutions that enable the repair or replacement of damaged tissues by highly porous scaffold biomaterials [150]. Scaffolds are 3D fabricated structures consisting of a series of materials to which cells and occasionally growth factors are added. They are often used in conjunction with a bioreactor, a device or system capable of applying several types of mechanical or chemical stimuli to cells. Characteristics such as porosity, permeability, surface nature, and mechanical stability are modulated to design an architecture that is representative of the microenvironment of the tissue being mimicked and able to providing a model for the formation of the tissue itself [151].

Several factors must be considered when designing or determining the suitability of a scaffold for use in tissue engineering. Firstly, the *biocompatibility* must be considered: any tissue-engineered scaffold must support cell adhesion, migration on the surface and across the scaffold, and their normal function and ability to lay down new matrix. Secondly, the *biodegradability* must be taken into account scaffolds are not intended to be permanent implants but must be biodegradable. Cells must be able to produce their own extracellular matrix and degrade the existing matrix. The products of this degradation should also be non-toxic.

Next, the *mechanical properties* represent a key figure to consider. The scaffold must have mechanical properties consistent with the anatomical site in which it is to replicate or in which it is to be implanted. Producing scaffolds with appropriate mechanical properties is one of the great challenges in attempting to engineer bone or cartilage.

Finally, the *scaffold architecture* must be regarded. The scaffolds should have an interconnected pore structure and high porosity to ensure cellular penetration, adequate diffusion of nutrients and at the same time must allow waste products to diffuse out of

the scaffold. The size of the pores may vary depending on the type of cells used and the tissue to be engineered.

The choice of the biomaterial is fundamental to determine the characteristics of the scaffold and is made considering all the previous criteria.

The European Society for Biomaterials (ESB) defines a biomaterial as a "*material intended to interface with biological systems to evaluate, treat, augment or replace any tissue, organ or function in the body*". Three types of polymers are used to produce scaffolds: synthetic, natural, and ceramic [152].

The most used synthetic polymers include polystyrene, polylactic acid (PLLA), polyglycolic acid (PGA), and poly-lactic-co-glycolic-acid (PLGA). The disadvantage of these materials is related to their degradation process. PLLA and PGA degrade by hydrolysis, producing carbon dioxide and thus lowering the local pH, which can cause cell and tissue necrosis.

Among natural hydrogels collagen, gelatin, various proteoglycans, alginate-based substrates, and chitosan are used. Unlike synthetic polymers, natural polymers are biologically active and promote excellent cell adhesion and growth. Another advantage is their biodegradability, so they allow host cells, over time, to produce their own extracellular matrix and replace the degraded scaffold. However, the fabrication of scaffolds from natural polymers with homogeneous and reproducible characteristics is still a challenge. In addition, natural polymer scaffolds have poor mechanical properties, which limits their use, for example, in load-bearing orthopedic applications [153].

For improving the mechanical strength and the osteoconductive properties, inorganic materials (bioceramics) are applied in bone tissue engineering. These materials could be divided into *bioinert* and *bioactive* ceramics. The characteristics of bioinert ceramics are high mechanical strength, outstanding biocompatibility, and chemical stability, while bioactive ceramics have a good biocompatibility and degradation ability in physiological environment and a good bioactivity *in vitro* and *in vivo* [154].

To enhance the mechanical properties of different polymers, to utilize their excellent characteristics and to increase tissue interaction, scaffolds consisting of natural or synthetic polymers combined with ceramics have been developed. The aim is to provide sufficient architecture and rigidity for the tissue to replace, surpassing the limit of using a single polymer.

In the composite scaffolds the bioactive glasses are characterized by a similar mechanical stiffness (elastic modulus about 40 GPa) as cortical bone (about 20 GPa). In addition, they exhibit excellent biocompatibility due to their chemical and structural similarity to the mineral phase of native bone. On the other hand, synthetic polymers have lower strength values (about 10 GPa), and natural polymers even lower (about 70 Mpa).

Another notable application of scaffolds is their use as supporting materials for different drug loadings (growth factors or antibiotics) , allowing for the sustained and controlled release of drugs over the desired time period and improving bone ingrowth, bone healing, and the treatment of tissue defects [150].

1.11 Instrumental methods of investigation

The analysis of complex systems, such as biological samples, requires the use of different approaches to obtain an overview of the phenomenon of interest.

In this regard, microscopy and spectroscopy are great tools for analysis singly, but when combined they can yield even more powerful results.

In recent years, the need to imagine the detailed relationship between structure and function, at various levels of resolution and length scales, has led to the development of increasingly performing imaging studies, often combining two-dimensional and 3D microscopic techniques. Over the years, new microscopic techniques have been added to optical microscopy, such as electron microscopy and X-ray transmission microscopy which, under the most favourable conditions, are able to resolve single elements with

a resolution of a few nanometres. In addition, the spectroscopic analytical techniques based on the interaction between electromagnetic radiation and matter offer a series of advantages (sensitivity, safety, non-invasiveness and/or remote access, miniaturization, little or no sample preparation).

Below is a brief overview of the different microscopic and spectroscopic approach used for this thesis project.

1.11.1 Electron-transmission microscopy (TEM)

TEM was discovered in 1931 by Ernst Ruska and Max Knolls.

In this kind of microscope, a thin electron beam is created by a high-voltage tungsten filament and focused by magnetic lenses. As the electron beam passes through the sample, electron particles begin to scatter. The electromagnetic lens of the EM (Electron Microscopy) focuses the scattering electron onto a screen and creates a highly magnified and detailed black and white image of the sample. During transmission, the speed of the electrons is related to the wavelength of the electron. At shorter wavelengths, the electrons move faster, and the quality and detail of the image will be greater. The lighter areas of the image represent the points where more electrons have passed through the sample, and the darker areas reflect the denser areas of the object, therefore traversed by fewer electrons. These differences provide information about the structure, texture, shape, and size of the sample. To achieve good TEM analysis, samples must have certain properties. They must be thin (<100 nm) so that electrons can pass through, a property known as electronic transparency [155].

TEM has provided a better understanding of the structure and organization of the components of tissues, cells, and organisms than a simple microscope. This technique offers several advantages, first their high-resolution power, they also have a wide range of applications and can be used in a variety of different scientific fields. The use of this technique depends on certain characteristic of the sample: transparency, size, and

ability to tolerate vacuum. Among the disadvantages there is certainly the sample preparation with the consequent risk of artifacts [155].

1.11.2 Synchrotron-based techniques

The application of new powerful and unconventional techniques based on synchrotron light is now having a significant impact in many areas of physics, chemistry, materials science, and engineering, as well as other sciences, such as life sciences and medicine. The synchrotron is a circular accelerator of particles (such as electrons and ions) that move at speeds close to that of light and, traveling in a tangential direction to the synchrotron orbit, generate an electromagnetic wave called synchrotron radiation (**Fig. 6**). This radiation is highly polarized and continuous. Its intensity and frequency are related to the intensity of the magnetic field in vacuum and the energy of charged particles affected by the field. Consequently, the stronger the magnetic field and the greater the energy of the particles, the greater will be the intensity and frequency of the emitted radiation. A synchrotron radiation system typically consists of (a) an electron accelerator (cannon), to accelerate electrons to a given energy (about hundreds of MeV to multi-GeV); (b) a high vacuum storage ring, in which accelerated electrons are injected in the form of pulses (clusters); and (c) magnetic field devices, such as bending magnets, oscillators, and undulators, to tune the emitted light and conduct it to the beamlines. In addition, SR structures enable wavelength and spot selection using devices such as slits, mirrors, and monochromators. The emitted spectrum is broadband from the microwave (pilot RF field harmonics) to the X-ray spectral regions. A particular advantage of synchrotron radiation sources over conventional X-ray sources is their extremely high brilliance. Brightness is expressed as the number of photons emitted per unit area of the source over a unit angle of emission and per unit energy (photons s^{-1} $mrad^{-2}$ mm^{-2} per 0.1% of the radiation bandwidth). Because of its high intensity and directionality, SR can provide micro and nano X-ray beams with flux

densities greater than 10^{13} photons/s^{-1}, for example, using broadband nano-focusing X-ray optics [157].

Synchrotron light has many advantages, which make it much more powerful for some biological applications than the laboratory source. By achieving submicrometric resolutions, synchrotron-based techniques allow the analysis of single cells, helping to elucidate their structure and the distribution, concentration, and chemical state of metals at the organelle level [158].

To date, there are numerous techniques that exploit the interaction phenomena between SR and matter, such as absorption and scattering. Fourier transform infrared spectroscopy (FTIR), X-ray absorption spectrometry (XAS) and X-ray computed tomography (X-CT), etc. are based on the absorption of synchrotron radiation by matter. X-ray diffraction (XRD) and small-angle X-ray scattering (SAXS), etc. rely on the scattering of synchrotron radiation. In contrast, other techniques exploit the detection of secondary particle emission such as X-ray fluorescence spectrometry (XRF) and X-ray photoelectron spectroscopy (XPS).

The following is a brief review of synchrotron-based techniques used for this thesis project purposes.

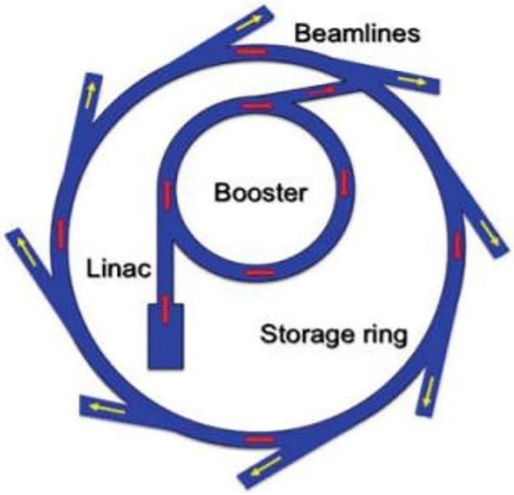

Figure 6 Schematic planar view of a synchrotron radiation facility. Electrons are first accelerated in the linear accelerator (linac) and in a booster synchrotron, and then they are injected into a storage ring.

1.11.2 Synchrotron X-Ray fluorescence microscopy

Synchrotron X-ray Fluorescence Microscopy (XRFM) is a powerful technique that harnesses the spectrally pure and finely focused X-ray beam from a synchrotron, allowing the identification of the elemental composition and quantitative analysis of a wide range of inorganic materials that are present in, or make up, the sample examined [159].

In the XRFM process a photon is absorbed by an atom creating a hole (lacunae) in the atom with the ejection of an electron. Electron cascading from outer electron shells fill the electron gaps created by the incoming photon. These have higher energy states than the inner shell electrons, and the rearrangement of the electrons causes the emission characteristic X-Ray fluorescent photon (**Fig. 7A**). X-ray fluorescence lines are historically named with the letter K, L or M, which indicates which shell had the original vacancy. While the subscript alpha (α) or beta (β) indicates which outer electron fill the lacunae (**Fig. 7B**) [160].

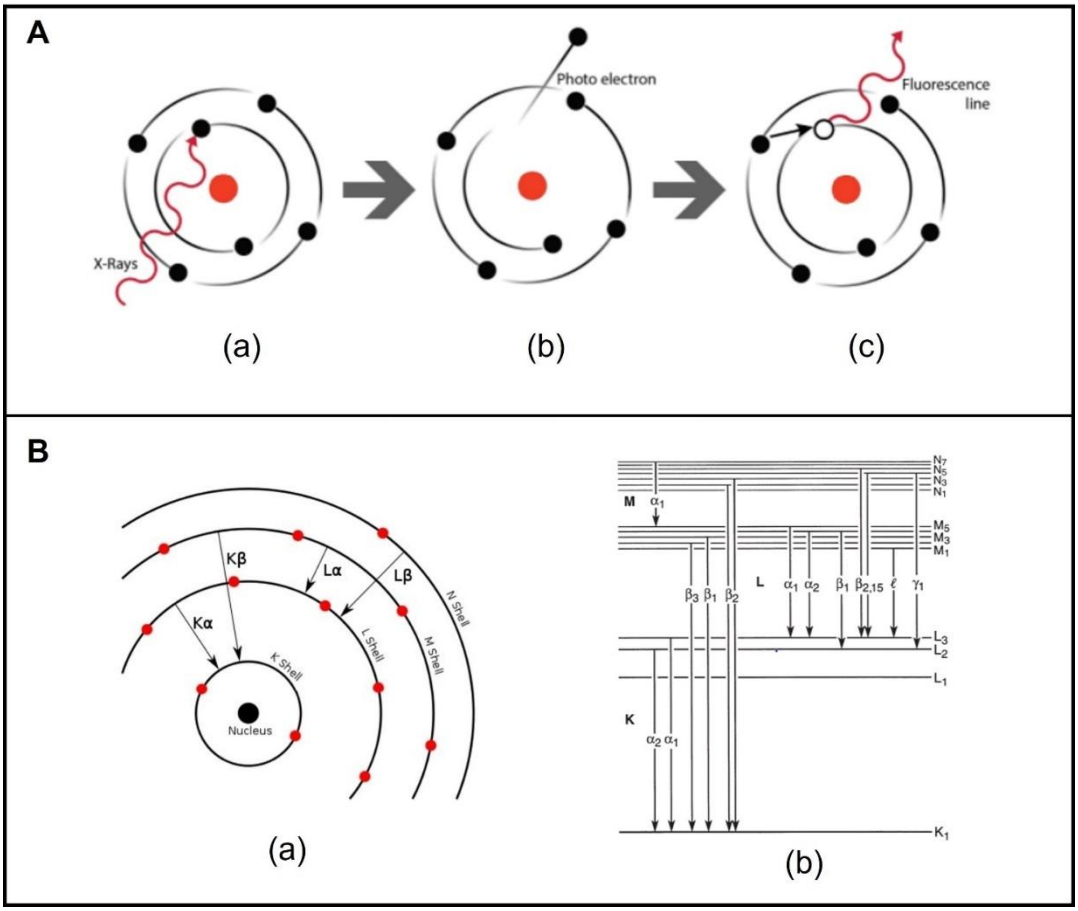

Figure 7 A) Bohr atom model - a positively charged nucleus surrounded by electrons that move within defined areas (called "shell" or "orbitals") - which illustrate the basic principle of X-ray fluorescence. (a) and (b) Excitation with X-ray leads to the ejection of an inner orbital electron from the atom. (c) The generated vacancy is filled by a higher-shell electron, during this process a photon, whose energy is equal to the difference in binding energies of the two shells involved in the transition, is emitted. **B**) X-ray emission lines. (a) Bohr atomic model, showing electron transitions in K and L emission lines that may follow electron vacancies. (b) X-ray emission lines described according to the "Siegbahn notation" [161].

Image sources: top image available from https://www.diamond.ac.uk/industry/Techniques-Available/Spectroscopy/X-ray-Fluorescence-XRF/How-XRF-works.html

Bottom left available from "Characteristic Radiation" by English Wikipedia user HenrikMidtiby. Licensed under CC BY-SA 3.0 via Wikimedia Commons-
https://commons.wikimedia.org/wiki/File:CharacteristicRadiation.svg#/media/File:CharacteristicRadiation.svg

Bottom right: Thompson AC, Kirz J, Attwood DT, Gullikson EM, et al. X-Ray Data Booklet. Third edition, September 2009. Thompson AC, editor. Lawrence Berkeley National Laboratory - University of California; available from: http://cxro.lbl.gov//PDF/X-Ray-Data-Booklet.pdf.

Each secondary X-ray photon (sometimes called characteristic radiation) emitted by the sample has a specific energy, characteristic of the atom it originated from. Thus, it is possible to establish the elemental composition of the sample at the point where the X-ray beam hits the sample, by measuring the energy of the secondary photons. XRFM provides the spatial distribution of different elements simultaneously and has been used to map trace elements in cells. Indeed, in μXRF mapping it is used a focussed spot to illuminate only a small section of the sample and to determine the composition at that point. Moving the sample in a grid pattern allows to generate a spectrum for each pixel of a 2D sample image. The spectra will then form the elemental map [162,163]. By use of calibrated standards, it is possible to make synchrotron XRF a quantitative technique.

1.11.3 X-ray Absorption Spectroscopy

The spectroscopy XAS (X-ray Absorption Spectroscopy) studies the absorption coefficient of a substance in function of the incident radiation energy in the X-ray region, from an energy that is just lower that the photoelectric absorption threshold tills to 1000 eV after the threshold. It allows studying the structure of atoms in molecules and materials. The energies involved in the XAS spectra range from a few hundred eV (soft X-rays) to several tens of thousands of eV (hard X-rays), usually used for with biological samples. Since it is necessary to continuously vary the energy of the radiation over a wide range, and since the useful signal is typically thousands of total signals, XAS experiments require an intense and polychromatic source. This is the reason it needs the use of synchrotron radiation.

The XAS spectrum is frequently divided into three distinct regions (**Fig. 8**) and different information can be obtained depending on the energy range considered [164]:

i) **Pre-edge region**: the energy range is limited to some eV before the absorption threshold. There is the presence of weak discontinuities due to the transitions of the core electron to other bound states.

ii) **XANES (X Ray Absorption Near Edge Structure)**: the part of the spectrum where the local electronic structure is characterized by studying the absorption cross section within 50-100 eV of an edge. The XANES study, combined with the pre-edge region, provides information about the local geometry of the absorbing metal and the oxidation state.

iii) **EXAFS (Extended X Ray Absorption Spectroscopy Fine Structure)**: the region of the spectrum that is between 100 eV and 1000 eV beyond the absorption threshold. From the EXAFS analysis, it is possible to determine the chemical state of the sample in the immediate vicinity of the absorptive atom (about ten Angstroms), that is provides information about metal site ligation.

The main advantages of the XAS method are its subatomic (angstrom) resolution, the ability to analyze almost any type of samples including amorphous (non-crystalline) materials, the possibility to analyze such materials in situ requiring minor or no sample preparation. The main limitations of XAS are its sensitivity in the mM (or mg g^{-1}) range, the difficulty to deconvolute the bulk data when the sample is composed of a mixture of structures of the absorber element, and the limited chemical selectivity of ligands to within one row of the periodic table [165,166].

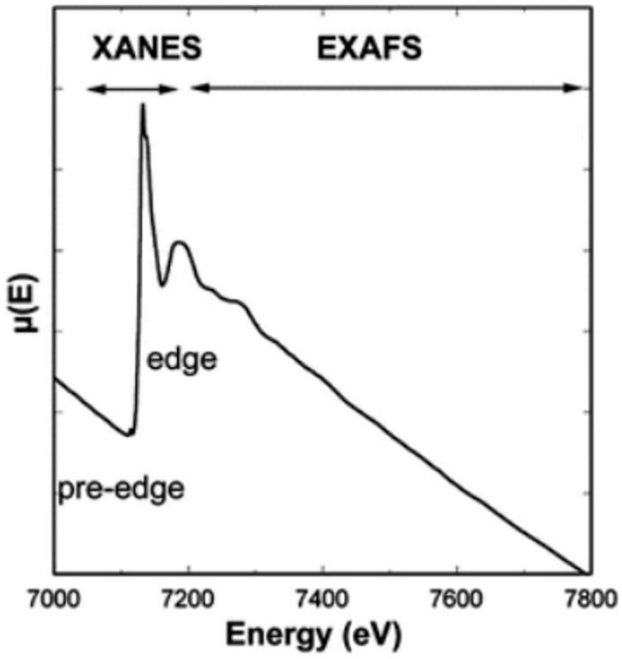

Figure 8 Variation of the linear absorption coefficient μ(E) as a function of the incident X-ray energy. *Image modified from Ortega et al, 2012 "* [164].

1.11.3.1 X-Ray Absorption Near Edge Structure

As mentioned above, XANES spectroscopy using synchrotron radiation is a well-established technique providing information on the electronic, structural, and magnetic properties of materials. A photon is absorbed, and an electron is excited from a central state to an empty state. To excite an electron in a given central level, the energy of the photon must be equal to or greater than the binding energy of this central level. The energy of an absorption edge corresponds to the energy of the central level, which is characteristic for each element, making XANES an element-selective technique. The region of the XANES spectrum is sensitive to a large amount of electronic structure information, which can be analyzed in three sections: i) before the boundary, the intensity of the pre-boundary features is strongly influenced by the coordination geometry of the central atom; ii) at the boundary, the formal oxidation state can be qualitatively assigned since the energy of the boundary position is not an invariant quantity for a given element, but shifts in accordance with the electronic density; iii)

beyond the boundary, the coordination shells are interrogated and the emitted photoelectron scatters onto neighbouring atoms [167].

Its element specificity and the possibility to obtain detailed information about local electronic structure of the element studied represent the main assets of XANES spectroscopy. XANES experiments can be performed with X-ray microscopes. Several transmission X-ray microscopes (TXM) or scanning transmission X-ray microscopes (STXM) exist for the soft X-ray range and the hard X-ray range. Typical resolutions that can be obtained are of the order of 20 nm [168,169].

1.11.4 Soft X-ray microscopy and X-ray cryotomography

Soft X-rays are a versatile probe for studying biological samples thanks to their specific interaction with matter in the so-called energy range of the water window, enabling high resolution imaging of intact and thick hydrated samples. The basic idea is to use the large absorption difference between carbon (e.g., proteins and lipids) and oxygen (e.g., water) in the "*water window"* (E≈285-535eV; λ ≈2.3–4.3 nm). This is due to (i) a high intrinsic depth of penetration into water and (ii) a high natural contrast between water and carbon-based cellular ultrastructure [31,170].

Single cells can be viewed through water layers up to ~ 10 μm thick, but the photon exposure required for imaging at 30 nm resolution leads to cells receiving a radiation dose of 106-108 Gray (108-1010 rad), excluding repeat imaging of live specimens. In recent years, 3D soft X-ray microscopy of cryo-fixed cells ("X-ray cryotomography") has emerged and is now providing unique results on a wide range of biologically relevant topics. Cryogenic sample preparation is essential for mitigating dose damage and is particularly interesting for its ability to study cells without modifications resulting from chemical fixation. [171].

Cryo-SXT consists of recording 2D soft X-ray transmission projections on a CCD (Charge Coupled Device) detector that changes the orientation of the sample with respect to the incident photons. X-ray cryotomography allows the classification of

different intracellular structures (e.g., lipid droplets, mitochondria, nuclei, vacuoles) providing 3D images of intact hydrated cells in their near-native state. This is possible thanks to the quantitative determination of the local absorption coefficient by the Beer-Lambert law, in analogy to macroscopic X-ray imaging of computed tomography (CT) [172,173].

These results were all obtained at the (few) soft X-ray microscopes which require a high photon flux, and which are currently available at the synchrotron radiation facilities in ALBA (Spain), HZB-Bessy II (Germany), Diamond (UK) or ALS (US). [171].

1.11.5 Micro-computed tomography (μCT)

X-ray computed tomography (XCT) is a powerful non-destructive technique that uses the penetrating power of X-rays to reconstruct 3D images of the internal structure of objects with a high spatial resolution, from 1 mm down to a few tens of nanometres. The technique consists of collecting radiographs of the sample (typically over 1000) from different angles (typically 360 ° or 180 °), which are then used to calculate the internal 3D structure of the object.

There are two main types of systems available: laboratory systems using X-ray tubes and synchrotron-based experimental stations.[174].

Synchrotron radiation micro computerized tomography (SR-μCT) has significant advantages: high flux of photons over a wide range of X-ray energies, high brightness, small angular divergence of the beam, high level of polarization and coherence, low emittance, and possibility of monochromatizating [175].

SR-μCT requires an experimental setup which consists of a high-precision sampling phase, with a sample holder, a scintillator, and subsequent light optics with a charge-coupled device (CCD) camera (**Fig. 9**). To obtain tomographic images, with a true micrometric resolution, a series of experimental conditions must be taken into consideration: the mechanical stability of the movement of the sample (translation and

rotation), the quality of the scintillator material and the number of angular projections recorded. The Radon transform is the mathematical approach commonly used to obtain the three-dimensional reconstruction of projection images [176].

The computational reconstruction of data is performed, producing a greyscale virtual 3D volume. The virtual slices can be extracted in any orientation and depth for viewing. Through image analysis processing tools, it is possible to obtain quantitative information from the investigated samples. Geometrical or morphological features inside the sample volume can be analysed and useful specific parameters can be extracted.

Since the sample is not damaged during the imaging process, this technique is routinely used in different scientific fields. In recent years, several papers have highlighted the potential of phase contrast SR-μCT as a promising technique for revealing the complexity of 3D bone features [177]. In the medical and bioengineering fields, the SR-μCT has been used to evaluate bone stiffness and the resistance of trabeculae and cortical tissue [178].

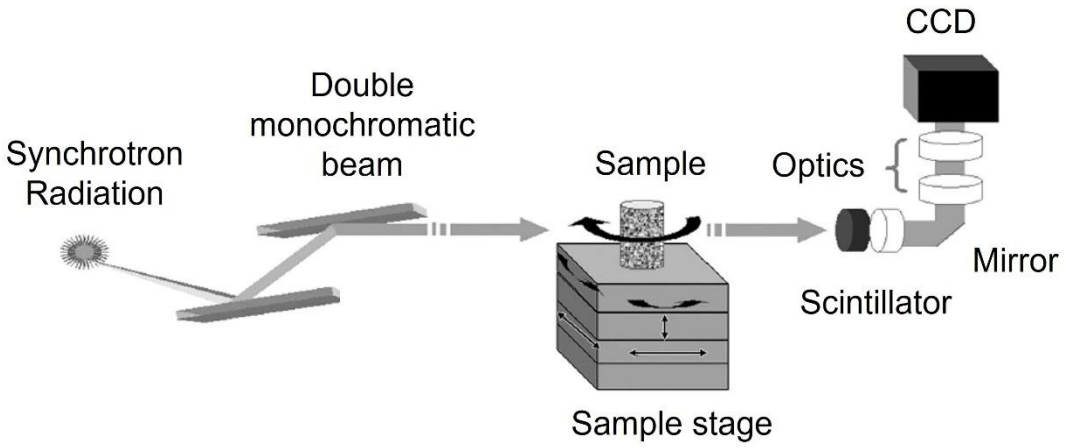

Figure 9 Schematic synchrotron radiation μCT experimental setup.

2. AIM of the project

The aim of this PhD thesis project was to investigate the early stages of bone biomineralization by assessing the formation of the first mineral core deposits and their evolution to hydroxyapatite in an osteosarcoma cell line as an osteoblast-like model.

To achieve this goal, 2D and 3D *in vitro* cultures of SaOS-2 cells were induced to differentiate by an osteogenic cocktail of dihydroxy vitamin D3, ascorbic acid and β-glycerophosphate. Successful osteogenic differentiation and development of intracellular and extracellular Ca mineral deposits were assessed at 3 different times after osteogenic induction.

The key point of this project was the use of multimodal and multiscale approaches that allowed us to study the phenomenon of differentiation and biomineralization from different angles. Firstly, the conventional laboratory methods such as gene expression analysis, histochemical stainings, enzyme activity assays and mitochondrial activity to primarily evaluate the efficacy of osteogenic treatment and the resulting metabolic changes were used.

The versatility of X-ray techniques generated by high-brilliance synchrotron light allowed the investigation at high spatial resolution of intracellular morphology and the actual localization and evolution of mineral nucleation during osteogenic engagement.

Moreover, the study of osteogenic differentiation performed on a tumor line is part of a broader and more ambitious context. A deeper understanding of the changes in mineral nanostructures in bone tumor cells could help to understand the mechanisms underlying the defective differentiation process occurring in osteosarcoma. Indeed, several studies suggested that the development of osteosarcoma may be associated with defects in osteogenic differentiation.

In light of this, most research efforts have focused on investigating alternative treatments that may overcome these defects while allowing for terminal differentiation and subsequent tumor inhibition.

Understanding the relationship between defects in osteogenic differentiation and tumorigenesis holds enormous potential for osteosarcoma treatment. The application of differentiation as a therapeutic approach may be a new desirable strategy for the treatment of osteosarcoma.

3. Materials and methods

3.1 SaOS-2 cell culture and Osteogenic Induction

Human osteosarcoma cell line SaOS-2 cells were purchased from American Type Culture Collection (ATCC, Manassas, VA, USA). For both 2D and 3D cell cultures, the cells were grown in RPMI 1640, supplemented with 10% heat inactivated FBS, 2 mM Glutamine, 1000 units/mL penicillin, and 1 mg/mL streptomycin, at 37 °C in a 5% CO_2/95% air humidified atmosphere.

To induce osteoblastic commitment, the 2D and 3D cells culture were treated with an osteogenic differentiation cocktail, after 24 hours from the seeding and then each 48 hours. The osteogenic cocktail contained 20 nM 1,25-Dihydroxyvitamin D3 (Sigma-Aldrich, Milan, Italy), 50 µM L-Ascorbic acid 2-phosphate (Sigma-Aldrich, Milan, Italy) and 10 mM β-Glycerol phosphate (Sigma-Aldrich, Milano, Italy). We selected 3 time points (3 or 4-7-10 days from cell seeding) for analyzing samples and evaluating the effect of osteogenic induction.

3.2 Experimental section on 2D cell cultures

3.2.1 Von Kossa and Alizarin Red staining

Von Kossa (Sigma-Aldrich, Milan, Italy) and Alizarin red (Sigma-Aldrich, Milan, Italy) stainings were used for the identification of mineralized deposits in the samples. SaOS-2 cells were seeded at $1\times10^4/cm^2$, grown in RPMI and treated with osteogenic cocktail as reported in section 1. For von Kossa staining the cells were washed with 1 mL of PBS for 3 times and fixed with EtOH 70% for 1 hour at RT. The fixed cells were washed 3 times with DDW and then 1 mL of 5% silver nitrate solution was added and left for 30 minutes under UV light. After 3 washes with DDW, it was added 1 mL of 5% sodium thiosulfate solution and left at RT for 5 minutes. Finally, the samples were washed three times with DDW and observed under light inverted microscope.

For Alizarin red staining the cells were washed with 1 mL of PBS for three times and fixed with cold EtOH 70% for 1h at RT. After 3 washed with DDW, 1 mL of 2% alizarin red solution was added and left for 30 minutes. The excess dye was removed, cells were washed twice with DDW and finally, the analysis under a microscope was performed.

3.2.2 Alkaline phosphatase activity (ALPL) assay

For evaluation of ALPL activity SaOS-2 cells were seeded at 2×10^4 /cm^2, grown in RPMI and treated with osteogenic cocktail as reported in paragraph 3.1. After 7 days of treatment the cells were harvested, washed twice in ice-cold PBS, and centrifuged at 3000 rpm for 5 minutes. For the treated samples we used a cell scraper to detach cells and collect them into ice-cold PBS before pelleting via centrifugation. The pellets were lysed in ice by 1 mL solution of 40 mmol/L HEPES, 110 mmol/L NaCl, 0.25% deoxycholate and 1 mg/mL aprotinin, (pH 7.4), stored at -20°C overnight and then centrifuged at 15000 rpm for 30 minutes. The supernatant containing proteins was tested for the ALPL spectrophotometric assay by using p-nitrophenyl phosphate (Sigma-Aldrich, Milano, Italy) as a substrate. ALPL activity was normalized for the protein content, measured by the Bio-Rad protein assay method. One unit of ALPL activity is defined as the amount of protein capable of transforming 1 mmol of substrate in 1 min at 25 °C [179]. Statistical analysis was performed by GraphPad Prism 8 software using a t-test and differences were deemed significant for $*p < 0.05$.

3.2.3 Gene expression analysis

Total RNA from cells collected after 7 days of osteogenic induction and extracted using the NucleoSpin®RNA (Macherey Nagel, Düren, Germany) following the manufacturer's instructions. The level of expression of the osteogenic markers runt-related transcription factor 2 (*RUNX2*), collagen type I (*COL1A1*), osteocalcin (*BGLAP*), osteopontin (*SPP1*) and osteonectin (*SPARC*) was analyzed by quantitative

real-time PCR (qPCR), as previously reported [180]. Data analysis was performed using the CFX Manager™ Software (Bio-Rad), creating a gene study that uses an intern calibrator to normalize the variability between the experiments. Data are reported as mean value ± SEM of at least three independent biological replicates. Statistical analysis was performed using GraphPad Prism 6 software using a two-way ANOVA followed by a Sidak's multiple comparison test. P values less than 0.05 were accepted as significant.

3.2.4 Electron transmission microscopy (TEM)

For ultrastructural evaluation, SaOS-2 cells was seeded in 6-well plates at 1×10^4 cells/cm^2 and were treated with vehicle or osteogenic differentiation cocktail as previously reported in paragraph 3.1.

After 4,7 and 10 days from osteogenic induction, the samples were fixed with glutaraldehyde (2.5%) in cacodylate buffer (0.1M pH 7.4) for 10 minutes and then detached by cell scraper. The cells were harvested, centrifuged at 3000 rpm for 20 minutes and fixed for 50 minutes at RT in the same solution. Post fixation, the pellets were washed twice in cacodylate buffer 0.1M pH 7.6.

After post-fixation with 1% osmium tetroxide (OsO4) in sodium cacodylate buffer 0.1M for 1 h, the pellets were dehydrated in an ethanol series, infiltrated with propylene oxide, and embedded in Epon resin. Ultrathin sections (80 nm thick) were stained with uranyl acetate and lead citrate (15 min each) and were observed with a JEOL JEM-1011 transmission electron microscope, operated at 100 kV. At least 100 cells per sample were observed.

3.2.5 Cryo-X-Ray Absorption Near-Edge Spectroscopy (cryo-XANES) and Cryo-Soft-X-ray Tomography (cryo-STX)

Sample preparation: SaOS-2 cells were seeded onto gold QUANTIFOIL® R 2/2 holey carbon-film microscopy grids, placed in a Petri dish p60. The cells were plated at a concentration of 2×10^4 cell/cm^2 on the grids previously sterilized by UV light for 3 hours. After 4 and 10 days from the osteogenic induction, the attachment and spreading of the cells was carefully verified using visible light microscopy prior the freezing. Cell culture medium was removed, and the membranes were briefly washed in PBS. The cells were stained with Mito tracker green 200 nM (Sigma-Aldrich, Milano, Italy) and incubated for 10 minutes at 37 °C. Immediately prior to freezing 1.5 µL of 100 nm gold fiducial aliquot (Chemical reference: gold nanoparticles 100 nm, EMGC100, BBI Group, Cardiff, UK) was added to the grids, necessary as external marker for the tomographic reconstruction. The grids were frozen hydrated by a rapid plunge freezing in a liquid ethane pool cooled with liquid nitrogen with a GP-Leica Microsystems Excess. Water is removed before plunge freezing via blotting. Quality of the sample's preparation was checked in cryo-conditions prior the loading in the microscope chamber. After plunge freezing, a cryogenic workflow is maintained until and during the measurements. Calcite reference sample were prepared by finely crushing calcite powders (Sigma–Aldrich, Milan,Italy) in a mortar, and the obtained dust was laid down on a Quantifoil Au TEM grid. The same procedure has been used for the preparation of HA and $Ca_3(PO_4)_2$ reference samples (provided Bio Eco Active S.R.L, Bologna, Italy).

Cryo-SXT and cryo-XANES images were recorded at the MISTRAL beamline of the ALBA Synchrotron. Scanning the X-ray energy through the Ca $L_{3,2}$ edge, cryo-XANES can be used to determine the Ca bulk chemical state. L-edge spectroscopy measures X-ray absorption caused by the excitation of a metal 2*p* electron to unfilled *d* orbitals, which creates a characteristic absorption peak called the L-edge. It is, in general, more

sensitive to the electronic, structural, and the spin state changes of the element compared to the K-edge spectroscopy (when the photoelectron originates from a 1*s* core level) [181].

2D Ca $L_{3,2}$ edge XANES images were collected on representative areas (12 s exposure time) using an effective pixel size of 13 nm and with a variable energy step (0.5 eV of pre-edge and post-edge, 0.1 elsewhere). The necessary total acquisition time was about 1.5 h per energy scan, including the flat field acquisition at each energy step. The transmitted intensity at each energy value is normalized to unity dividing by the corresponding flat field image. Then, all the transmission images are aligned with respect to the first image, applying the x–y shifts, which maximize the cross-correlation between the same selected ROI in the two images. Finally, the absorbance for each pixel can be calculated from the measured transmission as:

$$A=\mu t=-ln(I/I0)$$

and can be related as a function of the energy to the linear absorption coefficient using the Beer–Lambert law:

$$T(x,y)=I(x,y)/I0(x,y)=e(-\int \mu l(x,y,E0)dt)=e(-\int \mu m(x,y,E0)\rho dtm)$$

(2)

where t is the thickness, μl is the linear absorption coefficient of the material, and μm is the mass absorption coefficient. Spectra were extracted only from pixels that satisfy the following signal to noise criteria:

$$\Delta \mu lt=[\mu l(349.2eV)-\mu l(342eV)]t>2N$$

(3)

with μl as the linear absorption coefficient, t as the thickness, and N as the noise defined as the absorbance standard deviation in the pre-edge energy region (341–343.5 eV). The pixel selection operation was performed using a homemade function created in Matlab.

Cryo-SXT was carried out at 352.9 eV to optimize the contrast between the calcium- and carbon-rich objects and the surrounding water-rich cytoplasmic solution without

staining, sectioning, or using enhancing agents. For each cell, a tilt series was acquired using an angular step of 1° on a 110° angular range. The effective pixel size in the images was 13 nm at 352.9 eV. Each transmission projection image of the tilt series was normalized using flat-field images of 1 s acquisition time. The tilt series were manually aligned using eTomo in the IMOD tomography software suite [182]. Au fiducials of 100 nm from BBI solution were used for projection alignment purposes. The transmission tilt series were finally reconstructed with TOMO3D, using the SIRT iterative algorithm with 30 iterations and then segmented by Amira (Thermo Fisher Scientific, Waltham, MA, USA).

3.2.6 Mito-stress Seahorse assays

Cells were seeded at 2.5×10^3 cells/cm^2 into Seahorse XF96 V3 PS Cell Culture Microplates (Agilent, Santa Clara, California, United States) for 4 days prior to experiments. After 24 and 72 h from the seeding, cells were treated with vehicle or osteogenic differentiation cocktail as previously reported. Complete seahorse medium was prepared from Agilent Seahorse XF Base Medium (Agilent) to contain 10 mM glucose, 2 mM glutamine and 1 mM pyruvate, with pH 7.4. The cells were incubated in 180 µL complete seahorse medium at 37°C for 1 hour before measurements in Seahorse XFe96 Analyzer. The following working concentrations of compounds were used: 1 µM Oligomycin, 1 µM FCCP, 1 µM Rotenone, and 1 µM Antimycin A. The oxygen consumption rate (OCR) was normalized to the protein content. Statistical analysis was performed by GraphPad Prism 8 software, using a T-test. The differences were deemed significant for $*p < 0.05$. All data are presented as mean± SEM n = 5 technical replicates from five biological samples for each group.

3.3 Experimental section on 3D cell cultures

3.3.1 3D Collagen-Cell Cultures

Rat Tail Collagen solution 3.8 mg/mL pH 3-4 (RatCol®; CellSystems GmbH, Troisdorf, Germany) was mixed with formulated neutralization solution into a sterile mixing tube in a ratio 9:1 for a total of 10 parts for the formation of a collagen gel. 2×10^5 osteosarcoma SaOS-2 cells suspended in 55 µL of complete medium were added to 245 µL of collagen solution. The final Rat Tail Collagen mixture was divided up into 96-well plates, in a final volume of 300 µL for each scaffold. After gelification, the cell-laden scaffolds were incubated in humidified atmosphere at 37°C with 5% CO_2 in 1 mL of basal culture medium. The cells were treated with vehicle or osteogenic differentiation cocktail after 24h and every 48h. At indicated time points, the scaffolds were dissolved with a 0.25% collagenase solution and then processed for following analysis. To obtain cell growth curve, viable cells from triplicate wells were counted at 1, 3, 7, and 14 days. To determine cell cycle distribution, SaOS-2 cells were washed in PBS, and centrifuged. The pellet was resuspended in 0.01% Nonidet P-40, 10 µg/mL RNase, 0.1% sodium citrate, and 50 µg/mL propidium iodide for 30 min at 37 °C in the dark. Propidium iodide fluorescence was analyzed by using a flow cytometer Bryte HS (BioRad) and cell cycle analysis was performed using the Modfit 5.0 software (Verity Software House, Topsham, ME, USA).

3.3.2 Gene Expression Analysis

Total RNA from cells collected at the indicated time points from up to three scaffolds cultured in control condition or under osteogenic induction. At indicated time points, the scaffolds were dissolved with a 0.25% collagenase solution and then washed in PBS twice and then the pellets were extracted using the NucleoSpin®RNA (Macherey Nagel, Düren, Germany) following the manufacturer's instructions. The level of expression of the osteogenic markers *RUNX2*, *COL1A1*, *BGLAP* and *SPP1* was

analyzed by quantitative real-time PCR (qPCR), as previously reported in section *3.2.3* for 2D cell culture**.** Data are reported as mean value ±SEM of three independent biological replicates. Statistical analysis was performed using GraphPad Prism 6 software using a two-way ANOVA followed by a Sidak's multiple comparison test. P values less than 0.05 were accepted as significant.

3.3.3 Total Intracellular Mg Quantification

After the scaffold dissolution with collagenase 0.25%, SaOS-2 cells were washed twice with PBS without Ca^{2+} and Mg^{2+}, counted and resuspended at 1×10^6 cells/mL. Samples were lysed by sonifier, and 100 µL of the sample were added to 100 µL of PBS without Ca^{2+} and Mg^{2+}, 22 µL of the magnesium probe DCHQ5 1.37 µM in DMSO and 1778 µL of MOPS 20 mM/Methanol 50%. Fluorescence spectra were collected with λ_{ex} 363 nm. Mg concentration was assessed comparing the fluorescence intensity at λ_{em} 510 nm of the samples with a calibration curve prepared with $MgSO_4$ [183].

3.3.4 Histochemical Analysis

Collagen scaffolds were fixed with paraformaldehyde (4%) for 1 h at RT, dehydrated through a graded alcohol series up to 100% and embedded in paraffin with standard methods. Sections of 10 µm thickness were cut orthogonally to the scaffold axis, deparaffinized with xylene, rehydrated to 70% alcohol, and stained according to standard hematoxylin/eosin staining protocol with Mayer's hematoxylin and 1% eosin solution (Bio-Optica, Milan, Italy) and mounted in permanent medium. For Alizarin red S staining, the deparaffinized rehydrated sections were rinsed rapidly in distilled water and stained with 2% Alizarin red S solution for 5 minutes. Excess dye was shaken off and stained sections were fixed with acetone (20 dips), acetone-xylene (20 dips), cleared with xylene and mounted in permanent medium [184]. Quantitative analysis of ECM mineralization was performed on images acquired from cellularized collagen scaffold slices. Control and treated images acquired with optical microscope were

processed by using ImageJ software (National Institute of Health, USA), in order to determine the size of the red (Alizarin red staining) area. This was calculated using the maximum entropy threshold-based image segmentation method [185]. Four separate fields out of each single microphotograph were analysed.

3.3.5 X-ray Fluorescence Microscopy Analysis

Collagen scaffolds treated for 7 days was fixed with paraformaldehyde (4%) for 1 h at RT and embedded in paraffin with standard methods. Histological sections (thickness, 10 µm) were cut orthogonally to the scaffold axis by microtome. Ultralene foil (Spex Sample Prep 3525 Ultralene® Window Film 0.16 mil (4 µm) Thick, 2 7/8 in Wide; 300 ft; Cole-Parmer Srl, Milano) was used as support material.

The XRFM and STXM measurements were carried out at the Twinmic beamline of the Elettra Synchrotron light source (Basovizza, Trieste, Italy). A Fresnel zone plate focused the incoming beam (2150 eV), monochromatized by a plane grating monochromator, to a circular spot of about 1.25 /m in diameter. The sample was transversely scanned in the zone plate focus, in steps of 1.2 µm. At each step the fluorescence radiation intensity (dwell time 8–10 s) was measured by eight Si-drift detectors (active area 30 mm^2) (chips from PnDetector, Munich, Germany and electronics from XGLab, Milano, Italy) [186] concentrically mounted at a 20° grazing angle with respect to the specimen plane, at a detector-to-specimen distance of 28 mm. Simultaneously, the transmitted intensity was measured by a fast-readout electron-multiplying low-noise charge-coupled device (CCD) detector (Andor Technology, Belfast, Ireland) through an X-ray to visible light converting system [187]. Zone plate, sample, and detectors were accommodated in vacuum, thus avoiding any absorption and scattering by air. The X-ray fluorescence spectra were analysed by PyMCA software [188] which provides the total counts for the fluorescence K-lines of Mg and P.

3.3.6 Laboratory-Based X-ray Computed Microtomography Analysis

For Laboratory-based X-ray computed microtomography (μCT) one control and one treated sample for 7 days were analyzed. The samples were fixed with paraformaldehyde (4%) for 1 h at room temperature and embedded in paraffin with standard methods.

The μCT measurements were carried out at the TomoLab station [189] at Elettra. This instrument, based on a microfocus X-ray source (minimum focal spot size of 5 μm), can operate at a Voltage ranging between 40 and 130 kV with a maximum power of 39 W. A 12-bit, water cooled, 4008 x 2672 pixels CCD camera was used as detector. The camera chip is coupled via a fiber optic bundle to a Gadox scintillator screen, and a de-magnifying optics allows to obtain an effective pixel size of 12.5 μm yielding a maximum field of view of 50 × 33 mm^2 at sample. Due to the focal spot size of the source and the specific design of the TomoLab station [190] it was possible to perform propagation-based phase-contrast X-ray μCT measurements. The experimental parameters used for the imaged samples are summarized in Supplementary Table S2. The tomographic reconstruction was performed by the commercial software COBRA (Exxim, USA) while the 3D visualization of the reconstructed and processed data was obtained by the commercial software VGStudio MAX 2.0 (Volume Graphics, Heidelberg, Germany).

3.3.7 Synchrotron-Based X-ray Computed Microtomography Analysis

One tomographic data set for a sample treated for 7 days has been acquired, after embedding in PFA 4% as reported above.

The measurements were conducted at the SYRMEP beamline of Elettra [191], which was operated at an electron energy of 2.0 GeV. The source of the synchrotron radiation is a bending magnet featuring a magnetic field of 1.2 T, which generates a white spectrum of synchrotron radiation with a critical energy of about 3.2 KeV. This white beam spectrum has been filtered by a 500 μm thick Be window and additional Si filter

of a thickness of 500 µm resulting in a bell-shaped curve centered around 24 keV. The images were recorded in phase-contrast (propagation-based) mode. The source-to-sample distance was around 22 m while the sample-to-detector (thus the propagation) distance was set to 150 mm. The detector was a sCMOS imager (Orca Flash from Hamamatsu) optically coupled to a 45 µm thick GGG:Eu (Gd3Ga5O12:Eu) scintillator utilizing a set of optical lenses with different magnifications. The sCMOS sensor comprises 2048 × 2048 pixels^2 (with a size of 6.5 × 6.5 µm^2) and features a dynamic range of 37,000:1. For the data set described here the highest optical magnification has been used, which translates into a field of view of 1.85 mm × 1.85 mm and a pixel size of 0.9 × 0.9 µm^2. A total of 1800 equiangular projections have been acquired over a total scan angle of 180 degrees using an exposure time of 100 ms per projection.

The tomographic reconstruction was performed utilizing an in-house software tool, the so-called SYRMEP Tomo Project (STP) software (https://github.com/ElettraSciComp/STP-Gui) [192]. Prior to image reconstruction based on a filtered back projection algorithm, each projection was independently pre-processed with a phase-retrieval algorithm based on the transport of intensity equation [193].

3.3.8 3D Cell-Laden CTL/agarose scaffolds

Hydrochloride form of lactose-modified chitosan, CTL (CAS Registry Number-2173421-37-7) was kindly provided by BiopoLife s.r.l. (Trieste, Italy) [194]. Briefly, 110 mg of polymer was solubilized in 8.5 mL of milliQ water; the pH was then adjusted to 7.4 by adding NaOH 5 M. Then 1 ml of PBS 10× and deionized water amounts were added to have a final volume of 10 mL. Finally, 110 mg of agarose (Sigma-Aldrich, Milan, Italy) was added under magnetic stirring for 1h. The final solution was autoclaved and flow to 38°C. SaOS-2 cells were encapsulated into gel composed of CTL 1% w/v and agarose 1%w/v in 1:10 ratio and mixed into a tube. The final concentration of the cells was 4×10^6/ml. The resulting suspension was dispensed into

48-well plates, in a final volume of 200 µL for each scaffold and left for 1 h at RT for gelation. The scaffolds were removed and placed in 24-well plate and incubated in humidified atmosphere at 37 °C with 5% CO_2 in 1.5 mL of basal culture medium. After 24 h, cells were treated with vehicle or osteogenic differentiation cocktail, replacing the media every 48 h as previously reported.

3.3.9 Alamar Blue cell viability assay on CTL/agarose scaffolds

Cell viability/cytotoxicity was estimated using the colorimetric indicator AlamarBlue® assay (Life Technologies, Carlsbad, California, United States). At established time point (1, 4, 7 and 10 days after seeding), the culture medium was replaced by 1 ml of RPMI and AlamarBlue® solution (in a 10:1 ratio) for each scaffold and incubated for 4 h at 37 °C. Next, the medium was collected, and the fluorescence was measured with a plate reader (EnSpire Multimode Plate Reader, Perkin-Elmer) by applying a λ_{ex} of 560 nm and λ_{em} of 590 nm. For each experiment two scaffolds were measured in triplicates and the percentage of AlamarBlue reduction was normalized to that of the basal medium by using the equation: F590 sample*100/F590 basal medium. The experiment was repeated three times.

3.3.10 Live/dead assay on CTL/agarose scaffolds

To visualize the cell viability and distribution, the cell-laden scaffolds were dissected using a sterile scalpel and stained using live/dead viability/cytotoxicity assay. Briefly, cell-gel samples were washed two times with PBS and then incubated with propidium iodide (5 µg/ml) and calcein AM (2µM), according to manufacturer instructions, for 45 min at 37 °C and 5% CO2. Each section was observed under confocal fluorescence microscope. 100 µm z stacks were taken with 4 µm between each slice. Images were acquired with a Nikon eclipse 90i fluorescence microscopy (Nikon Corporation, Tokyo, Japan). Three images were taken per scaffold, at 3 different time point. Live and dead cells were counted using FiJi. The percentage of live cells was calculated as *total dead cells / total cells · 100% = % dead cells*

3.3.11 Phalloidin/Hoechst staining on CTL/agarose scaffolds

Cell-laden scaffolds were fixed in 4 % formaldehyde in PBS at room temperature for 3 hours, washed with PBS and then incubated with phalloidin-conjugate working solution and Hoechst working solution (1:500) at room temperature for 30 minutes. Each scaffold was rinsed with PBS, 5 minutes per wash, mounted to preserve the fluorescence and observed under confocal fluorescence microscope.

3.3.12 Alizarin red staining on CTL/agarose scaffolds

To investigate calcium depositions in differentiated SaOS-2 cell line cultured in the CTL/agarose scaffolds, Alizarin red S staining was carried out after 4, 7 and 10 days. The scaffolds were rinsed with PBS, fixed (PFA 4%, 1 h), and stained for 30 min with 2% Alizarin Red S pH 4.2 (Sigma–Aldrich, Milano, Italy). The scaffolds were washed in water to remove the excess of dye. Quantification of ARS was achieved by dissolving the samples in 2 mL of 10% w/v Cetylpyridinium Chloride (Sigma Aldrich, Milano, Italy) prepared in 10 mM Na_2PO_4 (pH 7.0). After overnight ARS solutions in CPC before were transferred into 96 well plates and the absorbance at 562 nm was measured by a microplate reader (EnSpire Multimode Plate Reader, Perkin-Elmer). The average value of negative controls (scaffolds without cells) was subtracted from the values of the corresponding experimental groups. The experiment was repeated three times in triplicate.

4. Results and Discussion

4.1. Differentiating effects on 2D cell cultures

4.1.1 Analysis of mineralization by histochemical stainings

SaOS-2 cell line was cultured for 7 days with basal and osteogenic media. In order to assess mineralization of extracellular matrix, two different staining were performed: i) von Kossa staining, that highlights the presence of carbonate and phosphate calcium salts replacing calcium with silver and, ii) Alizarin red staining that binds all calcium ions. Representative pictures of control and treated samples (**Fig. 1 A and B**) showed that after 7 days of osteogenic stimuli, microscopically visible silver glow spots appeared in treated sample. Likewise, Alizarin red staining showed that in the cells exposed to the control medium, the Ca-depositions were smaller and less intensely stained respect to the treated sample, where the calcified nodules were bigger and more intensely marked (**Fig. 1 C and D**). These results evidenced the presence, by Von Kossa and Alizarin red stainings, of carbonate and phosphate calcium salts in the extracellular matrix of cells undergoing osteogenic treatment.

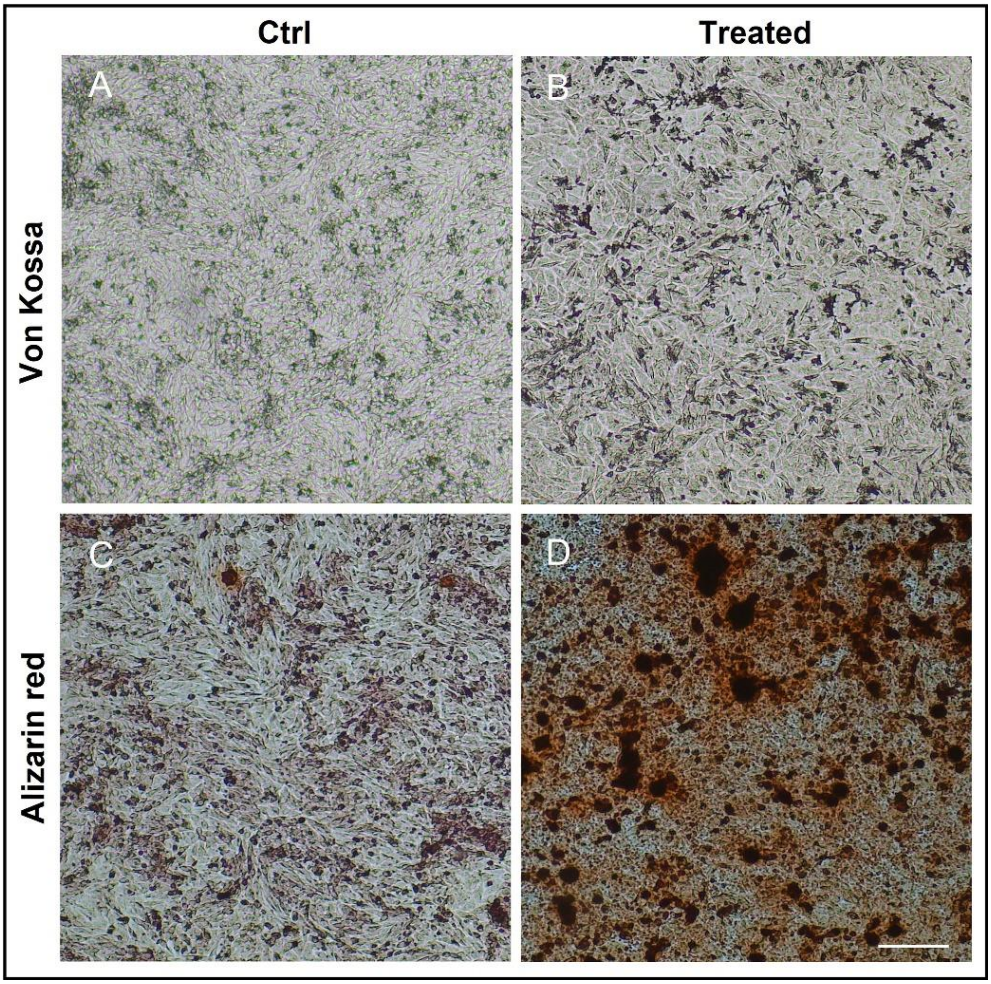

Figure 1 SaOS-2 cell culture after 7 days of osteogenic induction. A) and B) Von Kossa staining of and C) and D) Alizarin red staining of Ctrl and Treated sample. All pictures are obtained by inverted light microscope at 4× magnification. Scale bar is 200 μm.

4.1.2 Evaluation of osteogenic marker expression

Gene expression analysis of six osteogenic markers was evaluated by real-time qPCR in SaOS-2 cells at 7 days of treatment with osteogenic cocktail. The results obtained showed a relevant upregulation of all osteogenic markers in the treated sample, except for osteonectin (*SPARC1)* (**Fig. 2**). The early osteogenic commitment transcription factor (*RUNX2)* and alkaline phosphatase (*ALPL*) showed two-fold increase of mRNA expression levels in the treated sample respect to control. In addition, the other early osteogenic marker collagen type 1 (*COL1A1*) was much more upregulated, as well as

the late osteogenic markers osteocalcin (*BGLAP*) and osteopontin (*SPP1*) compared to their specific control counterparts. In detail, the upregulation of *BGLAP* and *SPP1* genes was 5-fold higher, for both. Meanwhile, after 7 days of treatment, the upregulation of the osteogenic marker *COL1A1* was scored, showing about a 9-fold increase in its mRNA expression level with respect to its control. SaOS-2 cells have been described as more differentiated osteoblasts respect to other osteosarcoma cell line, normally with an intrinsic low expression level of two initial-stage osteogenic marker *COL1A1* and *ALPL* [139].

Overall, our results show the overexpression of both early osteogenic genes (*RUNX2*, *COL1A1*, *ALPL*) and late osteogenic genes (*BGLAP*, *SPP1*) confirming a greater osteoblastic commitment following differentiating treatment, already after 7 days.

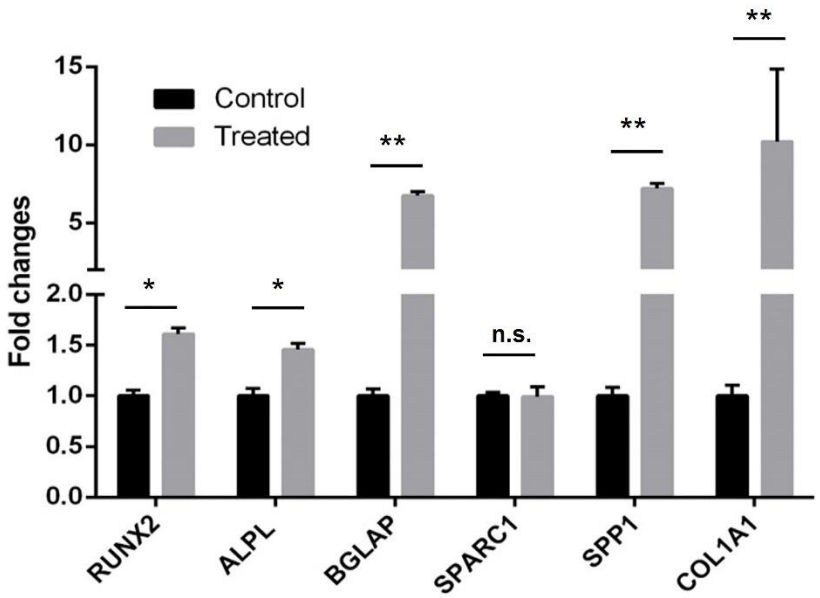

Figure 2 Gene expression analysis of SaOS-2 cells cultured for 7 days and treated with the osteogenic cocktail. qPCR analysis of osteogenic markers (*RUNX2, ALPL, SPARC, COL1A1*, *BGLAP*, and *SPP1*) was performed using GAPDH and HPRT1 as reference genes (2-ΔΔC*T* method). Fold changes from control untreated cells were calculated. Data of three biological replicates are reported as mean ± SEM. Two-way ANOVA followed by a Sidak's multiple comparison test was performed, * $p < 0.05$; ** $p < 0.01$.

4.1.3 Assessment of Alkaline phosphatase activity

Alkaline phosphatase enzyme plays a key role in bone mineralization, and it is well accepted that it represents an early marker of osteogenic differentiation since it is involved in bone formation. Its activity in SaOS-2 cells was examined to evaluate the osteo-inductive effect of cocktail after 7 days of treatment. Treated cells showed a significantly higher ALPL activity than the untreated samples, as indicated in **Fig. 3**. The osteogenic stimulation of SaOS-2 cells leads to a prompt increase in enzyme activity, although SaOS-2 is an osteoblast-like cell line with a high basal alkaline phosphatase activity [195]. Indeed, several studies suggest that in SaOS-2 cells ALPL activity can be considered an osteogenic marker and its increase correlates with differentiation toward an osteoblastic phenotype [196].

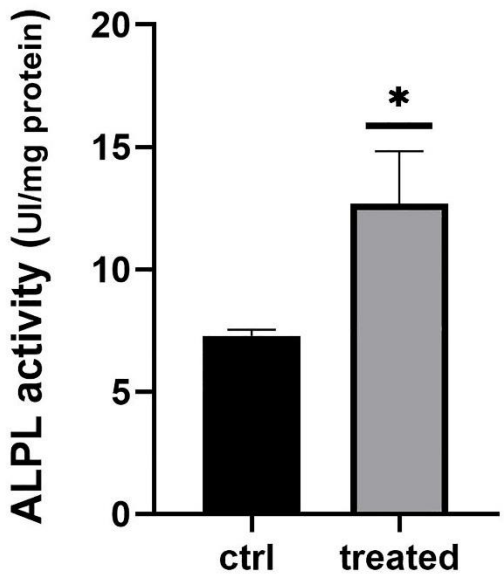

Figure 3 Alkaline phosphatase activity on SaOS-2 cells after 7 days of osteogenic induction. Data are reported as mean ± SEM of three biological replicates. Unpaired T-test was performed, *$p < 0.05$.

4.1.4 Ultrastructural characterization by TEM

TEM analysis showed that both control and treated samples had a cytoplasmic environment typical of a functioning cell, rich in mitochondria and with high vesicular trafficking. Great differences appeared in term of mineralization process, afterwards osteogenic treatment. Representative TEM images indicate that at 4 days of induction an increased intra-vesicular trafficking is noted in the treated sample respect to the control ones (**Fig. 4 A, B, C**). The effect of induction was well evident at 7 and 10 days of treatment. In particular, the cytoplasm of stimulated SaOS-2 cells at 7 days was rich in organelles not loaded with mineral material (**Fig. 4E**, *light green arrow*) or containing well compartmentalized mineral deposits (**Fig. 4E**, *red arrow*). In addition, a mineralization front was already appeared outside the cytoplasmic membrane (**Fig. 4F**, *blue arrow*). While, at 10 days the control sample appeared rich of organelles containing dense mineral material (**Fig. 4G**, *red arrow*), but it did not show the presence of extracellular matrix. At same time, in the treated sample there were more dilatated organelles, and the extracellular matrix became thicker and darker (**Fig. 4 H** and **I**, *blue arrow*). Therefore, there was a compaction of the mineral matrix probably due to the evolution of CaP (Calcium phosphates) in HA. The picture in the yellow box (**Fig. 4**) showed a representative HA crystal.

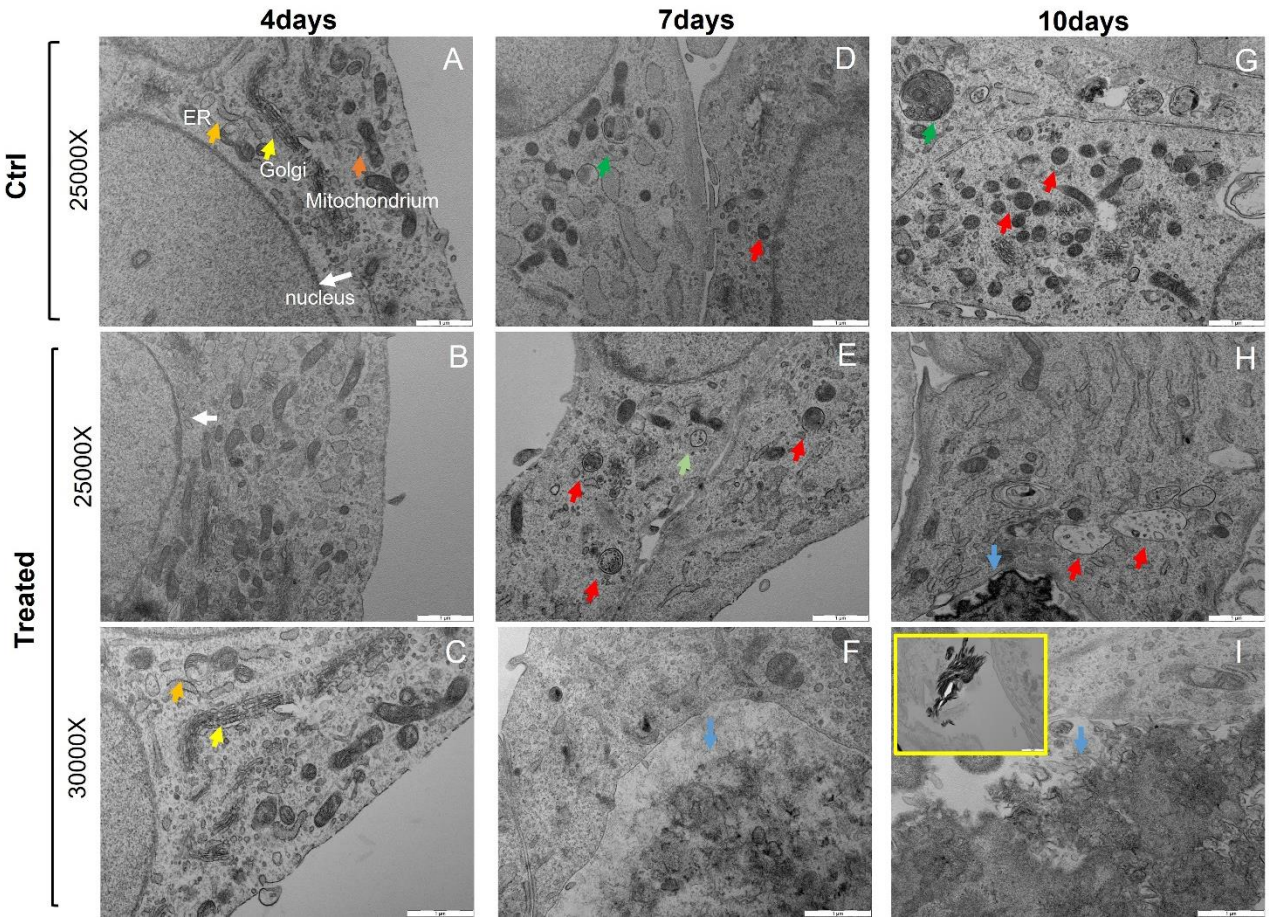

Figure 4 TEM images of SaOS-2 cells. The upper panel showed Ctrl sample (A, D, G) at 3 different time point. Magnification 25000×. The middle and lower panel showed Treated samples at 4,7,10 days of osteogenic treatment. B, E, H) Magnification 25000×; C, F, I) Magnification 30000×. Yellow box= HA crystal, magnification 25000×. Scale bar is 1µm. Arrow legend: White=nucleus, light yellow=Golgi apparatus, dark yellow=endoplasmic reticulum, orange=mitochondria, green=autophagic vacuole, red =MVBs with mineral deposits, light green= MVBs without Ca-deposits, light blue= extracellular mineral matrix. At least 100 cells per sample were observed.

TEM microscopy results revealed that the process of mineralization proceeds differently over time for ctrl and treated samples, also showing an evident implication of vesicles-like organelles in the matrix mineralization. Indeed, the dimensions and the localization of organelles rich of mineral deposits found in our samples, agree with the results reported by Iwayama et al. on a murine osteoblast cell line [197].

We hypothesized that the organelles with well compartmentalized depositions could be multi-vesicular bodies (MVBs) containing exosomes and Ca phosphate-rich matrix

vesicles (MVs) that must be driven out of the cytoplasmic environment, to release the extracellular mineral matrix. Exosomes and matrix vesicles are both categorized as homologous structures with similar sizes (100-300 nm), and they are both secreted during osteoblastic activity. They may share functions in cell-cell communication, providing a mechanism to transfer signaling molecules between cells within the growth plate and thereby regulating bone development and formation [198,199].

4.1.5 Characterization of intra and extra cellular Ca-depositions by Cryo-XANES and Cryo-SXT

Cryo-XANES spectro-microscopy at the Ca $L_{3,2}$-edges and cryo-SXT were performed in frozen-hydrated cells for localizing and characterizing crystalline phase of Ca-depositions. The two techniques were used respectively for 2D mapping of Ca chemical states and for analyzing Ca accumulation in intracellular and extracellular spot depositions.

The cryo-XANES microscopy performed at pre-edge and Ca $L_{3,2}$-edge on cytoplasmic cell region, showed the presence of small Ca-depositions in control sample at 4 days (**Fig. 5 A, B, C**). At the same time, the treated sample (**Fig. 5 D E, F**) showed the presence of bigger extracellular deposits. These Ca-depositions appeared quite structured and organized near or within organelles likewise, to multivesicular bodies (MVBs) containing exosomes or vesicles rich of Ca-minerals (**Fig. 5 E**, *yellow ring*), confirming their identification through the TEM analysis.

The cryo-XANES microscopy revealed that the Ca-depositions raised up in number and became more compact after 10 days of osteogenic induction (**Fig. 5 G, H, I**).

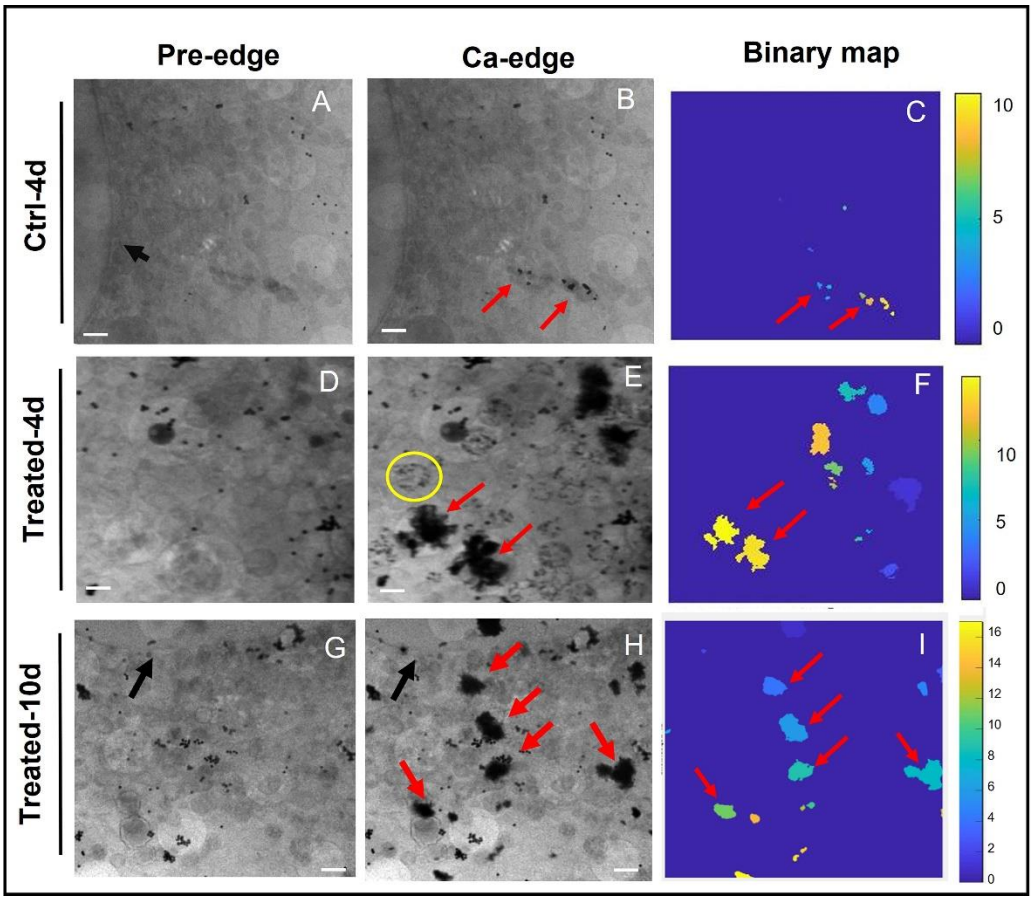

Figure 5. Cryo-XANES microscopy on Ctrl and Treated SaOS-2 cells after 4 and 10 days of osteogenic treatment. Average of absorbance projections of a cytoplasm cell region recorded at pre-Ca-edge energy region (≈ 342 eV) and at the Ca L_3 peak maxima (≈349 eV), respectively for Ctrl-4days (A, B), Treated-4days (D, E) and Treated-10days (G, H). The contrast between Ca and the other elements is maximized and showing the presence of calcium depositions. Scale bar=250 nm. Binary map of Ca-depositions for Ctrl-4days (C), Treated-4days (F) and Treated-10days (I) samples. Black arrow indicates the edge of cell nuclei, red arrows indicate the Ca-depositions at $L_{3,2}$ edge, yellow ring indicates the Ca-rich vesicles.

During time and after the osteogenic treatment we observed a change in the XANES spectral profile associated to the Calcium depositions. At 4 days of culture, the extravesicular Ca-depositions in control sample showed a XANES spectral profile ascribable the $CaCO_3$ (**Fig. 6A**), while those in the treated sample showed a profile spectrum more similar to $Ca_3(PO_4)_2$ (**Fig. 6C**). The reference standard spectra were reported respectively for $CaCO_3$ (**Fig. 6B**) and for $Ca_3(PO_4)_2$ (**Fig. 6D**).

After 10 days of osteogenic induction the crystalline structure of mineral depositions changed: some Ca-nodules showed a spectral profile similar to $Ca_3(PO_4)_2$, but most of them were more alike the HA spectrum, as shown in Fig. 6E and Fig. 6F.

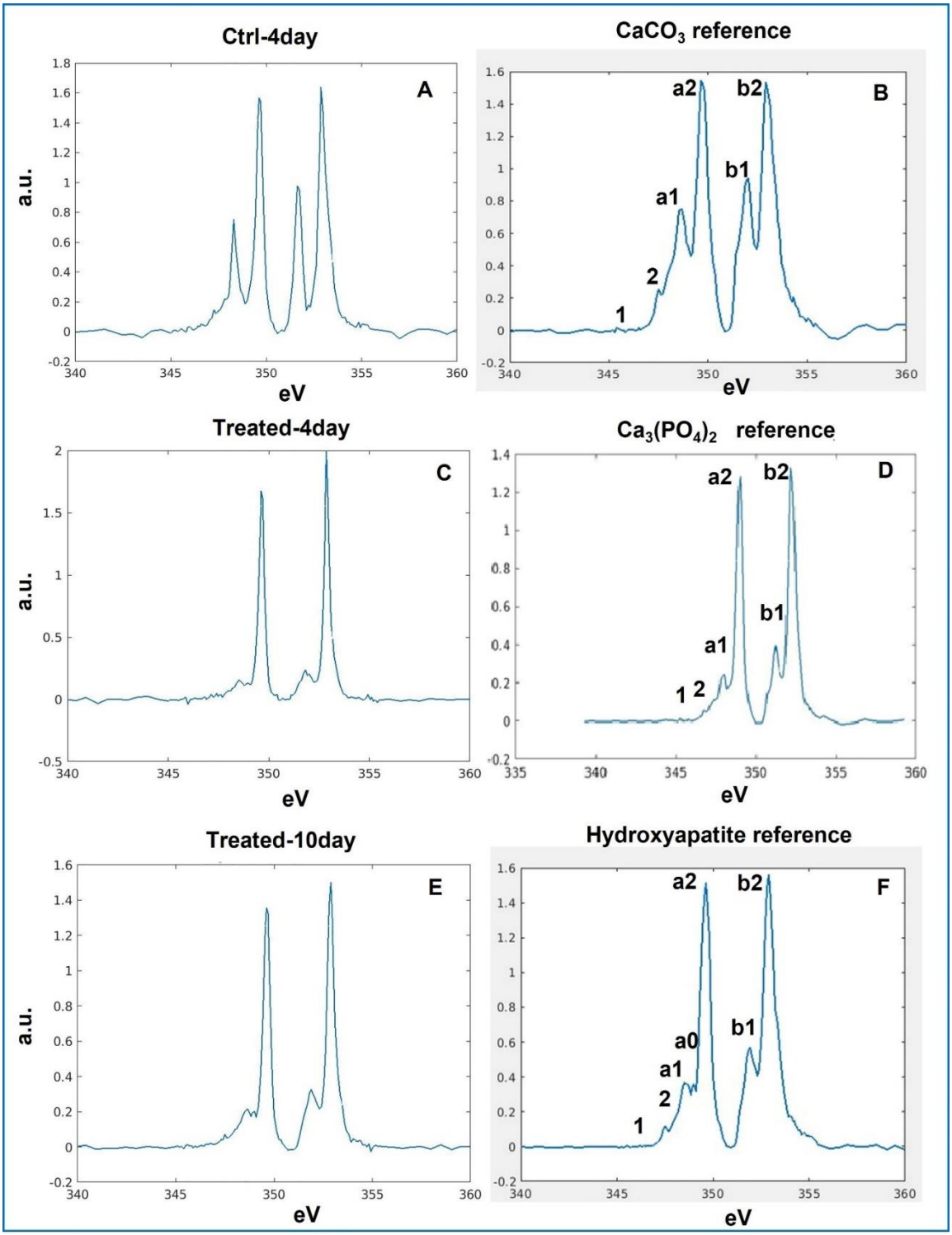

Figure 6 Cryo-XANES spectra of control and treated SaOS-2 cells after 4 and 10 days of osteogenic induction. (A) and (B) showed respectively the XANES spectrum of $CaCO_3$ detected in Control sample at 4 days and $CaCO_3$ reference spectra. (C) Representative $Ca_3(PO_4)_2$ spectrum in treated sample at 4 days; (D) $Ca_3(PO_4)_2$ reference spectrum. (E) and (F) showed respectively HA representative spectra detected in SaOS-2 cells after 10 days of osteogenic treatment and the HA reference spectra. In B, D, F the main spectral features are indicated by letters and number.

The representative spectrum of HA (**Fig. 6F)** shows the main characteristic L_3 and L_2 peaks of calcium compounds, respectively at 340 eV and 352.9 eV (a2 and b2 peaks in **Fig. 6F**), the small intensity peaks structure before the L_3 main peak (a1, a0 in **Fig. 6F**) and the "hook" shape of the L_2 pre-peak (b1 in **Fig. 6F**). These features can be observed also in the representative Ca-deposits spectrum of a treated sample at 10 days of induction (**Fig. 6E**).

The XANES spectroscopy provides a structural information about the Ca chemical state. A typical Ca $L_{3,2}$-edges spectrum of calcium compounds presents two main peaks ($L_3 \approx 340$ eV; $L_2 \approx 352.9$ eV) and a "multi-peak pattern" of relatively lower intensity before L_3 and L_2 main peaks. The "multi-peak pattern" distinguishes the crystalline phases from the amorphous ones both in calcium carbonates and in calcium phosphates compounds. In fact, these low intensity peaks correspond to transition towards crystalline states which do not exist in the amorphous case [200–202]. In our samples an evolution of Ca-compounds in the cell mineral depositions was observed. After 4 days of osteogenic induction, all the spectra extracted from the depositions of the control sample matched the calcium carbonate reference spectra. The treatment with the osteogenic cocktail induces a change in the crystalline structure of Ca-deposits both at early phase of differentiation (4 days) and at longer time scale (10 days). Indeed, all the Ca mineral depositions analyzed in the treated samples show absorption spectra that can be attributed to calcium phosphate and hydroxyapatite crystals. The mechanism according to which the formation of crystalline HA passes through amorphous calcium carbonate and calcium phosphate compounds has been described

in vitro by Marchegiani and colleagues [203] and recently demonstrated in bone marrow stem cells [31].

The fact that this evolution also occurs in SaOS-2 osteosarcoma cells, leads us to suppose that the differentiating treatment is able to restore the physiological biomineralization process.

We investigated also the intra-vesicular Ca-content in the ctrl and treated sample at 4 days of treatment. For both samples, the XANES spectrum of the intra-vesicular Ca-nodules (**Fig. 7**) was very noisy, probably because of the lower concentration of calcium. At 10 days of treatment, we observed an increase in extravesicular depositions, and a decrease in vesicles, as also shown by the results obtained from TEM microscopy.

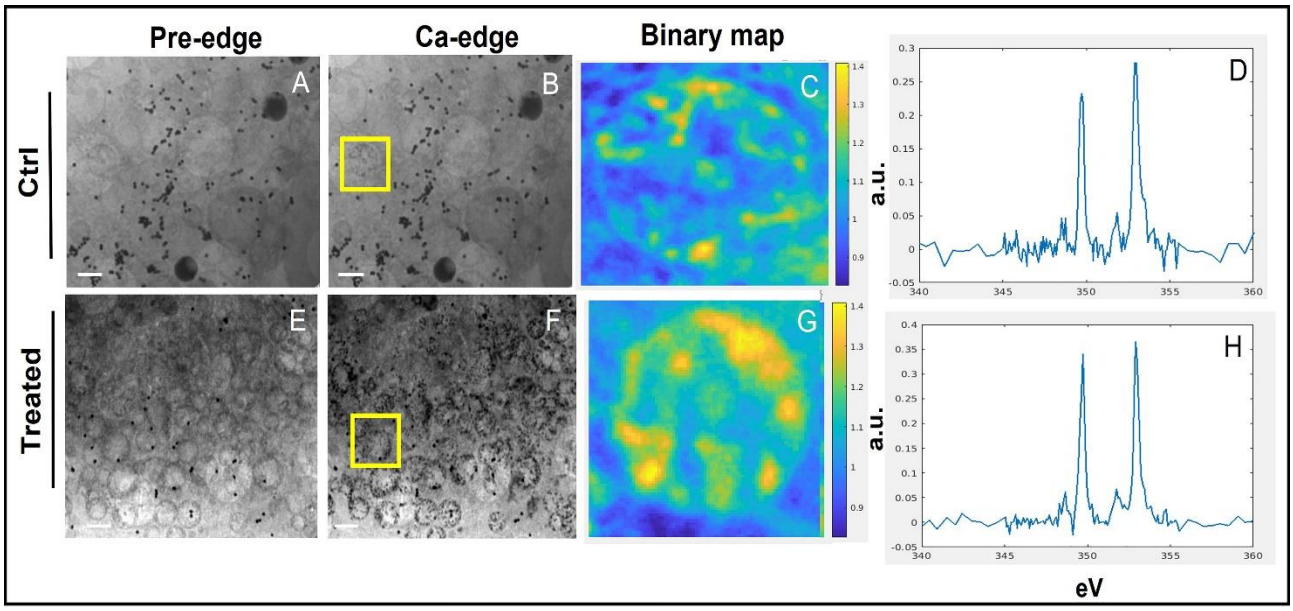

Figure 7 Average of absorbance projections of a cytoplasm cell region recorded at pre-Ca-edge energy region (≈ 342 eV) and at the Ca L_3 peak maxima (≈349 eV), respectively for Ctrl-4days (A, E) and Treated-4days (B, F). C, G) Binary absorbance map of vesicles in control and treated samples after 4 days of treatment: yellow regions correspond to the Ca-depositions. D, H) Average of XANES spectra of intra-vesicular Ca-depositions. Scale bar is 250 nm.

The Cryo-SXT tomography was carried out at 352.9 eV to optimize the contrast between calcium-rich objects, carbon dense structures and the surrounding water-rich cytoplasmic solution. In **Fig. 8A** is reported a ROI in the cytoplasm of the same treated sample shown in **Fig. 5** (**G**, **H**, **I**), where the Ca-rich object strongly absorbed the incoming radiation. We performed the 3D rendering of the intracellular structures and Ca mineral depositions (**Fig.8B**) to better visualize the 3D information given by the reconstructed electron density and to define the distribution of Ca-depositions.

In **Fig.8B** the green and violet spots indicate respectively the extra-vesicular and intra-vesicular calcium depositions, while the nucleus is shown in blue. It is evident that Ca depositions were grouped in cluster of different dimensions and localized inside or in proximity of big vesicles. A zoomed tomographic image of one vesicle is shown in the **Fig.8 C** and the respective 3D rendering of the calcium depositions contained in it is reported in **Fig.8D**.

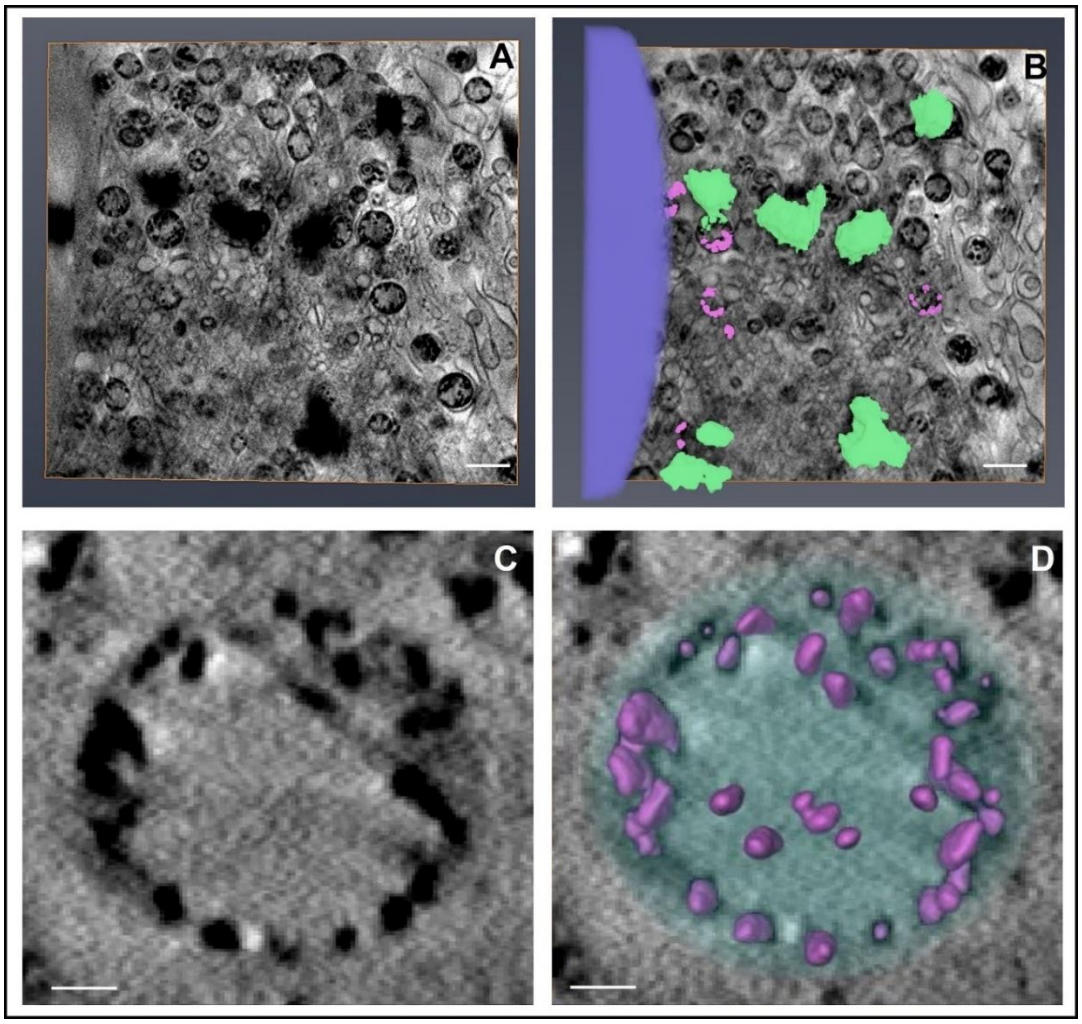

Figure 8 A) Cryo-SXT slice of SaOS-2 Treated-10 days collected at 352.9 eV and obtained by tomographic reconstruction. B) Corresponding color-coded 3D rendering (with the nucleus in blue, intra-vesicular Ca depositions in violet and extra-vesicular Ca-depositions in green). Scale bar is 500 nm. C) Zoom of vesicle containing Ca-dense objects. D) Corresponding color-coded 3D rendering of Ca-deposits (violet spots). Scale bar is 50 nm. For the 3D rendering the Ca-dense objects were automatically selected using a threshold.

The results obtained from Cryo-XANES microscopy and Cryo-SXT confirmed the presence of intra-vesicular and extra-vesicular Ca-mineral material. This may be due to the co-existence of several biomineralization processes: i) a mechanism mediated by membrane enzymes, such as ALPL, that participate in the nucleation of calcium phosphate outside the cell, at the intra and interfibrillar collagen level, and then crystallizes into hexagonal HA [204]; ii) the mineralization initiated by matrix vesicles

(MVs) containing enzymes for accumulation of CaP ion precursors (Pi and Ca^{2+}) and transporters to drive the mineral deposits from the cytoplasmic environment to the outside [205,206].

Moreover, since it is previously reported that MVs contain a variety of proteins [199] we supposed that the amorphous calcium depositions found within the vesicles could be associated to these proteins involved in intravesicular formation of ACP minerals.

4.1.7 Bio-energetic profile assessment by Mito-stress Seahorse assays

We investigated if early commitment to differentiation of SaOS-2 cells was associated with altered bioenergetic profiles by measuring real-time O_2 consumption (OCR) in 2D cell cultures. Cell Mito Stress Test was performed by Seahorse XFe96 Analyzer. The cells were seeded in appropriate multi-well 4 days before the analysis and treated after 24 and 72 hours from the seeding with osteogenic cocktail.

As shown in **Fig. 9**, the level of basal respiration (which occurs in absence of mitochondrial inhibitors and represents the sum of all mitochondrial O_2-comsuming processes) had a tendence to increase in treated SaOS-2 cells respect to controls, but without significant relevance. The injection of oligomycin, an inhibitor of the mitochondrial ATP synthase, leads to a decrease in basal respiration that is proportional to mitochondrial activity used to generate ATP. The further addition of FCCP, a proton ionophore which uncouples respiration from oxidative phosphorylation, allowed for the measurement of maximal respiratory rates. We observed a significantly increase of maximal respiration levels during osteogenic differentiation rather than in control samples.

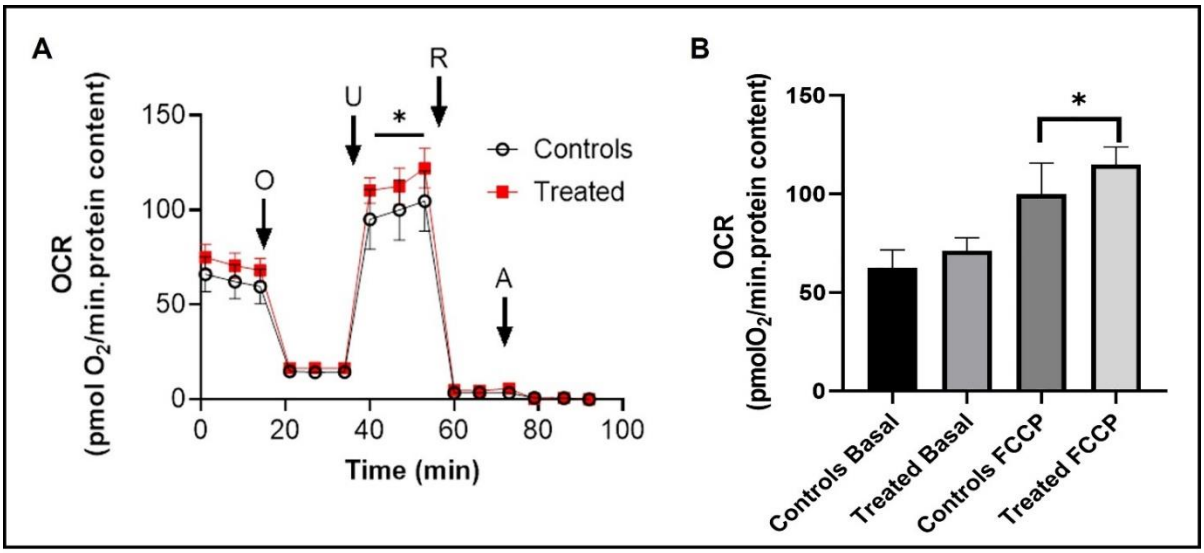

Figure 9 Seahorse XFp Cell Mito Stress Test assays in SaOS-2 cells after 4 days of treatment with osteogenic cocktail. A) Oxygen consumption rate (OCR) in Ctrl and Treated samples after 4 days of treatment with sequential injection of Oligomycin (O), Carbonyl cyanide-4 (trifluoromethoxy) phenylhydrazone ([FCCP] U), Rotenone, and Antimycin (R). Multiple t-test was performed, *p < 0.1. B) Mean value results of basal respiration rate and maximal respiration rate, after FCCP injection. Both rates were normalized against cell proteins and expressed as rate per protein content; T-student paired test was performed, *p<0.1. All data are presented as mean± SEM n = 5 technical replicates from five biological samples for each group.

According to literature [207], this result could be explained by the upregulation of mitochondrial biogenesis occurring during the differentiation process. Moreover, this overexpression of the mitochondria could be associated both with a greater energy demand during osteoblastic induction, and with a direct involvement of the mitochondria in the ionic calcium transpose chain. Indeed, Boonrungsiman et al. suggested a role for mitochondria in the trafficking of ions or clusters of calcium and phosphate ions. Supporting other studies, they assumed that mitochondria act as storage depot of calcium and phosphate ions, transferred by diffusion to intracellular vesicles and facilitating mammalian mineralization [208].

4.2 Differentiating effect of 3D cultured SaOS-2 cells

4.2.1 Characterization of 3D cultures on Collagen Scaffolds

To monitor the cell viability and proliferation rate of SaOS-2 cells grown on collagen scaffolds, cell counts at 1, 3, 7, and 14 days from the seeding were performed.

The doubling time was around 36 hours, in agreement with the literature regarding SaOS-2 cell line during exponential phase growth (**Fig. 10a**). The viability of 3D cultured cells was about 80% until the 7th day of culture, and significantly decreased in the following days up to 60%, when the plateau phase was clearly visible (**Table 1**).

To better characterize the cell proliferative activity, cell cycle analysis was performed by cytometry. DNA profile indicates that cells were highly proliferating at day 3, while they slow down when reaching confluence. As shown in **Fig. 10b**, the percentage in G0/G1 phase changed from 61% to 76%, and S phase halved from 30% to 15% [209]. As such, we observed a regular cell growth pattern in 3D scaffold. Cell cycle progression confirms that a collagen matrix is suitable for tissue-like growth of SaOS-2 osteosarcoma cells *in vitro*.

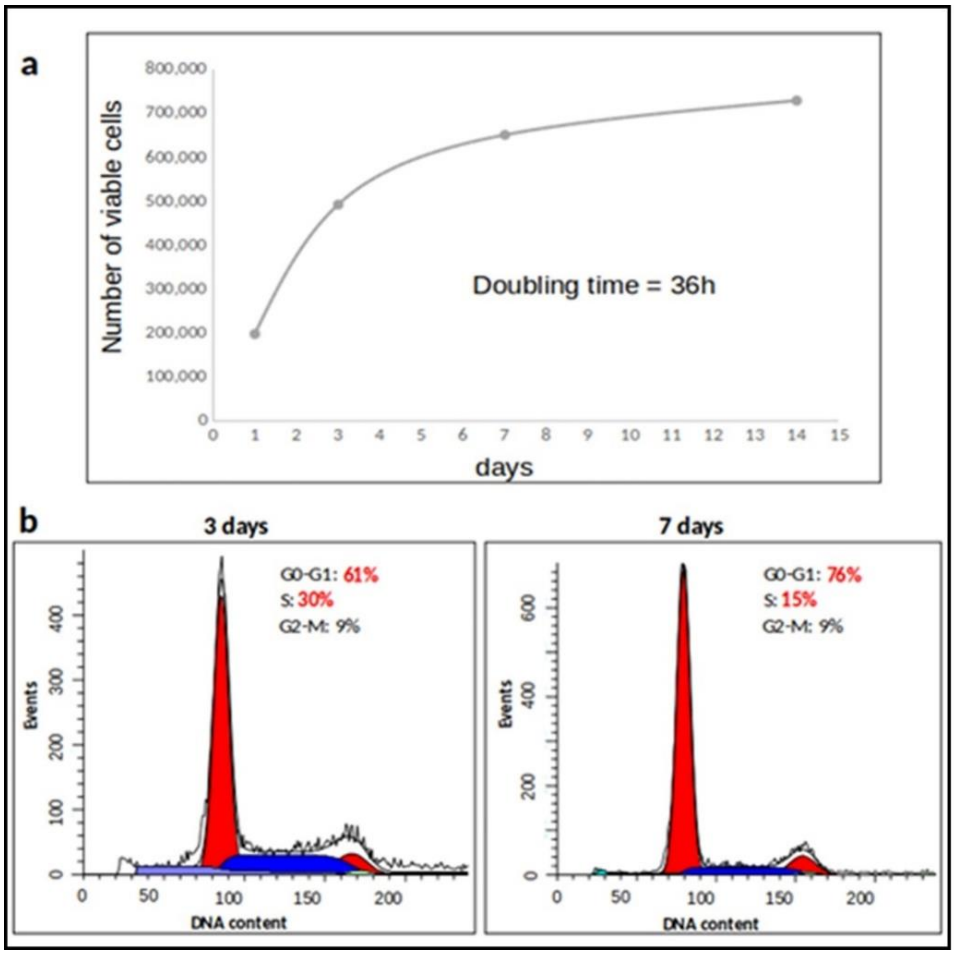

Figure 10. Assessment of 3D cell culture conditions. (a) cell growth curve; (b) cell cycle analysis. The figure depicts the results obtained in one experiment representative of three.

Table 1. Percentage of cell viability of SAOS-2 cells grown on collagen scaffold at 1,3,7 and 14 days after seeding. Viability count of cells was performed by staining with erythrosine (0.1% in PBS).

	% Live cells	**% Dead cells**
Ctrl 1 day	75.99%	24.0%
Treated 1 day	83.09%	16.9%
Ctrl 3 day	85.53%	14.47%
Treated 3 day	77.39%	22.61%
Ctrl 7 day	71.91%	28.09%
Treated 7 day	66.01%	33.99%
Ctrl 14 day	64.22%	35.78%
Treated 14 day	56.58%	43.42%

4.2.2 Osteogenic Gene Expression Analysis

To verify the induced differentiation of 3D cultured cells, the gene expression analysis of four osteogenic markers was evaluated by real-time qPCR (**Fig. 11)**. Among the tested genes, the late osteogenic markers osteocalcin and osteopontin showed a strong increase of their mRNA expression levels, already after 3 days of treatment, compared to their controls. In detail, the upregulation of osteocalcin and osteopontin genes was 41.7-fold (p-value < 0.01) and 3.1-fold (p-value < 0.05) higher, respectively. After 7 days of treatment, their levels were maintained overexpressed 47.4-fold and 5.5-fold, respectively, compared to their specific control counterparts (p-values < 0.01).

The early osteogenic commitment transcription factor *RUNX2* showed comparable level of expression during time. On the other hand, although not significant, a trend in the upregulation of the other early osteogenic marker collagen type 1 (*COL1A1*) was scored, showing about a two-fold increase in its mRNA expression level at both experimental time points with respect to control [209].

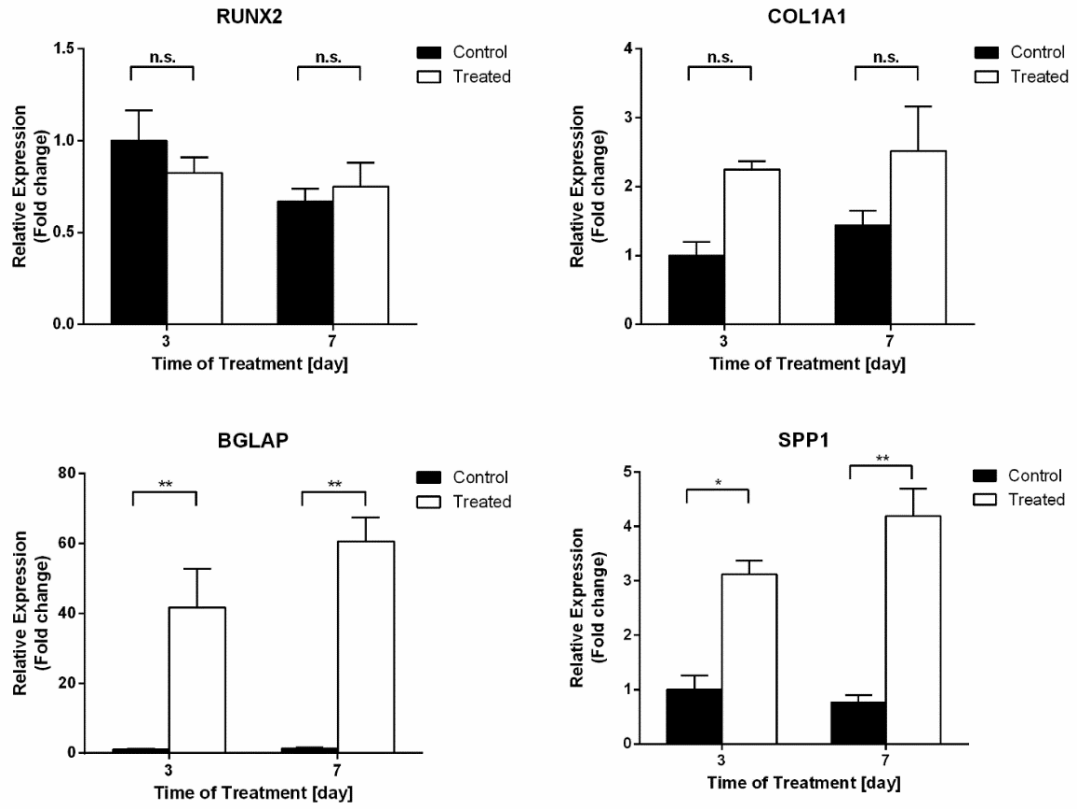

Figure 11. Analysis of SaOS-2 cells cultured in 3D collagen scaffolds (3 and 7 days) treated with the osteogenic cocktail. qPCR analysis of osteogenic markers (*RUNX2*, *COL1A1*, *BGLAP*, and *SPP1*) was performed using GAPDH and HPRT1 as reference genes (2-ΔΔCT method). Fold changes from control untreated cells at day 3 were calculated. Data are reported as mean ± SEM of three biological replicates. * $p < 0.05$; ** $p < 0.01$.

Altogether, this gene expression profile suggests that the osteogenic commitment of cells is already well active few days after the induction. The constitutively elevated levels of *RUNX2* mRNA in control cultures is likely to account for a lack of its further upregulation when the cells have been stimulated with osteogenic cocktail [210]. On the other hand, a significant increase of *BGLAP*, and *SPP1*, together with an apparent, although not statistically significant, trend towards the upregulation of *COL1A1*, was recorded in response to treatment at both days 3 and 7, demonstrating a successful activity of the administered molecular cocktail over SaOS-2 osteogenic function.

4.2.3 Histochemical Analysis of Mineralization in Collagen SaOS-2 Cells-laden scaffolds

To assess the distribution of cells inside the collagen scaffolds, 10 μ-thick sections were marked by classical Hematoxylin/Eosin (H/E) staining. The results reported in **Fig. 12a** show uniformly fitted cells. Larger numbers of cells were found in control samples respect to treated ones, since a slowdown of proliferation is expected consistently with the commitment towards a more differentiated phenotype. Alizarin Red S staining highlighted the presence in treated samples of nodular aggregates containing calcium, after only 3 days. The red spots were larger and more intensely stained at day 7, suggesting that a more extensive calcium deposition had occurred. In addition, to quantify the size of the red stained area covering the scaffold slices, four masks (n = 4) for each image acquired were analyzed using the maximum entropy threshold-based image segmentation method. **Fig. 12b** shows a significant increase of areas covered by Ca depositions at both 3 and 7 days after osteogenic induction. [210]. In summary, the alizarin staining showed many mineral nodular aggregates in treated cells, already after 3 days, demonstrating that SaOS-2 cells represent a suitable model for studying human osteoblast differentiation and responsiveness *in vitro*.

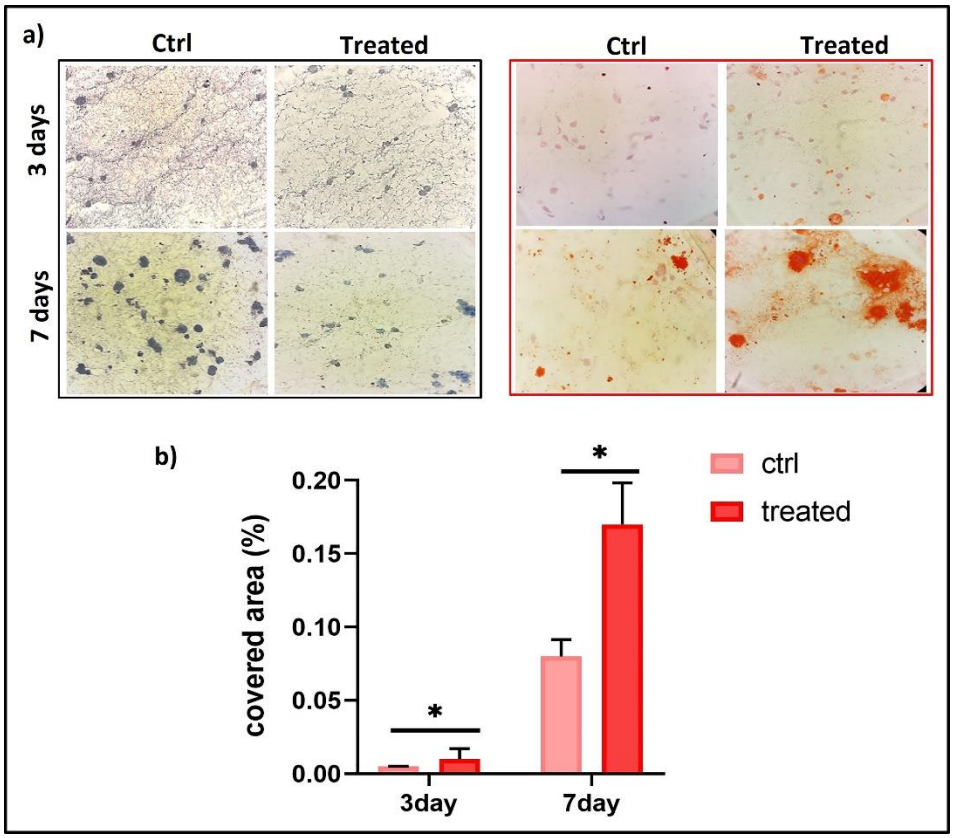

Figure 12 H/E ((a) left panel) or Alizarin Red ((a), right panel) staining of paraffin-embedded sections of 10 μm thickness (n = 3); (b) quantification of Alizarin-stained Ca depositions. Data are reported as means ± standard error of the mean, values deriving from a triplicate experiment. *$p < 0.05$.

4.2.4 Monitoring of intracellular Magnesium and X-ray fluorescence microscopy of mineral deposits

Several authors described a relationship between differentiation and magnesium availability, indicating a role for the cation even if not fully understood. To verify the involvement of magnesium in osteoblast differentiation, we assessed its intracellular concentration by highly sensitive DCHQ5 fluorescent dye. The osteogenic induction of 3D cultured cells was accompanied by a marked increase of magnesium concentration, both 3 and 7 days. A two-fold increase in the intracellular content of the treated samples with respect to their control has been observed (**Fig. 13A**). This result is in agreement with other studies demonstrating a pivotal role of Mg in bone differentiation involving the ERK/BMP2/Smads signaling pathway [211,212].

This finding poses the question as to whether Mg is present in the mineral Ca depositions produced in the early phase of biomineralization, and in which temporal phase is incorporated in the hydroxyapatite crystal, being Mg one of the Ca-substituting element in mature bone

Therefore, we characterized the chemical composition of the mineral depositions in differentiating 3D cultured SaOS-2 cells by X-ray fluorescence microscopy at the TwinMic beamline @ Elettra synchrotron [213]. In particular, we evaluated the Mg and P content in the mineral depositions. **Fig. 13** panel **B** represents the elemental map of a deposition and highlights the co-localization of Mg with P at 7 days of differentiation, indicating the presence of magnesium in the mineral depositions already in the early phases of biomineralization [209]. This evidence confirms many publications stating that the mineral fraction of bone is composed of HA, a non-stoichiometric Ca-compound containing trace elements such as Zn, Mg which are the main substituting cations in the crystal lattice of HA [214,215].

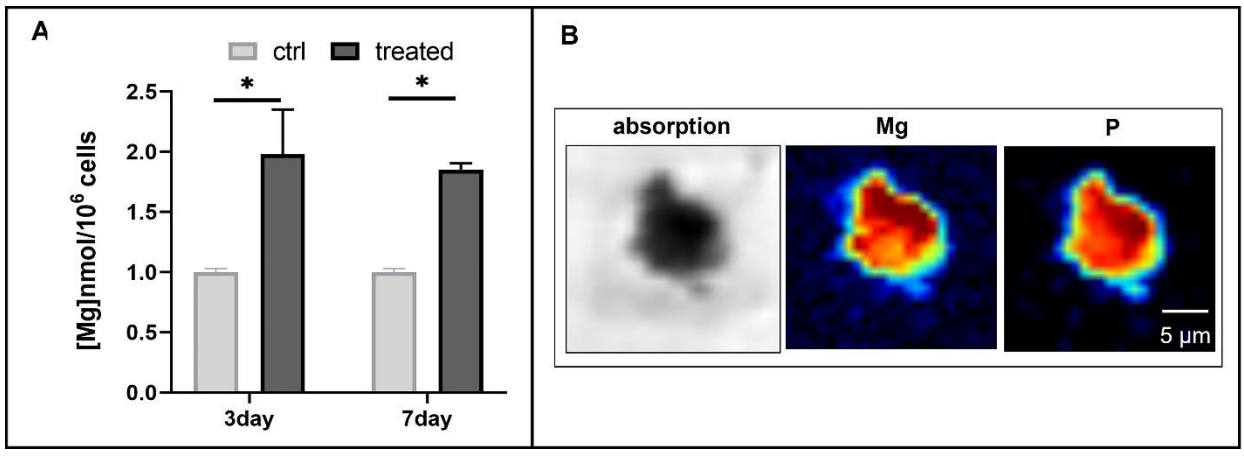

Figure 13 A) Fluorimetric assay of total intracellular magnesium content by DCHQ5 probe [183]; B) describes the Mg and P co-localization in a deposition released by a differentiating SaOS-2 cell at the TwinMic beamline of Elettra synchrotron.

4.2.5 Analysis of Mineral Depositions by X-ray Microtomography Techniques

With the aim to characterize and quantify the extracellular depositions, fixed scaffolds were imaged by phase-contrast microfocus X-ray µCT (Computed Tomography) at the TomoLab station [190] of the Elettra synchrotron light source. **Fig. 14** shows the 3D spatial distribution of the depositions in the whole scaffolds after 7 days of osteogenic induction (panel (**b**)) and in a control sample (panel (**a**)). Two representative volumes of interest (VOIs) (panel (**c**) and (**d**)) inside the scaffold (CTRL volume = 1.8 mm^3; treated volume = 1.2 mm^3) were analyzed by the ImageJ plug-in BoneJ [216]. A higher amount of depositions fraction compared in 7 days differentiated cells (0.80%) respect to the controls (0.31%) (table in **Fig. 14**). In addition, single-particles analysis showed that the volume of the depositions in differentiated sample was significantly lower (p-value < 0.001) with respect to the depositions present in the control ones (**Fig. 14**, **a**, and **c**). The graph classified the particles dimension (µm^3) in relation to the number of particles within the class [209].

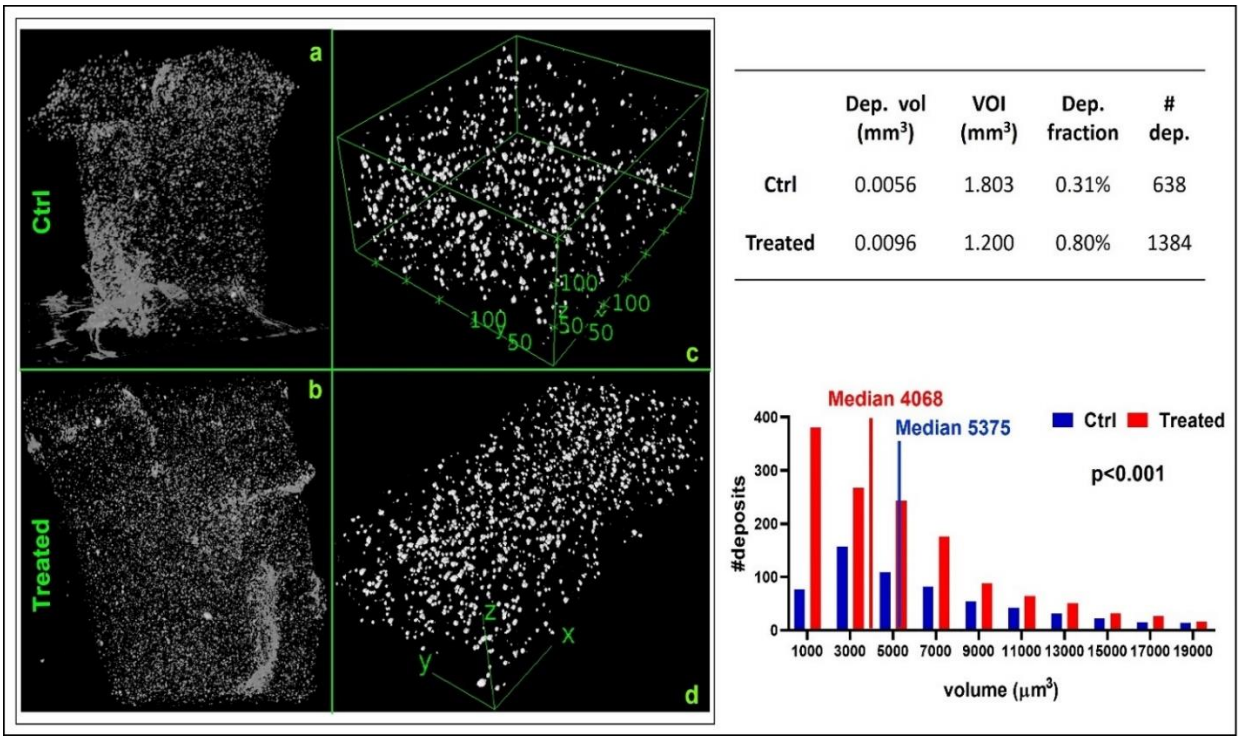

Figure 14 X-ray analysis of depositions released by SaOS-2 cells. Panels (**a**) and (**b**) depict the 3D distribution of mineral depositions in the whole control and treated scaffolds imaged by microfocus X-ray µCT at the TomoLab station of Elettra (isotropic voxel size = 5 mm for the control and 3.3 mm for the treated sample). The dimensions of the scaffolds are approximately 80 mm^3. Panel (**c**) and (**d**) show two selected VOIs reporting the depositions distribution in ctrl (6000 × 4300 × 700 mm^3) and treated scaffolds (7300 × 1200 × 800 mm^3) respectively. Table and graph show the descriptive statistical analysis of the depositions in the two representative VOIs showed in panel c (Ctrl) and d (treated), respectively. The graph classified the particles dimension (μm^3) in relation to the number of particles within the class.

Furthermore, a treated scaffold was imaged at the SYRMEP beamline of Elettra [191] by phase-contrast synchrotron X-ray µCT (**Fig. 15**) reaching a spatial resolution of the order of 1 µm. **Fig. 15** panel (**a**) shows a reconstructed tomographic slice with a reduced spatial resolution that highlights the presence of mineral depositions along brighter filament indicating a not random pattern. Depicted in panel (**b**) of **Fig. 15** is the region of interest indicated in green in panel (**a**) with the full spatial resolution of the system. To better understand the spatial distribution of both depositions and filaments a 3D rendering of 50 adjacent slices is reported in **Fig. 14 c** [209].

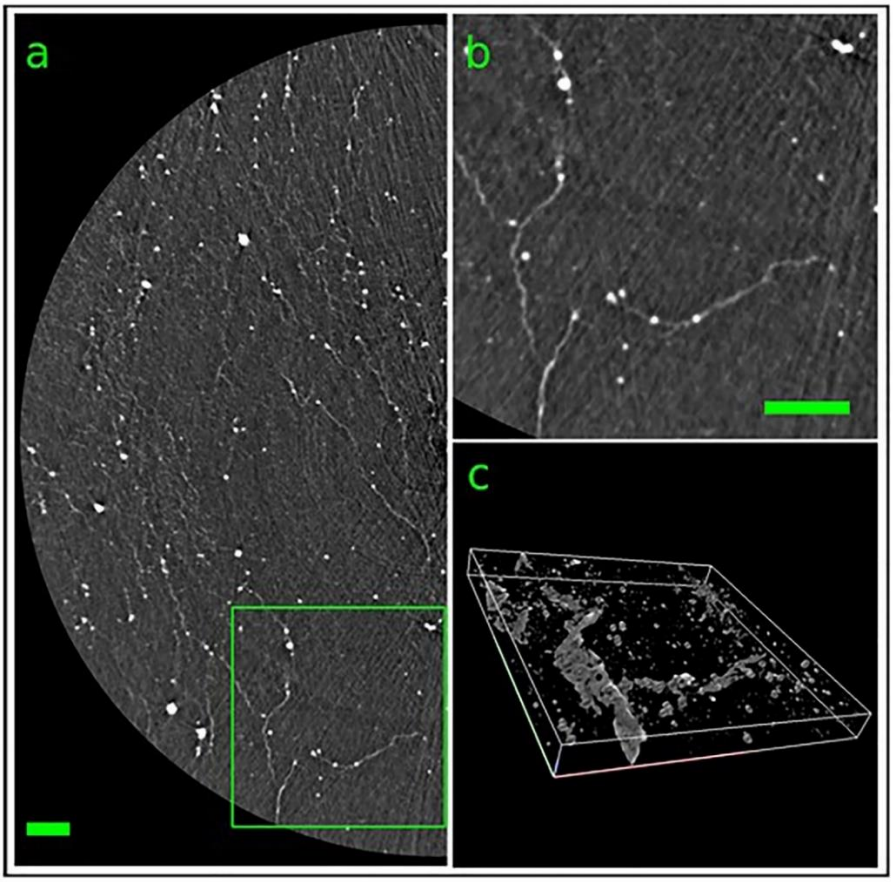

Figure 15 Synchrotron-based X-ray μCT analysis of one treated scaffold imaged at the SYRMEP beamline of Elettra. Panel (**a**) represents a reconstructed axial slice of the scaffold (isotropic voxel size = 0.9 mm) highlighting the presence of mineral depositions (white dots) along brighter filaments. Panel (**b**) shows a zoom of the green ROI (region of interest) indicated in panel (**a**). Panel (**c**) depicts a 3D rendering of 50 adjacent slices (400 × 400 × 50 mm^3) showing the 3D distribution of the mineral depositions. Scale bars is 100 mm.

These techniques provided a 3D spatial distribution map of the mineral depositions generated by SaOS-2 cells. We found an increase of biomineralization in differentiating SaOS-2 cells revealed by near 3-fold higher number of depositions in scaffold with differentiated cells treated samples. Nevertheless, the average volume of single depositions in the treated sample was lower than those of the control one. We speculate that the decrease of deposition volume could be related to the evolution of the amorphous Ca compounds into crystalline HA during the biomineralization process. To corroborate this hypothesis, in a recent study on differentiating stem cells,

we found that the mineral amorphous depositions rapidly evolve toward hexagonal HA crystal, similar to those present in mature human bone [35].

There are many evidences that collagen microfibrils direct the formation of nanosized HA platelets oriented parallel to the collagen fibril axis [217,218] for interfibrillar mineralization [219]. Indeed, synchrotron-based X-ray micro-tomography showed many depositions following an oriented pattern along denser filaments, as clear in **Fig. 15**. Nevertheless, as previously reported in gene expression analysis we found an overexpression of COL1A1 gene, coding for collagen type 1, and speculate that the observed filaments could be the neo-formed collagen fibrils produced by differentiating cells.

4.2.6 Characterization of 3D cultured SaOS-2 cells on CTL/agarose scaffold

Before to induce the osteogenic differentiation, the viability and spreading of SaOS-2 cells encapsulated within the CTL/agarose scaffolds was evaluated. Alamar cell viability assay was performed at 3 different time point (1, 4 and 7 days after seeding). As shown in **Fig. 15A**, the percentage of cell viability at 7 days was almost 70% respect to the day 1. To confirm this result, fluorescence images of live/dead assay was collected by confocal microscope (**Fig. 16C**) and the number of live and dead cells was calculated by using a Imagej plugin. The percentage of cell death shown in the table (**Fig. 16B**) was perfectly in agreement with the result obtained by alamarBlue assay. Moreover, phalloidin/Hoechst staining was performed for assessing the cell spreading and shape within scaffold. In **Fig. 16D**, three representative images were reported for each time point. Green color represents actin filaments and blue represents nuclei. The cells maintained a circular shape over time, without any spreading. Probably this depends on the viscoelasticity of hydrogel, that influenced the cell behaviour as previously reported [220].

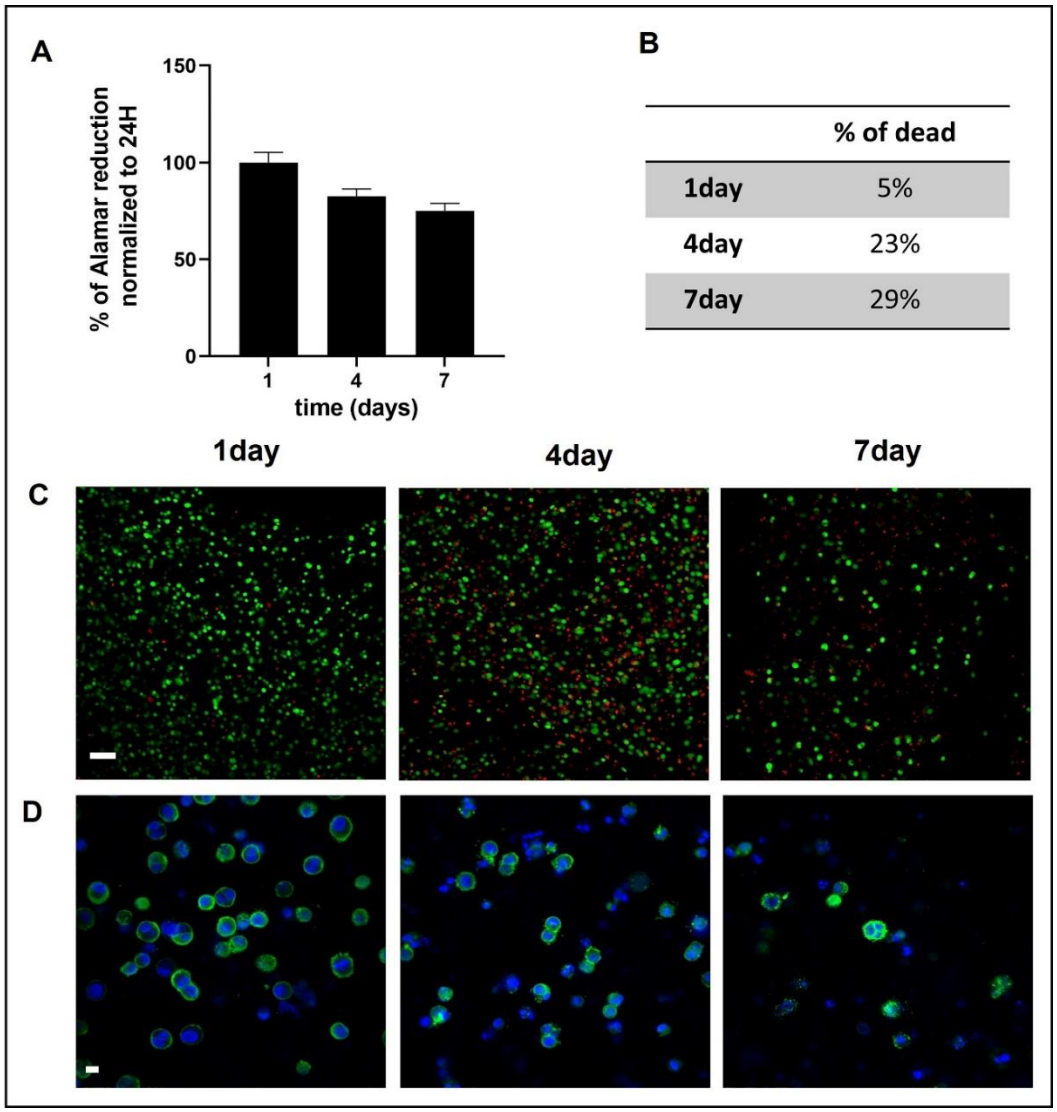

Figure 16 Cell viability and spreading for SaOS-2 cells encapsulated within CTL/agarose scaffolds. A) Cellular metabolic activity determined by the Alamar Blue metabolic assay. Data were shown as percentage of Alamar blue reduction at different time points respect to the Alamar reduction at 24 h B) Percentage of cell death over time. C) Fluorescence images of a live/dead assay: green colour represents live cells; red colour represents dead cells, magnification 20×. D) Fluorescence images of Phalloidin/Hoechst staining: green colour represents actin; blue colour represents nuclei; magnification 40×. The pictures are reported as representative of three independent experiments. Scale bar is 10 µm.

4.2.7 Cell viability and Alizarin Red staining of CTL/agarose SaOS-2 cell-laden scaffolds

To evaluate the osteogenic differentiation of SaOS-2 cells also in CTL/agarose scaffolds, the 3D cultures were treated with osteogenic cocktail and monitored for 10 days. The viability of cells was assessed by Alamar blue metabolic assay at 1,4,7 and 10 of treatment. As shown in **Fig. 17A**, on day 1 and 4 both the control and treated groups showed a high viability. From 7 days of cultivation the cell viability went down, becoming about the 50% on 10 days, respect to the beginning of experiment both for control and treated samples. Nonetheless, any significant difference between control and treated samples was evident.

The formation of mineral calcium depositions in CTL/agarose scaffolds following the osteogenic induction was assessed by Alizarin Red S staining at 4, 7, 10 days. Alizarin Red S staining results showed in **Fig. 17B**, indicated that also in this kind of scaffold, the osteogenic cocktail promoted a high osteogenic differentiation. As show in the left panel of **Fig. 17B**, the treated samples were more intensely stained than the control ones, already 4 days after osteogenic induction. These results were further confirmed by spectrophotometric quantification of Alizarin red dissolved by CPC. The graph in **Fig. 17B** showed a significant increase of absorbance in the treated groups at all three-time points respect to the control counterpart.

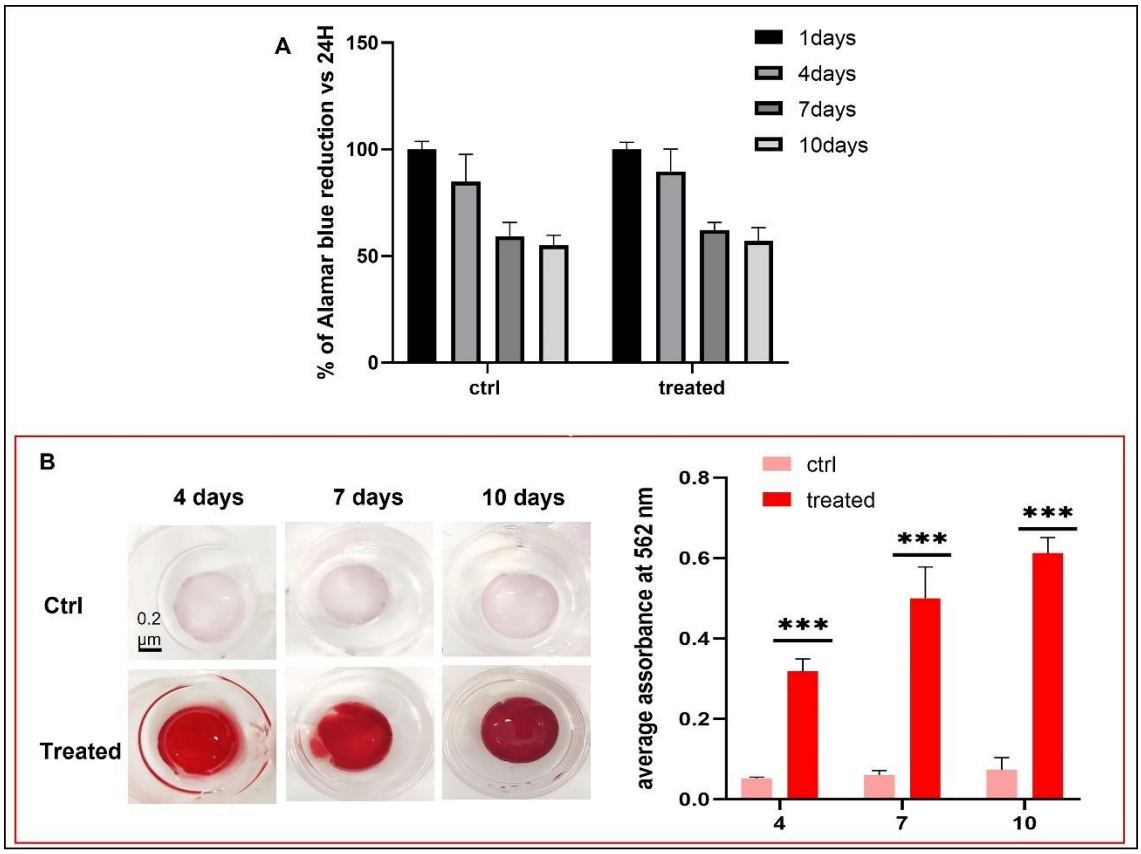

Figure 17 A) Cellular metabolic activity determined by the alamarBlue metabolic assay on treated and untreated within scaffold after 1,4,7 and 10 days of osteogenic induction. Data were shown as percentage of alamarBlue reduction at different time points respect to the alamar reduction at 24 h. **B)** Alizarin red staining and quantification of mineralized Ca deposits in CTL/agarose scaffold. In the left panel control and treated samples show the differences over the time. A single experiment is shown as representative of three independent ones. In the right panel, histogram shows the corresponding staining quantification and represents the mean values of three experiments. Two-way ANOVA followed by a Sidak's multiple comparison test was performed, *** $p < 0.001$.

The results obtained from cell viability test revealed that the CTL/agarose hydrogel was biocompatible and no cytotoxic effect on SaOS-2 cells was observed. The metabolic activity reduction at longer time scale is probably due to a restriction of medium diffusion in the core of scaffold, followed by insufficient nutrient and oxygen supply (hypoxia) and waste accumulation (acidification) for cells in the core region a typical condition for 3D cell culture [221].

CTL/agarose scaffold thus proved to be a promising hydrogel, useful for mimicking bone as well as cartilage tissue, as previously reported [194,222].

Further investigations are underway for the extraction of RNA and for the gene expression analysis necessary to confirm the differentiation in these new types of scaffolds.

5. Conclusion

This PhD project focused on the study of the early stages of bone biomineralization by evaluating the genesis of the mineral nuclei depositions and their evolution in a human osteosarcoma cell line exposed to an osteogenic cocktail.

This study allowed the validation of the SaOS-2 cell line as an osteoblast-like model suitable for both two- and three-dimensional *in vitro* systems and for ultrastructural investigations of bone biomineralization process.

The results obtained revealed that the osteogenic differentiative stimulus induced changes in the osteoblastic genes expression, in the mitochondrial respiration and in the production and evolution Calcium mineral depositions.

SaOS-2 cells after osteogenic induction showed a behaviour similar to that of differentiating hbMSCs, previously reported, with the formation of HA crystals, passing through the deposition of Calcium carbonate minerals.

This result provides the evidences about the possibility of a therapeutic strategy acting on the reversibility of tumorigenicity, following the osteogenic induction. Since several studies pointed out that osteosarcoma development is associated with defects in osteogenic differentiation, a new promising strategy could be sensitizing osteosarcoma cells to chemotherapy and inducing to differentiate the survived cells, with the irreversible loss of tumour phenotype.

In summary, the multi-modal and multiscale approaches have allowed to investigate different aspects of a complex phenomenon such as the osteosarcoma biomineralization, leading to a greater understanding of how this process occurs both in 2D and 3D *in vitro* models.

Future developments will be a deeper characterization of Ca-depositions by diffraction techniques and of matrix vesicles by TEM-EDX and fluorescence microscopy and, the investigation of mitochondria involvement at longer time scale. Moreover, it would be interesting to study the tumor microenvironment (cell-cell interaction and extracellular matrix) in the 3D cultures, using collagen and CTL scaffold templates within a

bioreactor system that simulates perfusion and compression to obtain a system as close as possible to the *in vivo* one. Nevertheless, these innovative 3D models could be used to test new therapeutic options, as well as the application of differentiative induction as desirable approach for the osteosarcoma treatment.

6. References

1. Tang, S.; Dong, Z.; Ke, X.; Luo, J.; Li, J. Advances in Biomineralization-Inspired Materials for Hard Tissue Repair. *Int J Oral Sci* **2021**, *13*, 42.

2. Weiner, S.; Wagner, H.D. THE MATERIAL BONE: Structure-Mechanical Function Relations. *Ann Rev Mater Sci* **1998**, *28*, 271–298.

3. Gorski, J.P. Biomineralization of Bone: A Fresh View of the Roles of Non-Collagenous Proteins. *Front Biosci (Landmark Ed)* **2011**, *16*, 2598–2621.

4. Florencio-Silva, R.; Sasso, G.R. da S.; Sasso-Cerri, E.; Simões, M.J.; Cerri, P.S. Biology of Bone Tissue: Structure, Function, and Factors That Influence Bone Cells. *Biomed Res Int* **2015**.

5. Sroga, G.E.; Karim, L.; Colón, W.; Vashishth, D. Biochemical Characterization of Major Bone-Matrix Proteins Using Nanoscale-Size Bone Samples and Proteomics Methodology. *Mol Cell Proteomics* **2011**, *10*, M110.006718.

6. Donnelly, E.; Meredith, D.S.; Nguyen, J.T.; Boskey, A.L. Bone Tissue Composition Varies across Anatomic Sites in the Proximal Femur and the Iliac Crest. *J Orthop Res* **2012**, *30*, 700–706.

7. Boskey, A.L. Bone Composition: Relationship to Bone Fragility and Antiosteoporotic Drug Effects. *Bonekey Rep* **2013**, *2*.

8. Hart, N.H.; Nimphius, S.; Rantalainen, T.; Ireland, A.; Siafarikas, A.; Newton, R.U. Mechanical Basis of Bone Strength: Influence of Bone Material, Bone Structure and Muscle Action. *J Musculoskelet Neuronal Interact* **2017**, *17*, 114–139.

9. Corradetti, B.; Taraballi, F.; Powell, S.; Sung, D.; Minardi, S.; Ferrari, M.; Weiner, B.K.; Tasciotti, E. Osteoprogenitor Cells from Bone Marrow and Cortical Bone: Understanding How the Environment Affects Their Fate. *Stem Cel ls Dev***2015**, *24*, 1112–1123.

10. Nahian, A.; Davis, D.D. Histology, Osteoprogenitor Cells. In *StatPearls*; StatPearls Publishing: Treasure Island (FL), **2020.**

11. Caplan, A.I.; Bruder, S.P. Mesenchymal Stem Cells: Building Blocks for Molecular Medicine in the 21st Century. *Trends Mol Med* **2001**, *7*, 259–264.

12. Rutkovskiy, A.; Stensløkken, K.-O.; Vaage, I.J. Osteoblast Differentiation at a Glance. *Med Sci Monit Basic Res* **2016**, *22*, 95–106.

13. Setiawati, R.; Rahardjo, P. *Bone Development and Growth*; IntechOpen, **2018**; ISBN 978-1-78985-768-9.

14. Dallas, S.L.; Bonewald, L.F. Dynamics of the Transition from Osteoblast to Osteocyte. *Ann N Y Acad Sci* **2010**, *1192*, 437–443.

15. Schaffler, M.B.; Cheung, W.-Y.; Majeska, R.; Kennedy, O. Osteocytes: Master Orchestrators of Bone. *Calcif Tissue Int* **2014**, *94*, 5–24.

16. Ru, J.; Wang, Y. Osteocyte Apoptosis: The Roles and Key Molecular Mechanisms in Resorption-Related Bone Diseases. *Cell Death Dis* **2020**, *11*, 1–24.

17. Suda, T.; Takahashi, N.; Udagawa, N.; Jimi, E.; Gillespie, M.T.; Martin, T.J. Modulation of Osteoclast Differentiation and Function by the New Members of the Tumor Necrosis Factor Receptor and Ligand Families. *Endocr Rev* **1999**, *20*, 345–357.

18. Boyle, W.J.; Simonet, W.S.; Lacey, D.L. Osteoclast Differentiation and Activation. *Nature* **2003**, *423*, 337–342.

19. Chen, B.; Wu, W.; Sun, W.; Zhang, Q.; Yan, F.; Xiao, Y. RANKL Expression in Periodontal Disease: Where Does RANKL Come From? *Biomed Res Int* **2014**.

20. Duka, M.; Eraković, M.; Dolićanin, Z.; Stefanović, D.; Čolić, M. Production of Soluble Receptor Activator of Nuclear Factor Kappa-B Ligand and Osteoprotegerin by Apical Periodontitis Cells in Culture and Their Modulation by Cytokines. *Mediat Inflamm* **2019**, e8325380.

21. Feng, X.; McDonald, J.M. Disorders of Bone Remodeling. *Annu Rev Pathol* **2011**, *6*, 121–145.

22. Miller, S.C.; de Saint-Georges, L.; Bowman, B.M.; Jee, W.S. Bone Lining Cells: Structure and Function. *Scanning Microsc* **1989**, *3*, 953–960; discussion 960-961.

23. Kenkre, J.; Bassett, J. The Bone Remodelling Cycle. *Ann Clin Biochem* **2018**, *55*, 308–327.

24. Feng, X. Chemical and Biochemical Basis of Cell-Bone Matrix Interaction in Health and Disease. *Curr Chem Biol* **2009**, *3*, 189–196,.

25. Lodish, H.; Berk, A.; Zipursky, S.L.; Matsudaira, P.; Baltimore, D.; Darnell, J. Collagen: The Fibrous Proteins of the Matrix. *Molecular Cell Biology. 4th edition* **2000**.

26. Bhowmick, M.; Fields, G.B. Stabilization of Collagen-Model, Triple-Helical Peptides for In Vitro and In Vivo Applications. *Methods Mol Biol* **2013**, *1081*, 167–194.

27. Sorushanova, A.; Delgado, L.M.; Wu, Z.; Shologu, N.; Kshirsagar, A.; Raghunath, R.; Mullen, A.M.; Bayon, Y.; Pandit, A.; Raghunath, M.; et al. The Collagen Suprafamily: From Biosynthesis to Advanced Biomaterial Development. *Adv Mater* **2019**, *31*, e1801651.

28. Lin, X.; Patil, S.; Gao, Y.-G.; Qian, A. The Bone Extracellular Matrix in Bone Formation and Regeneration. *Front Pharmacol* **2020**, *11*.

29. Morgan, S.; Poundarik, A.A.; Vashishth, D. Do Non-Collagenous Proteins Affect Skeletal Mechanical Properties? *Calcif Tissue Int* **2015**, *97*, 281–291, doi:10.1007/s00223-015-0016-3.

30. Mahamid, J.; Sharir, A.; Gur, D.; Zelzer, E.; Addadi, L.; Weiner, S. Bone Mineralization Proceeds through Intracellular Calcium Phosphate Loaded Vesicles: A Cryo-Electron Microscopy Study. *J Struct Biol* **2011**, *174*, 527–535.

31. Sorrentino, A.; Malucelli, E.; Rossi, F.; Cappadone, C.; Farruggia, G.; Moscheni, C.; Perez-Berna, A.J.; Conesa, J.J.; Colletti, C.; Roveri, N.; et al. Calcite as a Precursor of Hydroxyapatite in the Early Biomineralization of Differentiating Human Bone-Marrow Mesenchymal Stem Cells. *Int J Mol Sci* **2021**, *22*, 4939.

32. Supová, M. Isolation and Preparation of Nanoscale Bioapatites from Natural Sources: A Review. *J Nanosci Nanotechnol* **2014**, *14*, 546–563.

33. Palmer, L.C.; Newcomb, C.J.; Kaltz, S.R.; Spoerke, E.D.; Stupp, S.I. Biomimetic Systems for Hydroxyapatite Mineralization Inspired by Bone and Enamel. *Chem Rev* **2008**, *108*, 4754–4783.

34. Dey, P. *Bone Mineralisation*; IntechOpen, **2020**; ISBN 978-1-78985-040-6.

35. Procopio, A.; Malucelli, E.; Pacureanu, A.; Cappadone, C.; Farruggia, G.; Sargenti, A.; Castiglioni, S.; Altamura, D.; Sorrentino, A.; Giannini, C.; et al. Correction to Chemical Fingerprint of Zn–Hydroxyapatite in the Early Stages of Osteogenic Differentiation. *ACS Cent. Sci.* **2019**, *5*, 1731–1731.

36. Gaffney-Stomberg, E. The Impact of Trace Minerals on Bone Metabolism. *Biol Trace Elem Res* **2019**, *188*, 26–34.

37. Bigi, A.; Boanini, E. Functionalized Biomimetic Calcium Phosphates for Bone Tissue Repair. *J App Biomater Funct Mater* **2017**, *15*, e313–e325.

38. Radha, R.; Sreekanth, D. Insight of Magnesium Alloys and Composites for Orthopedic Implant Applications – a Review. *J Magnes Alloys* **2017**, *5*, 286–312.

39. Huang, W.; Yang, S.; Shao, J.; Li, Y.-P. Signaling and Transcriptional Regulation in Osteoblast Commitment and Differentiation. *Front Biosci* **2007**, *12*, 3068–3092.

40. Fetahu, I.S.; Höbaus, J.; Kállay, E. Vitamin D and the Epigenome. *Front Physiol* **2014**, *5*, 164.

41. Shahi, M.; Peymani, A.; Sahmani, M. Regulation of Bone Metabolism. *Rep Biochem Mol Biol* **2017**, *5*, 73–82.

42. Ichida, F.; Nishimura, R.; Hata, K.; Matsubara, T.; Ikeda, F.; Hisada, K.; Yatani, H.; Cao, X.; Komori, T.; Yamaguchi, A.; et al. Reciprocal Roles of Msx2 in Regulation of Osteoblast and Adipocyte Differentiation. *J Biol Chem* **2004**, *279*, 34015–34022.

43. Petrova, R.; Joyner, A.L. Roles for Hedgehog Signaling in Adult Organ Homeostasis and Repair. *Development* **2014**, *141*, 3445–3457.

44. Skoda, A.M.; Simovic, D.; Karin, V.; Kardum, V.; Vranic, S.; Serman, L. The Role of the Hedgehog Signaling Pathway in Cancer: A Comprehensive Review. *Bosn J Basic Med Sci* **2018**, *18*, 8–20.

45. AlMuraikhi, N.; Almasoud, N.; Binhamdan, S.; Younis, G.; Ali, D.; Manikandan, M.; Vishnubalaji, R.; Atteya, M.; Siyal, A.; Alfayez, M.; et al. Hedgehog Signaling Inhibition by

Smoothened Antagonist BMS-833923 Reduces Osteoblast Differentiation and Ectopic Bone Formation of Human Skeletal (Mesenchymal) Stem Cells. *Stem Cells Int* **2019**, *2019*.

46. MacDonald, B.T.; Tamai, K.; He, X. Wnt/β-Catenin Signaling: Components, Mechanisms, and Diseases. *Dev Cell* **2009**, *17*, 9–26.

47. Lee, S.; Remark, L.H.; Josephson, A.M.; Leclerc, K.; Lopez, E.M.; Kirby, D.J.; Mehta, D.; Litwa, H.P.; Wong, M.Z.; Shin, S.Y.; et al. Notch-Wnt Signal Crosstalk Regulates Proliferation and Differentiation of Osteoprogenitor Cells during Intramembranous Bone Healing. *NPJ Regen Med* **2021**, *6*, 29.

48. Lin, G.L.; Hankenson, K.D. Integration of BMP, Wnt, and Notch Signaling Pathways in Osteoblast Differentiation. *J Cell Biochem* **2011**, *112*, 3491–3501, doi:10.1002/jcb.23287.

49. Heo, J.S.; Lee, S.G.; Kim, H.O. Distal-Less Homeobox 5 Is a Master Regulator of the Osteogenesis of Human Mesenchymal Stem Cells. *Int J Mol Med* **2017**, *40*, 1486–1494.

50. Samee, N.; Geoffroy, V.; Marty, C.; Schiltz, C.; Vieux-Rochas, M.; Levi, G.; de Vernejoul, M.-C. Dlx5, a Positive Regulator of Osteoblastogenesis, Is Essential for Osteoblast-Osteoclast Coupling. *Am J Pathol* **2008**, *173*, 773–780.

51. Stein, G.S.; Lian, J.B.; Wijnen, A.J. van; Stein, J.L.; Montecino, M.; Javed, A.; Zaidi, S.K.; Young, D.W.; Choi, J.-Y.; Pockwinse, S.M. Runx2 Control of Organization, Assembly and Activity of the Regulatory Machinery for Skeletal Gene Expression. *Oncogene* **2004**, *23*, 4315–4329.

52. Nakashima, K.; Zhou, X.; Kunkel, G.; Zhang, Z.; Deng, J.M.; Behringer, R.R.; de Crombrugghe, B. The Novel Zinc Finger-Containing Transcription Factor Osterix Is Required for Osteoblast Differentiation and Bone Formation. *Cell* **2002**, *108*, 17–29.

53. Muff, R.; Ram Kumar, R.M.; Botter, S.M.; Born, W.; Fuchs, B. Genes Regulated in Metastatic Osteosarcoma: Evaluation by Microarray Analysis in Four Human and Two Mouse Cell Line Systems. *Sarcoma* **2012**, *2012*, e937506.

54. Ducy, P.; Zhang, R.; Geoffroy, V.; Ridall, A.L.; Karsenty, G. Osf2/Cbfa1: A Transcriptional Activator of Osteoblast Differentiation. *Cell* **1997**, *89*, 747–754.

55. Liu, Q.; Li, M.; Wang, S.; Xiao, Z.; Xiong, Y.; Wang, G. Recent Advances of Osterix Transcription Factor in Osteoblast Differentiation and Bone Formation. *Front. Cell Dev. Biol.* **2020**, *8*.

56. Felber, K.; Elks, P.M.; Lecca, M.; Roehl, H.H. Expression of Osterix Is Regulated by FGF and Wnt/β-Catenin Signalling during Osteoblast Differentiation. *PLoS One* **2015**, *10*.

57. Amarasekara, D.S.; Kim, S.; Rho, J. Regulation of Osteoblast Differentiation by Cytokine Networks. *Int J Mol Sci* **2021**, *22*, 2851.

58. Kaneto, C.M.; Lima, P.S.P.; Zanette, D.L.; Oliveira, T.Y.K.; de Assis Pereira, F.; Lorenzi, J.C.C.; dos Santos, J.L.; Prata, K.L.; Neto, J.M.P.; de Paula, F.J.A.; et al. Osteoblastic Differentiation of Bone Marrow Mesenchymal Stromal Cells in Bruck Syndrome. *BMC Med Genet* **2016**, *17*, 38.

59. Millán, J. The Role of Phosphatases in the Initiation of Skeletal Mineralization. *Calcif Tissue Int* **2012**, *93*.

60. Lowe, D.; Sanvictores, T.; John, S. Alkaline Phosphatase. In *StatPearls*; StatPearls Publishing: Treasure Island (FL), **2021.**

61. Udagawa, N.; Takahashi, N.; Yasuda, H.; Mizuno, A.; Itoh, K.; Ueno, Y.; Shinki, T.; Gillespie, M.T.; Martin, T.J.; Higashio, K.; et al. Osteoprotegerin Produced by Osteoblasts Is an Important Regulator in Osteoclast Development and Function. *Endocrinology* **2000**, *141*, 3478–3484.

62. Nakamura, M.; Udagawa, N.; Matsuura, S.; Mogi, M.; Nakamura, H.; Horiuchi, H.; Saito, N.; Hiraoka, B.Y.; Kobayashi, Y.; Takaoka, K.; et al. Osteoprotegerin Regulates Bone Formation through a Coupling Mechanism with Bone Resorption. *Endocrinology* **2003**, *144*, 5441–5449.

63. Jin, H.; van't Hof, R.J.; Albagha, O.M.E.; Ralston, S.H. Promoter and Intron 1 Polymorphisms of COL1A1 Interact to Regulate Transcription and Susceptibility to Osteoporosis. *Human Molecular Genetics* **2009**, *18*, 2729–2738.

64. Ortuño, M.J.; Susperregui, A.R.G.; Artigas, N.; Rosa, J.L.; Ventura, F. Osterix Induces Col1a1 Gene Expression through Binding to Sp1 Sites in the Bone Enhancer and Proximal Promoter Regions. *Bone* **2013**, *52*, 548–556.

65. Zoch, M.L.; Clemens, T.L.; Riddle, R.C. New Insights into the Biology of Osteocalcin. *Bone* **2016**, *82*, 42–49.

66. Ivaska, K.K.; Hentunen, T.A.; Vääräniemi, J.; Ylipahkala, H.; Pettersson, K.; Väänänen, H.K. Release of Intact and Fragmented Osteocalcin Molecules from Bone Matrix during Bone Resorption in Vitro. *J Biol Chem* **2004**, *279*, 18361–18369.

67. De Fusco, C.; Messina, A.; Monda, V.; Viggiano, E.; Moscatelli, F.; Valenzano, A.; Esposito, T.; Sergio, C.; Cibelli, G.; Monda, M.; et al. Osteopontin: Relation between Adipose Tissue and Bone Homeostasis. *Stem Cells International* **2017**, *2017*, e4045238, doi:10.1155/2017/4045238.

68. Icer, M.A.; Gezmen-Karadag, M. The Multiple Functions and Mechanisms of Osteopontin. *Clin Biochem* **2018**, *59*, 17–24.

69. Sharma, S.; Xing, F.; Liu, Y.; Wu, K.; Said, N.; Pochampally, R.; Shiozawa, Y.; Lin, H.-K.; Balaji, K.C.; Watabe, K. Secreted Protein Acidic and Rich in Cysteine (SPARC) Mediates Metastatic Dormancy of Prostate Cancer in Bone. *J Biol Chem* **2016**, *291*, 19351–19363.

70. Veis, A.; Dorvee, J.R. Biomineralization Mechanisms: A New Paradigm for Crystal Nucleation in Organic Matricies. *Calcif Tissue Int* **2013**, *93*, 307–315, doi:10.1007/s00223-012-9678-2.

71. Kolb, A.D.; Bussard, K.M. The Bone Extracellular Matrix as an Ideal Milieu for Cancer Cell Metastases. *Cancers (Basel)* **2019**, *11*.

72. Wu, J.; Hong, Y. Enhancing Cell Infiltration of Electrospun Fibrous Scaffolds in Tissue Regeneration. *Bioact Mater* **2016**, *1*, 56–64.

73. Chen, G.; Deng, C.; Li, Y.-P. TGF-β and BMP Signaling in Osteoblast Differentiation and Bone Formation. *Int J Biol Sci.* **2012**, *8*, 272–288.

74. Zou, M.-L.; Chen, Z.-H.; Teng, Y.-Y.; Liu, S.-Y.; Jia, Y.; Zhang, K.-W.; Sun, Z.-L.; Wu, J.-J.; Yuan, Z.-D.; Feng, Y.; et al. The Smad Dependent TGF-β and BMP Signaling Pathway in Bone Remodeling and Therapies. *Front Mol Biosci* **2021**, *8*.

75. Carvalho, C.R.; Oliveira, J.M.; Reis, R.L. Modern Trends for Peripheral Nerve Repair and Regeneration: Beyond the Hollow Nerve Guidance Conduit. *Front. Bioeng. Biotechnol.* **2019**, *7*.

76. Seibel, M.J. Biochemical Markers of Bone Turnover Part I: Biochemistry and Variability. *Clin Biochem Rev* **2005**, *26*, 97–122.

77. Krela-Kaźmierczak, I.; Szymczak, A.; Łykowska-Szuber, L.; Eder, P.; Stawczyk-Eder, K.; Klimczak, K.; Linke, K.; Horst-Sikorska, W. The Importance of Vitamin D in the Pathology of Bone Metabolism in Inflammatory Bowel Diseases. *Arch Med Sci* **2015**, *11*, 1028–1032.

78. Fleet, J.C. The Role of Vitamin D in the Endocrinology Controlling Calcium Homeostasis. *Mol Cell Endocrinol* **2017**, *453*, 36–45.

79. Blair, H.C.; Larrouture, Q.C.; Li, Y.; Lin, H.; Beer-Stoltz, D.; Liu, L.; Tuan, R.S.; Robinson, L.J.; Schlesinger, P.H.; Nelson, D.J. Osteoblast Differentiation and Bone Matrix Formation In Vivo and In Vitro. *Tissue Eng Part B Rev* **2017**, *23*, 268–280.

80. Dallas, S.L.; Prideaux, M.; Bonewald, L.F. The Osteocyte: An Endocrine Cell ... and More. *Endocr Rev* **2013**, *34*, 658–690, doi:10.1210/er.2012-1026.

81. Kohli, S.S.; Kohli, V.S. Role of RANKL–RANK/Osteoprotegerin Molecular Complex in Bone Remodeling and Its Immunopathologic Implications. *Indian J Endocrinol Metab* **2011**, *15*, 175–181.

82. Nakamura, H. Morphology, Function, and Differentiation of Bone Cells. *J Hard Tissue Biol* **2007**, *16*, 15–22.

83. Takito, J.; Inoue, S.; Nakamura, M. The Sealing Zone in Osteoclasts: A Self-Organized Structure on the Bone. *Int J Mol Sci* **2018**, *19*, 984.

84. Rucci, N. Molecular Biology of Bone Remodelling. *Clin Cases Miner Bone Metab* **2008**, *5*, 49–56.

85. Friedman, J.; Raisz, L.G. Thyrocalcitonin: Inhibitor of Bone Resorption in Tissue Culture. *Science* **1965**, *150*, 1465–1467.

86. Hadjidakis, D.J.; Androulakis, I.I. Bone Remodeling. *Ann N Y Acad Sci* **2006**, *1092*, 385–396.

87. Swanson, C.M.; Kohrt, W.M.; Buxton, O.M.; Everson, C.A.; Wright, K.P.; Orwoll, E.S.; Shea, S.A. The Importance of the Circadian System & Sleep for Bone Health. *Metabolism* **2018**, *84*, 28–43.

88. Beniash, E. Biominerals—Hierarchical Nanocomposites: The Example of Bone. *WIREs Nanomed Nanobiotechnol* **2011**, *3*, 47–69.

89. Omelon, S.; Ariganello, M.; Bonucci, E.; Grynpas, M.; Nanci, A. A Review of Phosphate Mineral Nucleation in Biology and Geobiology. *Calcif Tissue Int* **2013**, *93*, 382–396.

90. Margolis, H.C.; Kwak, S.-Y.; Yamazaki, H. Role of Mineralization Inhibitors in the Regulation of Hard Tissue Biomineralization: Relevance to Initial Enamel Formation and Maturation. *Front Physiol* **2014**, *5*, 339.

91. Zhou, X.; Cui, Y.; Zhou, X.; Han, J. Phosphate/Pyrophosphate and MV-Related Proteins in Mineralisation: Discoveries from Mouse Models. *Int J Biol Sci* **2012**, *8*, 778–790.

92. Stock, S.R. The Mineral–Collagen Interface in Bone. *Calcif Tissue Int* **2015**, *97*, 262–280.

93. Murshed, M. Mechanism of Bone Mineralization. *Cold Spring Harb Perspect Med* **2018**, *8*, a031229.

94. Boonrungsiman, S.; Gentleman, E.; Carzaniga, R.; Evans, N.D.; McComb, D.W.; Porter, A.E.; Stevens, M.M. The Role of Intracellular Calcium Phosphate in Osteoblast-Mediated Bone Apatite Formation. *PNAS* **2012**, *109*, 14170–14175.

95. Tang, C.; Wei, Y.; Gu, L.; Zhang, Q.; Li, M.; Yuan, G.; He, Y.; Huang, L.; Liu, Y.; Zhang, Y. Biomineral Precursor Formation Is Initiated by Transporting Calcium and Phosphorus Clusters from the Endoplasmic Reticulum to Mitochondria. *Adv Sci* **2020**, *7*, 1902536.

96. Lindsey, B.A.; Markel, J.E.; Kleinerman, E.S. Osteosarcoma Overview. *Rheumatol Ther* **2017**, *4*, 25–43.

97. Shaker, J.L. Paget's Disease of Bone: A Review of Epidemiology, Pathophysiology and Management. *Ther Adv Musculoskelet Dis* **2009**, *1*, 107–125.

98. Morrow, J.J.; Khanna, C. Osteosarcoma Genetics and Epigenetics: Emerging Biology and Candidate Therapies. *Crit Rev Oncog* **2015**, *20*, 173–197.

99. Czarnecka, A.M.; Synoradzki, K.; Firlej, W.; Bartnik, E.; Sobczuk, P.; Fiedorowicz, M.; Grieb, P.; Rutkowski, P. Molecular Biology of Osteosarcoma. *Cancers (Basel)* **2020**, *12*.

100. Haydon, R.C.; Luu, H.H.; He, T.-C. Osteosarcoma and Osteoblastic Differentiation: A New Perspective on Oncogenesis. *Clin. Orthop. Relat. Res.* **2007**, *454*, 237–246.

101. Rickel, K.; Fang, F.; Tao, J. Molecular Genetics of Osteosarcoma. *Bone* **2017**, *102*, 69–79.

102. Wagner, E.R.; Luther, G.; Zhu, G.; Luo, Q.; Shi, Q.; Kim, S.H.; Gao, J.-L.; Huang, E.; Gao, Y.; Yang, K.; et al. Defective Osteogenic Differentiation in the Development of Osteosarcoma. *Sarcoma* **2011**, *2011*, 325238.

103. Le Nail, L.-R.; Brennan, M.; Rosset, P.; Deschaseaux, F.; Piloquet, P.; Pichon, O.; Le Caignec, C.; Crenn, V.; Layrolle, P.; Hérault, O.; et al. Comparison of Tumor- and Bone Marrow-Derived Mesenchymal Stromal/Stem Cells from Patients with High-Grade Osteosarcoma. *Int J Mol Sci* **2018**, *19*.

104. Brown, H.K.; Schiavone, K.; Gouin, F.; Heymann, M.-F.; Heymann, D. Biology of Bone Sarcomas and New Therapeutic Developments. *Calcif Tissue Int* **2018**, *102*, 174–195.

105. Ando, K.; Heymann, M.-F.; Stresing, V.; Mori, K.; Rédini, F.; Heymann, D. Current Therapeutic Strategies and Novel Approaches in Osteosarcoma. *Cancers (Basel)* **2013**, *5*, 591–616.

106. Klein, M.; Siegal, G. Osteosarcoma Anatomic and Histologic Variants. *Am J Clin Pathol* **2006**, *125*, 555–581.

107. Mutsaers, A.J.; Walkley, C.R. Cells of Origin in Osteosarcoma: Mesenchymal Stem Cells or Osteoblast Committed Cells? *Bone* **2014**, *62*, 56–63.

108. Palmerini, E.; Setola, E.; Grignani, G.; D'Ambrosio, L.; Comandone, A.; Righi, A.; Longhi, A.; Cesari, M.; Paioli, A.; Hakim, R.; et al. High Dose Ifosfamide in Relapsed and Unresectable High-Grade Osteosarcoma Patients: A Retrospective Series. *Cells* **2020**, *9*, E2389.

109. Longhi, A.; Paioli, A.; Palmerini, E.; Cesari, M.; Abate, M.E.; Setola, E.; Spinnato, P.; Donati, D.; Hompland, I.; Boye, K. Pazopanib in Relapsed Osteosarcoma Patients: Report on 15 Cases. *Acta Oncol* **2019**, *58*, 124–128.

110. Avnet, S.; Di Pompo, G.; Chano, T.; Errani, C.; Ibrahim-Hashim, A.; Gillies, R.J.; Donati, D.M.; Baldini, N. Cancer-Associated Mesenchymal Stroma Fosters the Stemness of Osteosarcoma Cells in Response to Intratumoral Acidosis via NF-KB Activation. *Int J Cancer* **2017**, *140*, 1331–1345.

111. Zhao, X.; Wu, Q.; Gong, X.; Liu, J.; Ma, Y. Osteosarcoma: A Review of Current and Future Therapeutic Approaches. *Biomed Eng Online* **2021**, *20*.

112. Saraf, A.J.; Fenger, J.M.; Roberts, R.D. Osteosarcoma: Accelerating Progress Makes for a Hopeful Future. *Front Oncol* **2018**, *8*.

113. Gerrand, C.; Athanasou, N.; Brennan, B.; Grimer, R.; Judson, I.; Morland, B.; Peake, D.; Seddon, B.; Whelan, J.; On behalf of the British Sarcoma Group UK Guidelines for the Management of Bone Sarcomas. *Clinical Sarcoma Research* **2016**, *6*, 7.

114. Pucci, C.; Martinelli, C.; Ciofani, G. Innovative Approaches for Cancer Treatment: Current Perspectives and New Challenges. *Ecancermedicalscience* **2019**, *13*.

115. Righi, A.; Paioli, A.; Dei Tos, A.P.; Gambarotti, M.; Palmerini, E.; Cesari, M.; Marchesi, E.; Donati, D.M.; Picci, P.; Ferrari, S. High-Grade Focal Areas in Low-Grade Central Osteosarcoma: High-Grade or Still Low-Grade Osteosarcoma? *Clin Sarcoma Res* **2015**, *5*, 23.

116. Duchi, S.; Sotgiu, G.; Lucarelli, E.; Ballestri, M.; Dozza, B.; Santi, S.; Guerrini, A.; Dambruoso, P.; Giannini, S.; Donati, D.; et al. Mesenchymal Stem Cells as Delivery Vehicle of Porphyrin Loaded Nanoparticles: Effective Photoinduced in Vitro Killing of Osteosarcoma. *J Control Release* **2013**, *168*, 225–23.

117. Dozza, B.; Papi, A.; Lucarelli, E.; Scotlandi, K.; Pierini, M.; Tresca, G.; Donati, D.; Orlandi, M. Cell Growth Inhibition and Apoptotic Effect of the Rexinoid 6-OH-11-O-Hydroxyphenantrene on Human Osteosarcoma and Mesenchymal Stem Cells. *Toxicol In Vitro* **2012**, *26*, 142–149.

118. Strzelecka-Kiliszek, A.; Bozycki, L.; Mebarek, S.; Buchet, R.; Pikula, S. Characteristics of Minerals in Vesicles Produced by Human Osteoblasts HFOB 1.19 and Osteosarcoma Saos-2 Cells Stimulated for Mineralization. *J Inorg Biochem* **2017**, *171*, 100–107.

119. Ahmad, M.; McCarthy, M.; Gronowicz, G. An in Vitro Model for Mineralization of Human Osteoblast-like Cells on Implant Materials. *Biomaterials* **1999**, *20*, 211–220.

120. Yen, M.-L.; Chien, C.-C.; Chiu, I.-M.; Huang, H.-I.; Chen, Y.-C.; Hu, H.-I.; Yen, B.L. Multilineage Differentiation and Characterization of the Human Fetal Osteoblastic 1.19 Cell Line: A Possible in Vitro Model of Human Mesenchymal Progenitors. *Stem Cells* **2007**, *25*, 125–131.

121. Czekanska, E.M.; Stoddart, M.J.; Richards, R.G.; Hayes, J.S. In Search of an Osteoblast Cell Model for in Vitro Research. *Eur Cell Mater* **2012**, *24*, 1–17, doi:10.22203/ecm.v024a01.

122. Kaur, G.; Dufour, J.M. Cell Lines. *Spermatogenesis* **2012**, *2*, 1–5, doi:10.4161/spmg.19885.

123. Mendonsa, A.M.; Na, T.-Y.; Gumbiner, B.M. E-Cadherin in Contact Inhibition and Cancer. *Oncogene* **2018**, *37*, 4769–4780.

124. Guijarro, M.V. Osteosarcoma: Mouse Models, Cell of Origin and Cancer Stem Cell. *Postdoc J* **2014**, *2*, 19–30.

125. Quarles, L.D.; Yohay, D.A.; Lever, L.W.; Caton, R.; Wenstrup, R.J. Distinct Proliferative and Differentiated Stages of Murine MC3T3-E1 Cells in Culture: An in Vitro Model of Osteoblast Development. *J Bone Miner Res* **1992**, *7*, 683–692.

126. Kartsogiannis, V.; Ng, K.W. Cell Lines and Primary Cell Cultures in the Study of Bone Cell Biology. *Mol Cell Endocrinol* **2004**, *228*, 79–102.

127. Pontén, J.; Saksela, E. Two Established in Vitro Cell Lines from Human Mesenchymal Tumours. *Int J Cancer* **1967**, *2*, 434–447.

128. McAllister, R.M.; Gardner, M.B.; Greene, A.E.; Bradt, C.; Nichols, W.W.; Landing, B.H. Cultivation in Vitro of Cells Derived from a Human Osteosarcoma. *Cancer* **1971**, *27*, 397–402.

129. Clover, J.; Gowen, M. Are MG-63 and HOS TE85 Human Osteosarcoma Cell Lines Representative Models of the Osteoblastic Phenotype? *Bone* **1994**, *15*, 585–591.

130. Rhim, J.S.; Putman, D.L.; Arnstein, P.; Huebner, R.J.; McAllister, R.M. Characterization of Human Cells Transformed in Vitro by N-Methyl-N'-Nitro-N-Nitrosoguanidine. *Int J Cancer* **1977**, *19*, 505–510.

131. Luu, H.H.; Kang, Q.; Park, J.K.; Si, W.; Luo, Q.; Jiang, W.; Yin, H.; Montag, A.G.; Simon, M.A.; Peabody, T.D.; et al. An Orthotopic Model of Human Osteosarcoma Growth and Spontaneous Pulmonary Metastasis. *Clin Exp Metastasis* **2005**, *22*, 319–329.

132. Kirsten, W.H.; Mayer, L.A. Morphologic Responses to a Murine Erythroblastosis Virus. *J Natl Cancer Inst* **1967**, *39*, 311–335.

133. Ikeda, T.; Futaesaku, Y.; Tsuchida, N. In Vitro Differentiation of the Human Osteosarcoma Cell Lines, HOS and KHOS. *Virchows Archiv B Cell Pathol* **1992**, *62*, 199–206.

134. Campione-Piccardo, J.; Rawls, W.E.; Bacchetti, S. Selective Assay for Herpes Simplex Viruses Expressing Thymidine Kinase. *J Virol* **1979**, *31*, 281–287.

135. Boyle, D.B.; Coupar, B.E. Identification and Cloning of the Fowlpox Virus Thymidine Kinase Gene Using Vaccinia Virus. *J Gen Virol* **1986**, *67 (Pt 8)*, 1591–1600.

136. Rodan, S.B.; Imai, Y.; Thiede, M.A.; Wesolowski, G.; Thompson, D.; Bar-Shavit, Z.; Shull, S.; Mann, K.; Rodan, G.A. Characterization of a Human Osteosarcoma Cell Line (Saos-2) with Osteoblastic Properties. *Cancer Res.* **1987**, *47*, 4961–4966.

137. Heremans, H.; Billiau, A.; Cassiman, J.J.; Mulier, J.C.; de Somer, P. In Vitro Cultivation of Human Tumor Tissues. II. Morphological and Virological Characterization of Three Cell Lines. *Oncology* **1978**, *35*, 246–252.

138. Billiau, A.; Edy, V.G.; Heremans, H.; Van Damme, J.; Desmyter, J.; Georgiades, J.A.; De Somer, P. Human Interferon: Mass Production in a Newly Established Cell Line, MG-63. *Antimicrob Agents Chemother* **1977**, *12*, 11–15.

139. Pautke, C.; Schieker, M.; Tischer, T.; Kolk, A.; Neth, P.; Mutschler, W.; Milz, S. Characterization of Osteosarcoma Cell Lines MG-63, Saos-2 and U-2 OS in Comparison to Human Osteoblasts. *Anticancer Res* **2004**, *24*, 3743–3748.

140. Fedde, K.N. Human Osteosarcoma Cells Spontaneously Release Matrix-Vesicle-like Structures with the Capacity to Mineralize. *Bone Miner* **1992**, *17*, 145–151.

141. Rao, L.G.; Sutherland, M.K.; Reddy, G.S.; Siu-Caldera, M.L.; Uskokovic, M.R.; Murray, T.M. Effects of 1alpha,25-Dihydroxy-16ene, 23yne-Vitamin D3 on Osteoblastic Function in Human Osteosarcoma SaOS-2 Cells: Differentiation-Stage Dependence and Modulation by 17-Beta Estradiol. *Bone* **1996**, *19*, 621–627.

142. Saldaña, L.; Bensiamar, F.; Boré, A.; Vilaboa, N. In Search of Representative Models of Human Bone-Forming Cells for Cytocompatibility Studies. *Acta Biomater* **2011**, *7*, 4210–4221.

143. Müller, W.E.G.; Wang, X.; Diehl-Seifert, B.; Kropf, K.; Schlossmacher, U.; Lieberwirth, I.; Glasser, G.; Wiens, M.; Schröder, H.C. Inorganic Polymeric Phosphate/Polyphosphate as an Inducer of Alkaline Phosphatase and a Modulator of Intracellular Ca2+ Level in Osteoblasts (SaOS-2 Cells) in Vitro. *Acta Biomater* **2011**, *7*, 2661–2671.

144. Fernandes, R.J.; Harkey, M.A.; Weis, M.; Askew, J.W.; Eyre, D.R. The Post-Translational Phenotype of Collagen Synthesized by Saos-2 Osteosarcoma Cells. *Bone* **2007**, *40*, 1343–1351.

145. Bilbe, G.; Roberts, E.; Birch, M.; Evans, D.B. PCR Phenotyping of Cytokines, Growth Factors and Their Receptors and Bone Matrix Proteins in Human Osteoblast-like Cell Lines. *Bone* **1996**, *19*, 437–445.

146. Prideaux, M.; Wijenayaka, A.R.; Kumarasinghe, D.D.; Ormsby, R.T.; Evdokiou, A.; Findlay, D.M.; Atkins, G.J. SaOS2 Osteosarcoma Cells as an in Vitro Model for Studying the Transition of Human Osteoblasts to Osteocytes. *Calcif. Tissue Int.* **2014**, *95*, 183–193.

147. Joseph, J.S.; Malindisa, S.T.; Ntwasa, M. Two-Dimensional (2D) and Three-Dimensional (3D) Cell Culturing in Drug Discovery; IntechOpen, 2018; ISBN 978-1-78984-867-0.

148. Antoni, D.; Burckel, H.; Josset, E.; Noel, G. Three-Dimensional Cell Culture: A Breakthrough in Vivo. *Int J Mol Sci* **2015**, *16*, 5517–5527.

149. Jensen, C.; Teng, Y. Is It Time to Start Transitioning From 2D to 3D Cell Culture? *Front. Mol. Biosci.* **2020**, *7*.

150. Klimek, K.; Ginalska, G. Proteins and Peptides as Important Modifiers of the Polymer Scaffolds for Tissue Engineering Applications—A Review. *Polymers* **2020**, *12*, 844.

151. Saydé, T.; El Hamoui, O.; Alies, B.; Gaudin, K.; Lespes, G.; Battu, S. Biomaterials for Three-Dimensional Cell Culture: From Applications in Oncology to Nanotechnology. *Nanomaterials* **2021**, *11*, 481.

152. O'Brien, F.J. Biomaterials & Scaffolds for Tissue Engineering. *Materials Today* **2011**, *14*, 88–95.

153. Marcos, J.J.L.; Perrotti, V.; Iaculli, F.; Aragones, Á.; Benfatti, C.A.M.; Magrin, G.L.; Piattelli, A.; Bianchini, M.A. Physical and Mechanical Properties of Composite Scaffolds with or without Collagen Impregnation. *Applied Sciences* **2019**, *9*, 4296.

154. Du, X.; Fu, S.; Zhu, Y. 3D Printing of Ceramic-Based Scaffolds for Bone Tissue Engineering: An Overview. *J. Mater. Chem. B* **2018**, *6*, 4397–4412.

155. Graham, L.; Orenstein, J.M. Processing Tissue and Cells for Transmission Electron Microscopy in Diagnostic Pathology and Research. *Nature Protocols* **2007**, *2*, 2439–2450.

156. Alberts, B.; Johnson, A.; Lewis, J.; Raff, M.; Roberts, K.; Walter, P. Looking at the Structure of Cells in the Microscope. *Mol Biol Cell. 4th edition* **2002**.

157. Hulbert, S.L.; Williams, G.P. 1. Synchrotron Radiation Sources. Vacuum Ultraviolet Spectroscopy I. Series: Experimental Methods in the Physical Sciences **1998**, *31*, 1–25.

158. Malucelli, E.; Procopio, A.; Fratini, M.; Gianoncelli, A.; Notargiacomo, A.; Merolle, L.; Sargenti, A.; Castiglioni, S.; Cappadone, C.; Farruggia, G.; et al. Single Cell versus Large Population Analysis: Cell Variability in Elemental Intracellular Concentration and Distribution. *Anal Bioanal Chem* **2018**, *410*, 337–348.

159. Gramaccioni, C.; Yang, Y.; Procopio, A.; Pacureanu, A.; Bohic, S.; Malucelli, E.; Iotti, S.; Farruggia, G.; Bukreeva, I.; Notargiacomo, A.; et al. Nanoscale Quantification of Intracellular Element Concentration by X-Ray Fluorescence Microscopy Combined with X-Ray Phase Contrast Nanotomography. *Appl. Phys. Lett.* **2018**, *112*, 053701.

160. Acquafredda, P. XRF Technique. *Physical Sciences Reviews* **2019**, *4*.

161. Thompson, A.C.; Attwood, D.T.; Howells, M.R.; Kortright, J.B.; Robinson, A.L.; Underwood, J.H.; Kim, K.-J.; Kirz, J.; Lindau, I.; Pianetta, P.; et al. X-Ray Data Booklet. 457.

162. Bohic, S.; Simionovici, A.; Snigirev, A.; Ortega, R.; Devès, G.; Heymann, D.; Schroer, C.G. Synchrotron Hard X-Ray Microprobe: Fluorescence Imaging of Single Cells. *Appl. Phys. Lett.* **2001**, *78*, 3544–3546.

163. Hu, Q.; Antipova, O.A.; O'Halloran, T.V.; Wolfner, M.F. X-Ray Fluorescence Microscopy Scanning of Drosophila Oocytes and Eggs. *STAR Protoc* **2021**, *2*, 100247.

164. Ortega, R.; Carmona, A.; Llorens, I.; Solari, P.L. X-Ray Absorption Spectroscopy of Biological Samples. A Tutorial. *J. Anal. At. Spectrom.* **2012**, *27*, 2054, doi:10.1039/c2ja30224a.

165. Yano, J.; Yachandra, V.K. X-Ray Absorption Spectroscopy. *Photosynth Res* **2009**, *102*, 241–254.

166. Porcaro, F.; Roudeau, S.; Carmona, A.; Ortega, R. Advances in Element Speciation Analysis of Biomedical Samples Using Synchrotron-Based Techniques. *Trends Anal Chem* **2018**, *104*, 22–41.

167. Henderson, G.S.; de Groot, F.M.F.; Moulton, B.J.A. X-Ray Absorption Near-Edge Structure (XANES) Spectroscopy. *Reviews in Mineralogy and Geochemistry* **2014**, *78*, 75–138.

168. Schneider, G.; Guttmann, P.; Heim, S.; Rehbein, S.; Mueller, F.; Nagashima, K.; Heymann, J.B.; Müller, W.G.; McNally, J.G. Three-Dimensional Cellular Ultrastructure Resolved by X-Ray Microscopy. *Nat Methods* **2010**, *7*, 985–987.

169. Leontowich, A.F.G.; Berg, R.; Regier, C.N.; Taylor, D.M.; Wang, J.; Beauregard, D.; Geilhufe, J.; Swirsky, J.; Wu, J.; Karunakaran, C.; et al. Cryo Scanning Transmission X-Ray Microscope Optimized for Spectrotomography. *Review of Scientific Instruments* **2018**, *89*, 093704.

170. McDermott, G.; Le Gros, M.A.; Knoechel, C.G.; Uchida, M.; Larabell, C.A. Soft X-Ray Tomography and Cryogenic Light Microscopy: The Cool Combination in Cellular Imaging. *Trends Cell Biol* **2009**, *19*, 587–595.

171. Otón, J.; Pereiro, E.; Pérez-Berná, A.J.; Millach, L.; Sorzano, C.O.S.; Marabini, R.; Carazo, J.M. Characterization of Transfer Function, Resolution and Depth of Field of a Soft X-Ray Microscope Applied to Tomography Enhancement by Wiener Deconvolution. *Biomed Opt Express* **2016**, *7*, 5092–5103.

172. Sorrentino, A.; Nicolás, J.; Valcárcel, R.; Chichón, F.J.; Rosanes, M.; Avila, J.; Tkachuk, A.; Irwin, J.; Ferrer, S.; Pereiro, E. MISTRAL: A Transmission Soft X-Ray Microscopy Beamline for Cryo Nano-Tomography of Biological Samples and Magnetic Domains Imaging. *J Synchrotron Rad* **2015**, *22*, 1112–1117.

173. Kördel, M.; Kördel, M.; Dehlinger, A.; Dehlinger, A.; Dehlinger, A.; Seim, C.; Seim, C.; Vogt, U.; Fogelqvist, E.; Fogelqvist, E.; et al. Laboratory Water-Window x-Ray Microscopy. *Optica*, **2020**, *7*, 658–674.

174. Rawson, S.D.; Maksimcuka, J.; Withers, P.J.; Cartmell, S.H. X-Ray Computed Tomography in Life Sciences. *BMC Biology* **2020**, *18*, 21.

175. Bonse, U.; Busch, F. X-Ray Computed Microtomography (MCT) Using Synchrotron Radiation (SR). *Progress in Biophysics and Molecular Biology* **1996**, *65*, 133–169.

176. Barrett, H.H. III The Radon Transform and Its Applications. In *Progress in Optics*; Wolf, E., Ed.; Elsevier, 1984; Vol. 21, pp. 217–286.

177. Cooper, D.M.L.; Turinsky, A.L.; Sensen, C.W.; Hallgrímsson, B. Quantitative 3D Analysis of the Canal Network in Cortical Bone by Micro-Computed Tomography. *Anat Rec B New Anat* **2003**, *274*, 169–179.

178. Palacio-Mancheno, P.; Larriera, A.; Doty, S.; Cardoso, L.; Fritton, S. 3D Assessment of Cortical Bone Porosity and Tissue Mineral Density Using High-Resolution MCT: Effects of Resolution and Threshold Method. *J Bone Miner Res* **2014**, *29*.

179. Cappadone, C.; Stefanelli, C.; Malucelli, E.; Zini, M.; Onofrillo, C.; Locatelli, A.; Rambaldi, M.; Sargenti, A.; Merolle, L.; Farruggia, G.; et al. P53-Dependent and P53-Independent Anticancer Activity of a New Indole Derivative in Human Osteosarcoma Cells. *Biochem Biophys Res Commun* **2015**, *467*, 348–353.

180. Pasini, A.; Lovecchio, J.; Ferretti, G.; Giordano, E. Medium Perfusion Flow Improves Osteogenic Commitment of Human Stromal Cells Available, *Stem Cell Int*, **2019**, ID 1304194

181. Penner-Hahn, J.E. 2.13 X-Ray Absorption Spectroscopy. 28.

182. MessaoudiI, C.; Boudier, T.; Sorzano, C.O.S.; Marco, S. TomoJ: Tomography Software for Three-Dimensional Reconstruction in Transmission Electron Microscopy. *BMC Bioinformatics* **2007**, *8*, 288.

183. Sargenti, A.; Farruggia, G.; Zaccheroni, N.; Marraccini, C.; Sgarzi, M.; Cappadone, C.; Malucelli, E.; Procopio, A.; Prodi, L.; Lombardo, M.; et al. Synthesis of a Highly Mg2+-Selective Fluorescent Probe and Its Application to Quantifying and Imaging Total Intracellular Magnesium. *Nat Protoc* **2017**, *12*, 461–471.

184. Casagrande, S.; Tiribuzi, R.; Cassetti, E.; Selmin, F.; Gervasi, G.L.; Barberini, L.; Freddolini, M.; Ricci, M.; Schoubben, A.; Cerulli, G.G.; et al. Biodegradable Composite Porous Poly(DL -Lactide- *Co* -Glycolide) Scaffold Supports Mesenchymal Stem Cell Differentiation and Calcium Phosphate Deposition. *Artif Cells Nanomed Biotechnol* **2018**, *46*, 219–229.

185. Lovecchio, J.; Gargiulo, P.; Vargas Luna, J.L.; Giordano, E.; Sigurjónsson, Ó.E. A Standalone Bioreactor System to Deliver Compressive Load under Perfusion Flow to HBMSC-Seeded 3D Chitosan-Graphene Templates. *Sci Rep* **2019**, *9*, 1–11

186. Gianoncelli, A.; Kaulich, B.; Alberti, R.; Klatka, T.; Longoni, A.; de Marco, A.; Marcello, A.; Kiskinova, M. Simultaneous Soft X-Ray Transmission and Emission Microscopy. *Nucl Instrum Methods* **2009**, *608*, 195–198.

187. Gianoncelli, A.; Morrison, G.R.; Kaulich, B.; Bacescu, D.; Kovac, J. Scanning Transmission X-Ray Microscopy with a Configurable Detector. *Appl Phys Lett* **2006**, *89*, 251117.

188. Solé, V.; Papillon, E.; Cotte, M.; Walter, P.; Susini, J. A Multiplatform Code for the Analysis of Energy-Dispersive X-Ray Fluorescence Spectra. *Spectrochim Acta Part B At Spectrosc* **2007**, *62*, 63–68.

189. Polacci, M.; Baker, D.; Mancini, L.; Tromba, G.; Zanini, F. Three-Dimensional Investigation of Volcanic Textures by X-Ray Microtomography and Implications for Conduit Processes. *Geophys Res Lett* **2006**, *33*.

190. Zandomeneghi, D.; Voltolini, M.; Mancini, L.; Brun, F.; Dreossi, D.; Polacci, M. Quantitative Analysis of X-Ray Microtomography Images of Geomaterials: Application to Volcanic Rocks. *Geosphere* **2010**, *6*, 793–804.

191. Tromba, G.; Longo, R.; Abrami, A.; Arfelli, F.; Astolfo, A.; Bregant, P.; Brun, F.; Casarin, K.; Chenda, V.; Dreossi, D.; et al. The SYRMEP Beamline of Elettra: Clinical Mammography and Bio-medical Applications. *AIP Conference Proceedings* **2010**, *1266*, 18–23.

192. Brun, F.; Pacilè, S.; Accardo, A.; Kourousias, G.; Dreossi, D.; Mancini, L.; Tromba, G.; Pugliese, R. Enhanced and Flexible Software Tools for X-Ray Computed Tomography at the Italian Synchrotron Radiation Facility Elettra. *Fundam Inform* **2015**, *141*, 233–243.

193. Paganin, D.; Mayo, S.C.; Gureyev, T.E.; Miller, P.R.; Wilkins, S.W. Simultaneous Phase and Amplitude Extraction from a Single Defocused Image of a Homogeneous Object. *J Microsc* **2002**, *206*, 33–40.

194. Donati, I.; Stredanska, S.; Silvestrini, G.; Vetere, A.; Marcon, P.; Marsich, E.; Mozetic, P.; Gamini, A.; Paoletti, S.; Vittur, F. The Aggregation of Pig Articular Chondrocyte and Synthesis of Extracellular Matrix by a Lactose-Modified Chitosan. *Biomaterials* **2005**, *26*, 987–998.

195. Murray, E.; Provvedini, D.; Curran, D.; Catherwood, B.; Sussman, H.; Manolagas, S. Characterization of a Human Osteoblastic Osteosarcoma Cell Line (SAOS-2) with High Bone Alkaline Phosphatase Activity. *J Bone Miner Res* **1987**, *2*, 231–238.

196. Postiglione, L.; Di Domenico, G.; Ramaglia, L.; Montagnani, S.; Salzano, S.; Di Meglio, F.; Sbordone, L.; Vitale, M.; Rossi, G. Behavior of SaOS-2 Cells Cultured on Different Titanium Surfaces. *J Dent Res* **2003**, *82*, 692–696.

197. Iwayama, T.; Okada, T.; Ueda, T.; Tomita, K.; Matsumoto, S.; Takedachi, M.; Wakisaka, S.; Noda, T.; Ogura, T.; Okano, T.; et al. Osteoblastic Lysosome Plays a Central Role in Mineralization. *Sci Adv* **2019**, *5*, eaax0672.

198. Shapiro, I.M.; Greenspan, J.S. Are Mitochondria Directly Involved in Biological Mineralisation? *Calcif Tissue Res* **1969**, *3*, 100–102.

199. Hasegawa, T.; Yamamoto, T.; Tsuchiya, E.; Hongo, H.; Tsuboi, K.; Kudo, A.; Abe, M.; Yoshida, T.; Nagai, T.; Khadiza, N.; et al. Ultrastructural and Biochemical Aspects of Matrix Vesicle-Mediated Mineralization. *Jpn Dent Sci Rev* **2017**, *53*, 34–45.

200. Beniash, E.; Metzler, R.A.; Lam, R.S.K.; Gilbert, P.U.P.A. TRANSIENT AMORPHOUS CALCIUM PHOSPHATE IN FORMING ENAMEL. *J Struct Biol* **2009**, *166*, 133–143.

201. Fleet, M.; Liu, X. Calcium L-2,L-3-Edge XANES of Carbonates, Carbonate Apatite, and Oldhamite (CaS). *American Mineralogist* **2009**, *94*, 1235–1241.

202. Cosmidis, J.; Benzerara, K.; Nassif, N.; Tyliszczak, T.; Bourdelle, F. Characterization of Ca-Phosphate Biological Materials by Scanning Transmission X-Ray Microscopy (STXM) at the Ca L2,3-, P L2,3- and C K-Edges. *Acta Biomater* **2015**, *12*, 260–269.

203. Marchegiani, F.; Cibej, E.; Vergni, P.; Tosi, G.; Fermani, S.; Falini, G. Hydroxyapatite Synthesis from Biogenic Calcite Single Crystals into Phosphate Solutions at Ambient Conditions. *II-VI Compd 1987, Proc of the Third Int Conf on II-VI Compd* **2009**, *311*, 4219–4225.

204. Huesa, C.; Houston, D.; Kiffer-Moreira, T.; Yadav, M.C.; Luis Millan, J.; Farquharson, C. The Functional Co-Operativity of Tissue-Nonspecific Alkaline Phosphatase (TNAP) and PHOSPHO1 during Initiation of Skeletal Mineralization. *Biochem BiophysRep* **2015**, *4*, 196–201.

205. Shapiro, I.M.; Landis, W.J.; Risbud, M.V. MATRIX VESICLES: ARE THEY ANCHORED EXOSOMES? *Bone* **2015**, *79*, 29–36.

206. Ansari, S.; de Wildt, B.W.M.; Vis, M.A.M.; de Korte, C.E.; Ito, K.; Hofmann, S.; Yuana, Y. Matrix Vesicles: Role in Bone Mineralization and Potential Use as Therapeutics. *Pharmaceuticals* **2021**, *14*, 289.

207. Forni, M.F.; Peloggia, J.; Trudeau, K.; Shirihai, O.; Kowaltowski, A.J. Murine Mesenchymal Stem Cell Commitment to Differentiation Is Regulated by Mitochondrial Dynamics. *Stem Cells* **2016**, *34*, 743–755.

208. Lehninger, A.L. Mitochondria and Calcium Ion Transport. *Biochem J* **1970**, *119*, 129–138.

209. Picone, G.; Cappadone, C.; Pasini, A.; Lovecchio, J.; Cortesi, M.; Farruggia, G.; Lombardo, M.; Gianoncelli, A.; Mancini, L.; Ralf H., M.; et al. Analysis of Intracellular Magnesium and Mineral

Depositions during Osteogenic Commitment of 3D Cultured Saos2 Cells. *Int J Mol Sci* **2020**, *21*, 2368.

210. Lucero, C.M.J.; Vega, O.A.; Osorio, M.M.; Tapia, J.C.; Antonelli, M.; Stein, G.S.; van Wijnen, A.J.; Galindo, M.A. The Cancer-Related Transcription Factor Runx2 Modulates Cell Proliferation in Human Osteosarcoma Cell Lines. *J. Cell. Physiol.* **2013**, *228*, 714–723.

211. Kong, Y.; Hu, X.; Zhong, Y.; Xu, K.; Wu, B.; Zheng, J. Magnesium-Enriched Microenvironment Promotes Odontogenic Differentiation in Human Dental Pulp Stem Cells by Activating ERK/BMP2/Smads Signaling. *Stem Cell Res Ther* **2019**, *10*.

212. Wang, Y.; Geng, Z.; Huang, Y.; Jia, Z.; Cui, Z.; Li, Z.; Wu, S.; Liang, Y.; Zhu, S.; Yang, X.; et al. Unraveling the Osteogenesis of Magnesium by the Activity of Osteoblasts in Vitro. *J. Mater. Chem. B* **2018**, *6*, 6615–6621.

213. Gianoncelli, A.; Kourousias, G.; Merolle, L.; Altissimo, M.; Bianco, A. Current Status of the TwinMic Beamline at Elettra: A Soft X-Ray Transmission and Emission Microscopy Station. *J Synchrotron Radiat* **2016**, *23*, 1526–1537, doi:10.1107/S1600577516014405.

214. Akram, M.A.; Ahmed, R.; Shakir, I.; Ibrahim, W.A.W.; Hussain, R. Extracting Hydroxyapatite and Its Precursors from Natural Resources. *J Mat Sci* **2013**, *49*, 1461–1475.

215. Milovac, D.; Gamboa-Martínez, T.C.; Ivankovic, M.; Gallego Ferrer, G.; Ivankovic, H. PCL-Coated Hydroxyapatite Scaffold Derived from Cuttlefish Bone: In Vitro Cell Culture Studies. *Mater Sci Eng C Mater Biol Appl* **2014**, *42*, 264–272.

216. Doube, M.; Kłosowski, M.M.; Arganda-Carreras, I.; Cordelières, F.P.; Dougherty, R.P.; Jackson, J.S.; Schmid, B.; Hutchinson, J.R.; Shefelbine, S.J. BoneJ: Free and Extensible Bone Image Analysis in ImageJ. *Bone* **2010**, *47*, 1076–1079.

217. Nudelman, F.; Pieterse, K.; George, A.; Bomans, P.H.H.; Friedrich, H.; Brylka, L.J.; Hilbers, P.A.J.; de With, G.; Sommerdijk, N.A.J.M. The Role of Collagen in Bone Apatite Formation in the Presence of Hydroxyapatite Nucleation Inhibitors. *Nat Mater* **2010**, *9*, 1004–1009.

218. Scaglione, S.; Giannoni, P.; Bianchini, P.; Sandri, M.; Marotta, R.; Firpo, G.; Valbusa, U.; Tampieri, A.; Diaspro, A.; Bianco, P.; et al. Order versus Disorder: In Vivo Bone Formation within Osteoconductive Scaffolds. *Sci Rep* **2012**, *2*, 1–6.

219. Giannini, C.; Siliqi, D.; Bunk, O.; Beraudi, A.; Ladisa, M.; Altamura, D.; Stea, S.; Baruffaldi, F. Correlative Light and Scanning X-Ray Scattering Microscopy of Healthy and Pathologic Human Bone Sections. *Sci Rep* **2012**, *2*, 1–5.

220. Chaudhuri, O.; Gu, L.; Klumpers, D.; Darnell, M.; Bencherif, S.A.; Weaver, J.C.; Huebsch, N.; Lee, H.; Lippens, E.; Duda, G.N.; et al. Hydrogels with Tunable Stress Relaxation Regulate Stem Cell Fate and Activity. *Nature Mater* **2016**, *15*, 326–334.

221. Bergemann, C.; Elter, P.; Lange, R.; Weißmann, V.; Hansmann, H.; Klinkenberg, E.-D.; Nebe, B. Cellular Nutrition in Complex Three-Dimensional Scaffolds: A Comparison between Experiments and Computer Simulations. *Int J Biomater* **2015**, *2015*, 584362.

222. Furlani, F.; Sacco, P.; Cok, M.; de Marzo, G.; Marsich, E.; Paoletti, S.; Donati, I. Biomimetic, Multiresponsive, and Self-Healing Lactose-Modified Chitosan (CTL)-Based Gels Formed via Competitor-Assisted Mechanism. *ACS Biomater. Sci. Eng.* **2019**, *5*, 5539–5547.